



**Politecnico
di Torino**

POLITECNICO DI TORINO

DEPARTMENT OF MECHANICAL ENGINEERING

Master thesis

**Handling system design as part of the NUMEN experiment
at the Istituto Nazionale di Fisica Nucleare**

Supervisors:

**Prof. Carlo Ferraresi
Ing. Carlo De Benedictis
Dr. Daniela Calvo, Ph.D.
Ing. Diego Sartirana**

Candidate:

Stefano Belliardo

April 2022

| | |
|--|-----------|
| Introduction..... | 1 |
| 1 The NUMEN project..... | 3 |
| 1.1 DCE process..... | 4 |
| 1.2 Upgrade of the NUMEN experiment..... | 6 |
| 1.3 Upgrade of the scattering chamber | 7 |
| 1.4 Gamma detectors | 10 |
| 2 Positioning of the gamma detectors..... | 12 |
| 2.1 Tasks of the support structure | 12 |
| 2.2 Subdivision of the domain..... | 13 |
| 2.3 Subdomains' trajectories | 15 |
| 2.3.1 Upstream inferior quarter | 15 |
| 2.3.2 Upper hemisphere..... | 19 |
| 2.3.3 Downstream right octant | 21 |
| 2.3.4 Downstream left octant | 22 |
| 3 Upstream inferior quarter's preliminary structure | 26 |
| 3.1 Requirements' analysis..... | 26 |
| 3.2 Construction configurations..... | 28 |
| 3.2.1 Central actuator with three cylindrical guides | 28 |
| 3.2.2 Lateral actuator with two cylindrical guides | 30 |
| 3.2.3 Three pneumatic actuators..... | 31 |
| 3.3 Development of the second configuration | 32 |
| 3.4 Sizing of the components | 34 |
| 3.4.1 Grooved guides' diameter | 34 |

| | | |
|----------|---|-----------|
| 3.4.2 | Actuator diameter | 37 |
| 3.4.3 | Sustain plates | 39 |
| 3.5 | Cart..... | 39 |
| 3.6 | Global consideration on preliminary solution..... | 45 |
| 4 | Frontal inferior quarter's intermediate solution | 46 |
| 4.1 | Structure design | 47 |
| 4.2 | Global consideration on solution 2..... | 49 |
| 5 | Frontal inferior quarter's final structure..... | 50 |
| 5.1 | The Stewart's platform | 50 |
| 5.1.1 | Geometry and inverse kinematic | 52 |
| 5.1.2 | Global geometry | 60 |
| 5.1.3 | Commercial Stewart platform | 65 |
| 5.1.4 | Manual Stewart platform design | 66 |
| 5.2 | Design and sizing of the elements of the supporting structure | 66 |
| 5.2.1 | Upstream inferior quarter shell..... | 67 |
| 5.2.2 | Shell's connecting bolts | 72 |
| 5.2.3 | Automation structure's connecting plate | 96 |
| 5.2.4 | Cylindrical guides' connecting bolts | 91 |
| 5.2.5 | Cylindrical guides | 92 |
| 5.2.6 | End stops plate's bolts | 100 |
| 5.2.7 | End stops' plate | 102 |
| 5.2.8 | Cylindrical bearings..... | 104 |

| | | |
|------------------------|--|------------|
| 5.2.9 | Cylindrical bearings' supporting plates..... | 116 |
| 5.2.10 | Supporting plates' connecting bolts | 123 |
| 5.2.11 | Vertical uprights..... | 126 |
| 5.2.12 | Vertical uprights' connecting bolts..... | 130 |
| 5.2.13 | Stewart platform..... | 134 |
| 5.2.14 | Linear bearings | 144 |
| 5.2.15 | Support frame | 151 |
| 5.2.16 | Patch panels | 154 |
| 5.3 | Control system..... | 155 |
| 5.4 | Price quote..... | 159 |
| 6 | Conclusions | 161 |
| 7 | Bibliography..... | 166 |
| 8 | Sitography..... | 167 |
| 9 | Catalogs | 168 |
| Appendix A..... | | 168 |
| | MATLAB Script for the solution of the Stewart platform inverse kinematic.. | 168 |

Introduction

The work developed in this thesis is my study concerning semi-automated handling of detectors inside the NUMEN experiment. NUMEN is a project approved by the Italian institute “Istituto Nazionale di Fisica Nucleare” (INFN) and it is based on the upgrade of the pre-existing MAGNEX spectrometer at the Laboratori Nazionali del Sud in Catania.

NUMEN has international relevance as complementary study to the knowledge of the nature of neutrinos. In particular, NUMEN will measure the cross sections of double charge exchange reactions of heavy ions. Until now all the tests have been performed using a low intensity line, but to collect more statistics, a new cyclotron that will produce more intense ion beams with a wider energy range per nucleon is being installed.

An upgrade of the MAGNEX spectrometer becomes then necessary. Many components will be replaced with new versions able to tolerate higher radiation levels and most of the manual steps required to change the experimental set-up during the tests will be automated. Indeed, the higher radiations produced by the nuclear reactions can activate the instrumentation located in the proximity of the scattering chamber forbidding technicians to directly modify the experimental set-up. Moreover, the automatic/semiautomatic movement of some parts of the experiment will simplify the maintenance procedure, allowing to operate on the instrumentation away from the numerous components present around the scattering chamber.

This thesis will focus on this last point, with the aim of studying and designing a high precision self-moving structure to place groups of gamma detectors in the right experiment's spot.

In the following chapters will be address issues related to the analysis of the MAGNEX structure, to the upgrades needed to carry out experiments with the new high-intensity line and to the possible constructive solutions for the Gamma detectors' supporting structures.

All these arguments will be thoroughly described in this thesis in chronological order so that it is simpler to follow the engineering process that had led to the last design solution.

1 The NUMEN project

The aim of the NUMEN (NUclear Matrix Elements for Neutrinoless double beta decay) experiment is to collect information for the determination of nuclear matrix elements of the neutrinoless Double Beta Decay process ($0\nu\beta\beta$), which is potentially the best way to prove the Majorana nature of neutrino and to extract its effective mass (figure 1.1). Evidence of the existence of such a nuclear reaction would show that a neutrino particle must coincide with its anti-particle, condition which would be in contrast with the current Standard Model and might open the way toward a Grand Unified Theory of fundamental interactions.^{1,2}

Since the $0\nu\beta\beta$ is an extremely rare phenomenon to be observed and it is strongly affected by others natural processes, information can be collected using others nuclear reactions as the Double Charge Exchange (DCE) process.

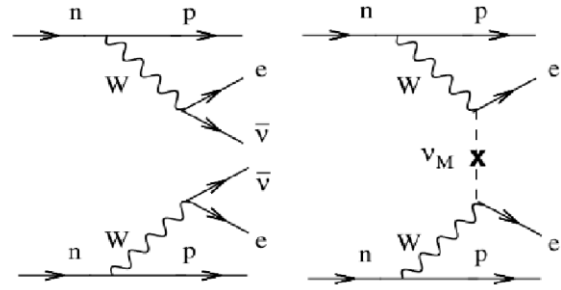


Figure 1.1: Feynman Diagrams for Double Beta Decay (left) and neutrinoless Double Beta Decay (right) processes.

It is right on this latter principle that NUMEN bases its operation. Indeed, a Double Charge Exchange process takes place during the experiments and, because of the similarity between the two previously described processes, useful information on the Double Beta Decay process can be obtained (i.e., the DCE cross sections).

¹ D. Sartirana, *Sistemi automatici per la movimentazione di bersagli per esperimenti di fisica nucleare*, Torino: Politecnico di Torino, 2019, p. 1.

² "The NUMEN Technical Design Report", International Journal of Modern Physics A (IJMPA), Volume No. 36, Issue No. 30, Article No. 2130018.

1.1 DCE process

In addition to other competitive reactions, the Double Charge Exchange process occurs in the MAGNEX scattering chamber when an ions beam collides with a target composed by a thin layer of carbon on which isotopes under analysis are deposited.

To produce the ions beam, a circular superconductor cyclotron K800 is used (figure 1.3). It is composed by three stages, and it uses Niobium-Titanium coils submerged in a Helium bath to produce a 4,8 T magnetic field. Once the ions beam has been accelerated up to the prescribed energy (in a range between 10 and 80 MeV/u) two electrostatic deflectors extract it and the beam is directed to the experimental hall.³

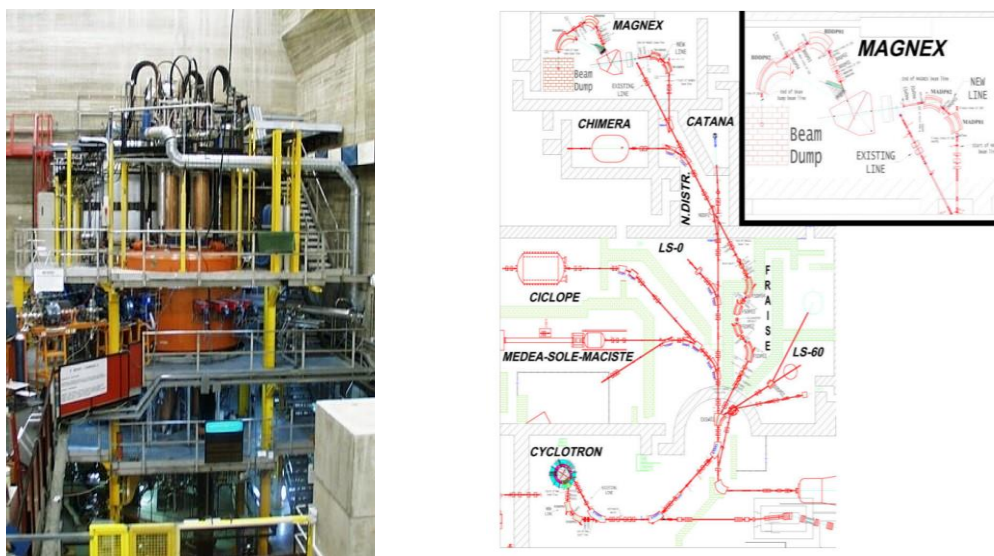


Figure 1.3: On the left: the actual K800 circular superconductor cyclotron installed at LNS. On the right: Plan of the LNS with represented the cyclotron position, the different beam lines, and the different experimental halls among which the MAGNEX experiment room. In the zoom on the top right is represented MAGNEX with the new high intensity beam line and the beam dump.

³ *Superconducting Cyclotron*, Ins.infn.it, <https://www.lns.infn.it/en/accelerators/superconducting-cyclotron.html>

Here the ions collide with the target inside the scattering chamber triggering to many reactions, among them the DCE. The particles produced by the nuclear reaction continue their path inside the MAGNEX apparatus which is a large acceptance spectrometer composed by a quadrupole, a dipole, and a focal plane detector (FPD) whose purpose is to detect the results of the collision and to produce the electric signals for the data acquisition system (figure 1.4).^{4,5}



Figure 1.4: Lateral view of the actual MAGNEX apparatus. In order from left to right: [1] MAGNEX scattering chamber, [2] MAGNEX quadrupole, [3] MAGNEX dipole, [4] focal plane detector, [5] rotary platform able to rotate, thanks to the rail [6], around the vertical axis passing through the target (in the center of the scattering chamber).

The ions beam enters the scattering chamber from left side of the image and, after colliding with the target positioned in the center of it (not visible from this view), continues its path through the window positioned behind the target.

⁴ MAGNEX, [lns.infn.it](https://www.lns.infn.it/apparati/magnex.html), <https://www.lns.infn.it/apparati/magnex.html>

⁵ F. Cappuzzello, C. Agodi, D. Carbone and M. Cavallaro, *The MAGNEX spectrometer: Results and perspectives*, Eur. Phys. J. A (2016) 52: 167. DOI 10.1140/epja/i2016-16167-1.

1.2 Upgrade of the NUMEN experiment

Until now, the NUMEN experiment has given great results in the study of the DCE processes. However, an upgrade of the cyclotron allows higher intensity ion beams and, therefore, it enables the acquisition of statistics in a shorter time increasing the knowledge related to the DCE process and indirectly to the $0\nu\beta\beta$.⁶

For this purpose, a new cyclotron will be installed in the “Laboratori Nazionali del Sud” in Catania, allowing to perform experiments using a high intensity ions beam. However, the use of a high intensity beam requires a complete redesign of most of the components and structures which meet the beam itself.

The new high intensity line must be installed with an angle of 70° with respect to the old one, the scattering chamber must be redesigned together with all the components connected to it, the focal plane detector must be strengthened by changing the already present detectors with new ones suitable to sustain a high rate beam, and a beam dump must be positioned after the FPD in order to extinguish the ions which do not collide with the target.⁷

In addition, the experiment must be able to adapt to both high and low intensity configurations. Therefore, the instruments necessary for the high intensity measurements should be able to move and/or be easily removed to allow the experiment to be configured for low intensity tests. The changing of configuration will be performed at least once a year and should be fast enough not to block experimental tests for too long.

⁶ NUMEN, [lns.infn.it](https://www.lns.infn.it/it/ricerca/progetti/numen.html), <https://www.lns.infn.it/it/ricerca/progetti/numen.html>

⁷ D. Sartirana, *Sistemi automatici per la movimentazione di bersagli per esperimenti di fisica nucleare*, Torino: Politecnico di Torino, 2019, p. 5.

1.3 Upgrade of the scattering chamber

The new scattering chamber has been designed by radically changing the shape and the dimensions of the actual one. A hemispherical enclosure made of aluminum will replace the actual cylindrical structure (figure 1.5). The global dimension will be smaller and most of the components currently contained inside the chamber will be positioned outside (e.g., the four copper sleds, the Faraday's cup,...). The new enclosure will have 6 mm thick walls against the 20 mm of the actual chamber in order not to interfere with the gamma rays produced at the target level after the interaction. Since a high level of vacuum will be maintained in the inside of the enclosure ($\sim 10^{-6}$ mbar), some reinforcements will be needed on the external surface to sustain the compressive forces coming from the environmental pressure.⁸

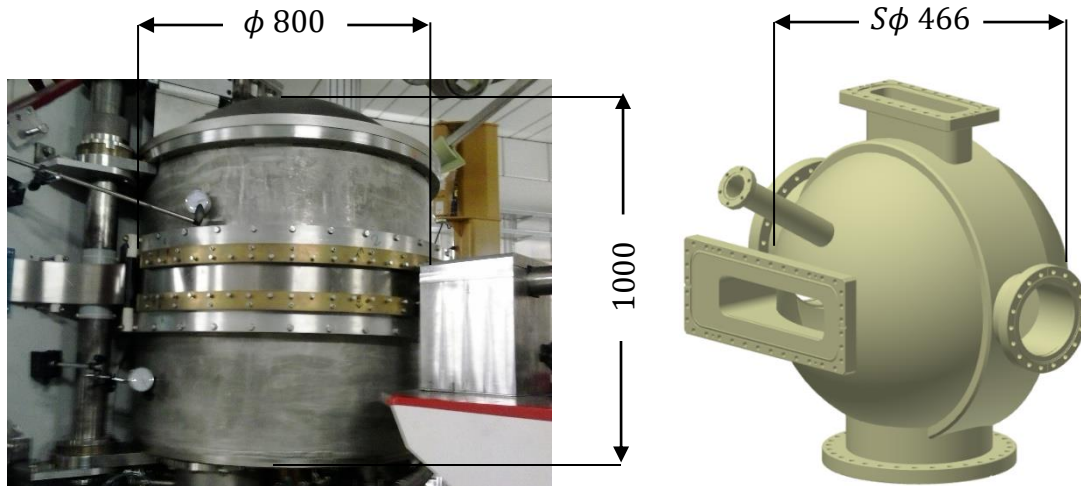


Figure 1.5: Comparison between the actual scattering chamber on the left and the new scattering chamber on the right. It is evident the difference in shape (cylindrical on the left and hemispherical on the right) as well as in the dimensions of the two chambers.

⁸ "The NUMEN Technical Design Report", International Journal of Modern Physics A (IJMPA), Volume No. 36, Issue No. 30, Article No. 2130018.

The new structure will be positioned on a solid sustain directly connected with the base of the experiment and it will have six main openings (figure 1.6):

- Frontal, connected with the high intensity line. [1]
- On the left, connected with the vacuum pump through a gate valve. This window allows also the robotic arm designed to automatically change the target to enter the scattering chamber.[2]
- On the right, allowing technicians to access the inside of the enclosure. [3]
- On the bottom, connected with the cryo-refrigerator structure which will be described later. [4]
- On the top, connected with the Faraday's cup. [5]
- On the back, connected with the MAGNEX quadrupole. [6]

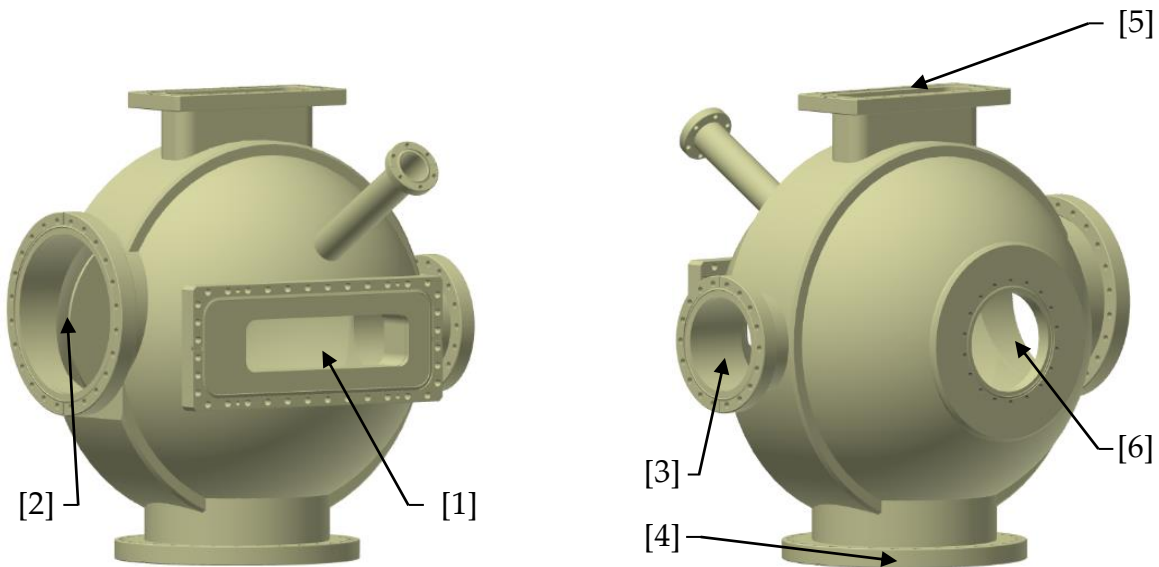


Figure 1.6: Axonometric views of the new MAGNEX scattering chamber with numbered openings referring to the above list.

Working with high intensity ions beam means having a high number of interactions between the ions themselves and the target. The collisions between the two release a high amount of energy which is partially transformed into heat. To maintain the target's temperature below a certain threshold, it must be set on a cryo-refrigerator whose work is to extract all the produced heat (figure 1.7). The selected cryo-refrigerator is composed by one stage, and it exploits a helium adiabatic expansion transformation which takes places inside a copper cylinder to reduce its temperature. The entire structure of the refrigerator can move vertically to align the center of the target with the ion beam.⁹

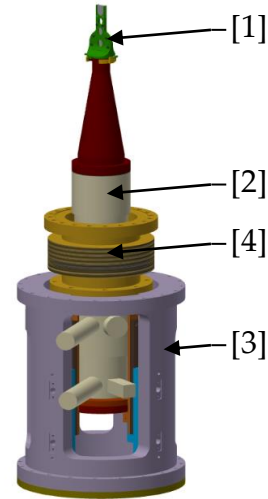


Figure 1.7: Representation of the mounting of the target holder [1] on the cryo-refrigerator [2]. Below, the cryo-refrigerator supporting structure [3] and the sealing system which allows the vertical movement [4].

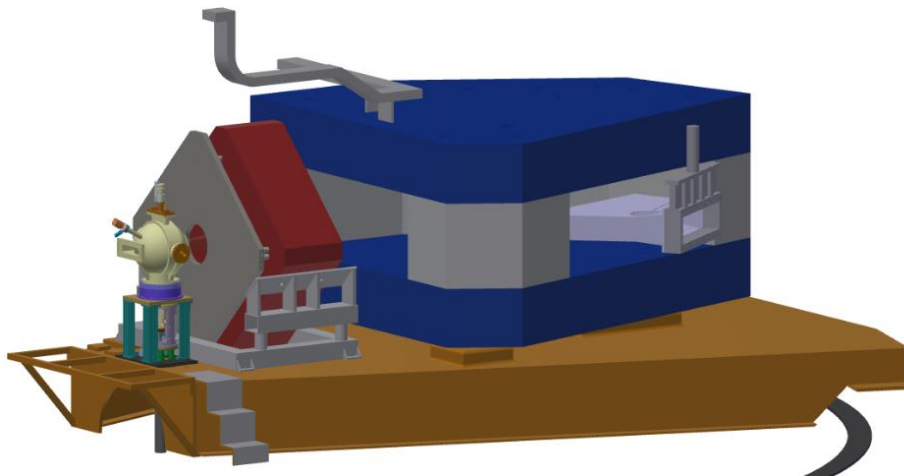


Figure 1.8: Simplified representation of the NUMEN experiment with the new scattering chamber (in yellow), the MAGNEX quadrupole (in red) and the MAGNEX dipole (in blue).

⁹ D. Sartirana, *Sistemi automatici per la movimentazione di bersagli per esperimenti di fisica nucleare*, Torino: Politecnico di Torino, 2019, p. 8.

1.4 Gamma detectors

The NUMEN experiment is not limited to the study of the particles detected by the focal plane only. Indeed, during the DCE process, a de-excitation of excited nuclei states occurs, producing gamma rays which are emitted in all the radial directions with respect to the target center. Therefore, all around the scattering chamber, a series of gamma detector are radially positioned (figure 1.9). These components detect gamma rays which are produced during the DCE process and generate an electric signal which is collected by the data acquisition system and subsequently analyzed.

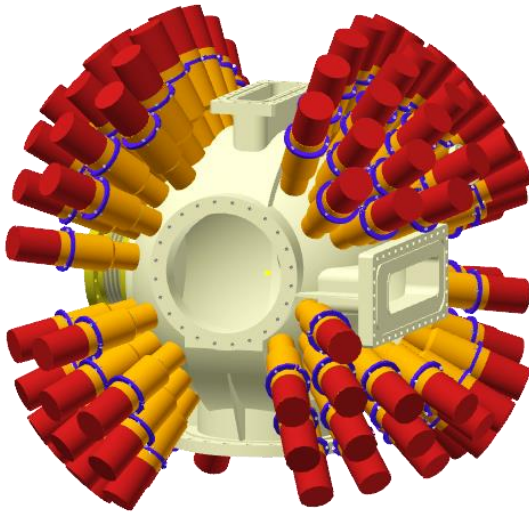


Figure 1.9: representation of the new scattering chamber (yellow), surrounded by the new gamma detectors (orange and red cylinders). The position of the detectors is optimized considering physical simulations and mechanical requirements.

Like the other components previously described, the gamma detector will also be redesigned both in terms of technology and positioning. Indeed, by moving them close to the center of the chamber, the gamma rays path length from the target to the sensor, and consequently the material encountered by the rays, are reduced, and the quality of the signal increases.

The design of a structure able to sustain the detectors in the correct position identified by physical simulations will be the main topic on which this thesis will focus on.

The new gamma detectors are still in the design phase, but they will be composed by three main parts (figure 1.10):

- One sensor composed by a lanthanum bromide scintillator able to capture the gamma rays and produce a photon signal. [1]
- One photocathode whose job is to convert the photons coming from the sensor into electrons, amplify them and produce an electric signal. [2]
- The electronics that manage the signal, powers the photocathode, and communicate with the data acquisition system positioned far from the experiment through a wiring. [3]

All the three components of the gamma detector are contained inside an aluminum cylinder, and they are shielded from external disturbs using a thin layer of Mu-metal. Each detector will weight around 700 g, but this value can still change since some changes are still being defined.

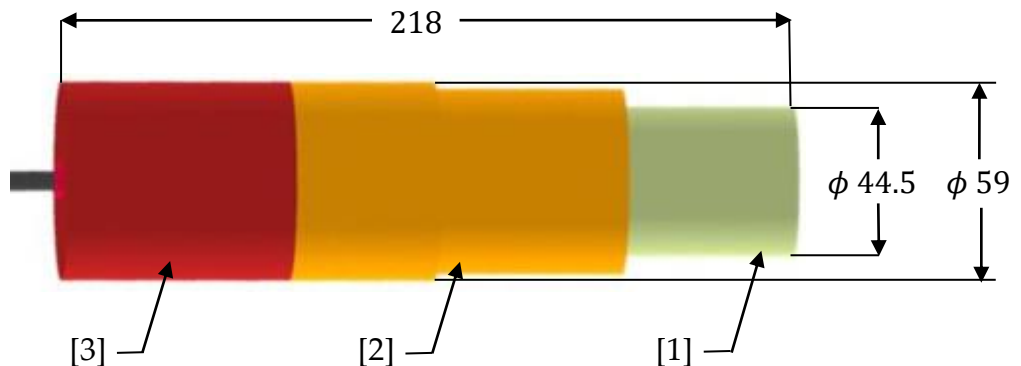


Figure 1.10: schematic representation of the new gamma detector's design. From left to right: the wiring exiting the detector (black), the electronics (red), the photocathode (orange) and the sensor (yellow).

The detectors will be mounted on an aluminum plate described later by means of a metallic collar which allows the cylinder to slide back and forth to set the correct distance equal to 240 mm of the sensor's face from the target's center.

2 Positioning of the gamma detectors

As previously said, the positioning of the gamma detectors close to the external surface of the scattering chamber is an important requirement to obtain better results in the study of the gamma rays emitted during the nuclear reaction. A proper structure designed to position and sustain the gamma detectors is needed since it is not possible to directly mount the detectors on the external surface of the enclosure. Indeed, the structure of the scattering chamber is not designed to sustain an external load since it has been optimized to sustain the pressure load caused by the vacuum and at the same time to be sufficiently thin not to interfere with the gamma rays.

2.1 Tasks of the support structure

The support structure must carry out several tasks: firstly, it must keep in the working position all the 112 detectors guaranteeing a precision with respect to the ideal position equal to 0,5 mm along the three principal axes X, Y and Z and 1° in the azimuthal and zenithal direction. Hence, the structure must have the possibility to be finely regulated along the six degrees of freedom (DOF) which characterize a body in free state (figure 2.1).

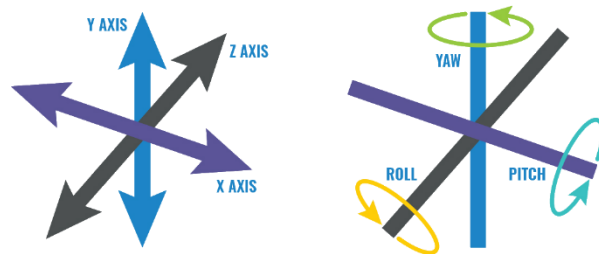


Figure 2.1: Representation of the six DOF which characterize a body in free state

Moreover, since the detectors may require some maintenance, the structure will be designed to semi-automatically move, when required, from the working

position to a maintenance position on the spectrometer platform, sufficiently far from the target to allow technicians to work on the detectors without being exposed to the induced radiation of the scattering chamber. Then, the same structure must be designed to sustain cables and the interconnection boards needed by the detectors to properly work.

2.2 Subdivision of the domain

Moving all the 112 detectors simultaneously is practically impossible since they are placed around a sphere and any movement will cause some sensors to touch the enclosure. To solve this problem the whole detectors' domain is divided into subdomains considering the geometrical constraints imposed by the nearby components. Four main subdomains have been identified (figure 2.2):

- One upstream inferior quarter which carries 25 detectors. [1]
- One upper hemisphere which carries 62 detectors. [2]
- Two downstream octants: one on the right and one on the left which carries 13 and 12 detectors respectively. [3] [4]

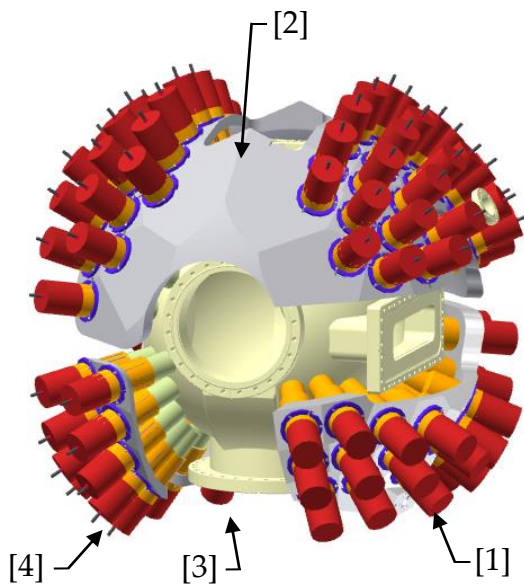


Figure 2.2: representation of the new scattering chamber (yellow), surrounded by the new gamma detectors (orange and red cylinders) kept in place by the four shells described above. The detectors are mounted on the shells by means of blue collars which are directly screwed to the shell.

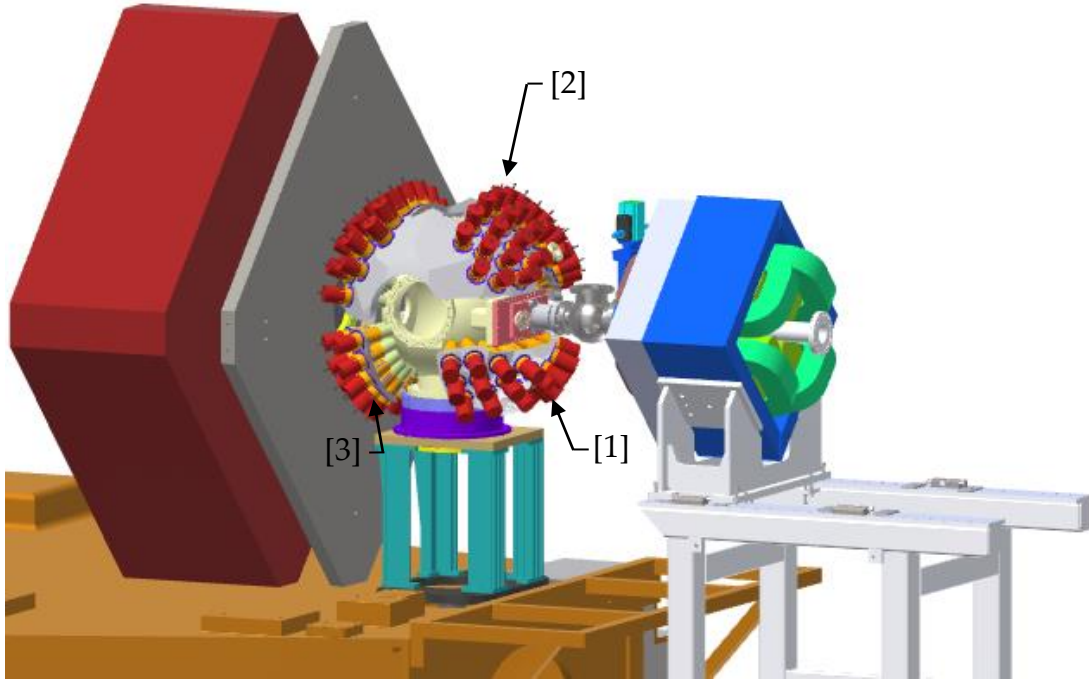


Figure 2.3: Simplified representation of the frontal part of the NUMEN experiment with the scattering chamber surrounded by the four detectors' supporting shells (shell [4] is placed behind the scattering chamber hence it is not visible).

Each subdomain is composed by an aluminum plate on which holes are made to accommodate the detector's cylinders. These holes must be oriented so that the axes of the detectors are all pointing the center of the target, so, a special machining operation must be performed to obtain the correct shape of the shell starting from the solid metal.

The division of the entire domain into subdomains allows to process a set of detectors as a single entity. Indeed, all the sensors belonging to the same sector are rigidly connected, decreasing the number of components to be oriented in space from 112 to 4. It is important to be noticed that each detector must be correctly positioned on each shell in radial direction before the shell is moved to the working position.

Each sector has its own reference system and moves along a specific path to reach a dedicated maintenance position. A proper study must be carried out in order to define a path for each sector which avoid the collision between the detectors and the components mounted in the proximity of the scattering chamber.

2.3 Subdomains' trajectories

Once the subdomains' structures have been designed, in order to understand how the support structure works, it is important to define the path that each sector follows from the maintenance position to the working one. The definition of the trajectories is a crucial point in the design of the supporting structures since they determine the number of DOF which characterize each structure and subsequently the number of actuators needed to obtain a fully automated movement.

Several paths have been simulated in the CAD environment with the help of a virtual instrument which generate an error in case contact occurs during the movement. Each of them displays some pros and cons which will be analyzed later to choose the best paths.

2.3.1 Upstream inferior quarter

Three different paths have been identified for this quadrant. Each of them is characterized by a first movement which takes the quarter to the free zone positioned below the high intensity line in between the scattering chamber support and the high intensity line structure [1]. Then, a second 500 mm movement allows the quadrant to horizontally slide below the beam's line and reaching a nearby maintenance position [2] (figure 2.4).

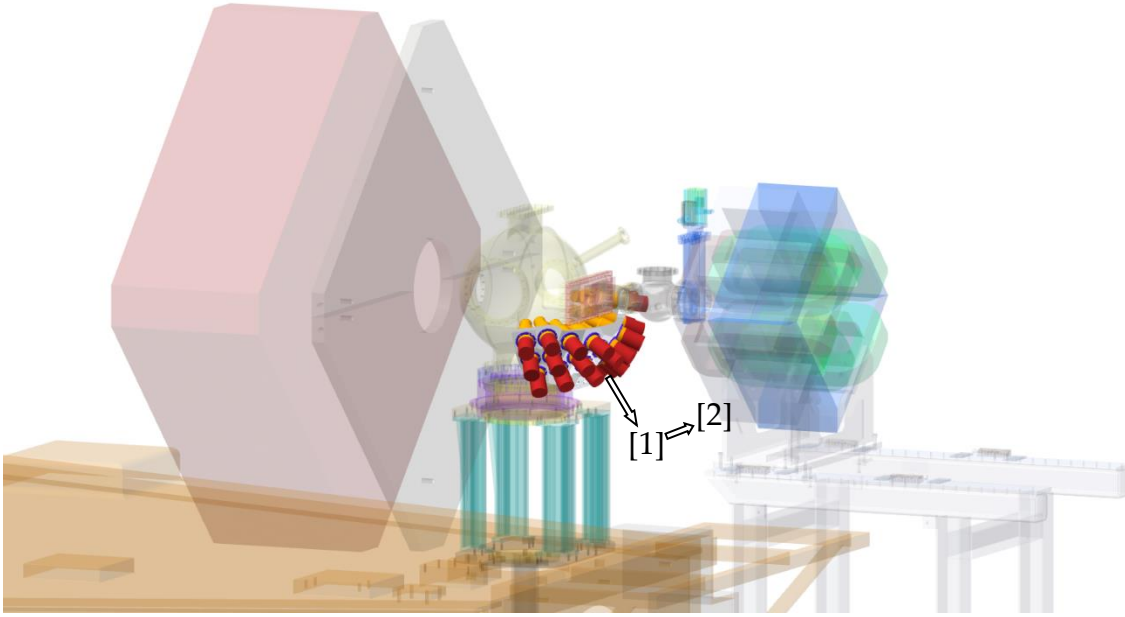


Figure 2.4: Global representation of the frontal part of MAGNEX with all transparent components except the upstream inferior quarter. The brackets identify the two main path zones (described below) in which the shell must pass to avoid collision with the high intensity line structure.

The three paths differ one from the other in the way the first movement is performed:

- OPTION 1: Linear translation composed of three movements.
This solution provides a sequence of three movements to reach the maintenance position (figure 2.5). A first 50 mm vertical displacement [1] is performed to avoid the collision between the shell and the line's connection flange and it is followed by a second 300 mm movement [2] along a 45° tilted line will disengage the quadrant from the nearby structure. The first 50 mm vertical movement is mandatory to avoid the collision between two lateral detectors and the scattering chamber's flange. Therefore, this solution requires a minimum of three actuator to fully automate the movements, but it does not need to remove any detector.

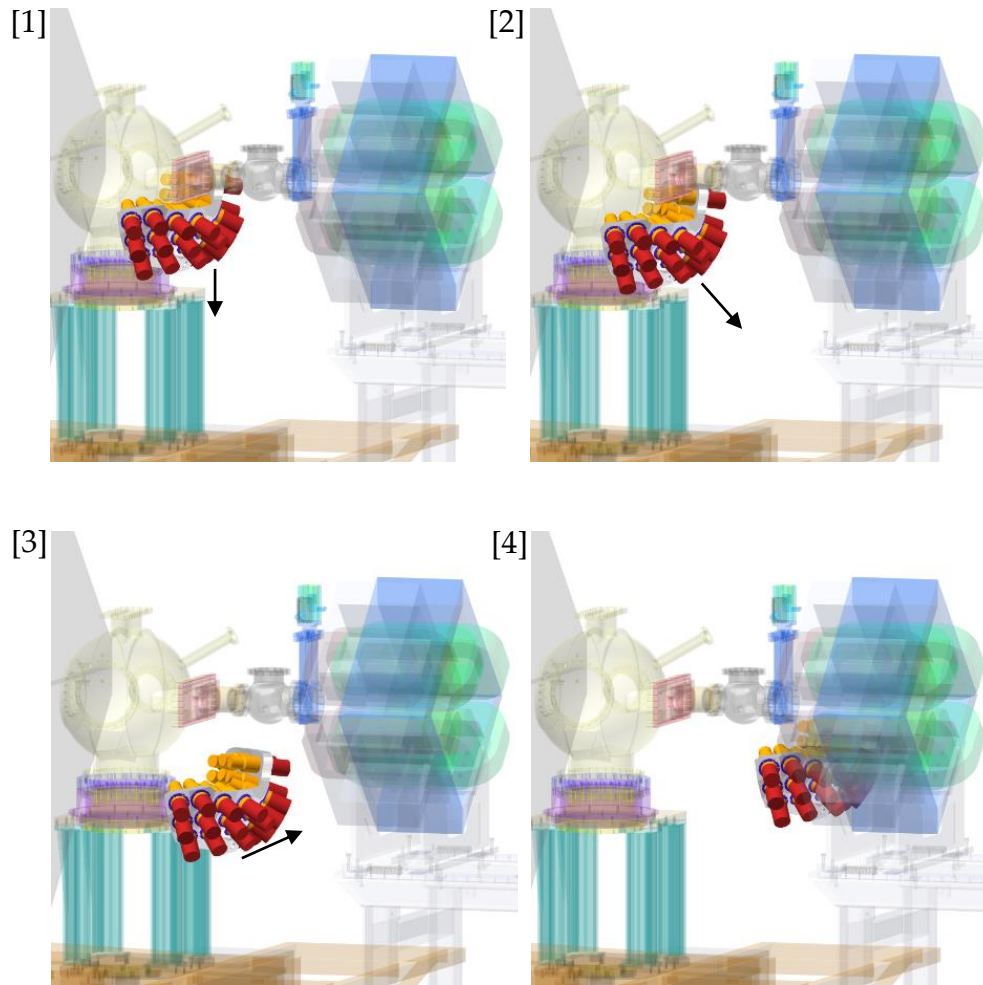


Figure 2.5: Upstream inferior quarter movement steps according to option 1.

- **OPTION 2: Linear translation composed of two movements.**
The second solution is like the first one, but it provides only two movements (figure 2.6). A first 150 mm slide [1] along a 40° tilted line allows the quarter to disengage the scattering chamber's structure, while a second 500 mm horizontal movement [2] takes the shell to the maintenance position. This solution needs only two actuators to perform the movement, but it requires to remove one lateral detector to avoid collisions.

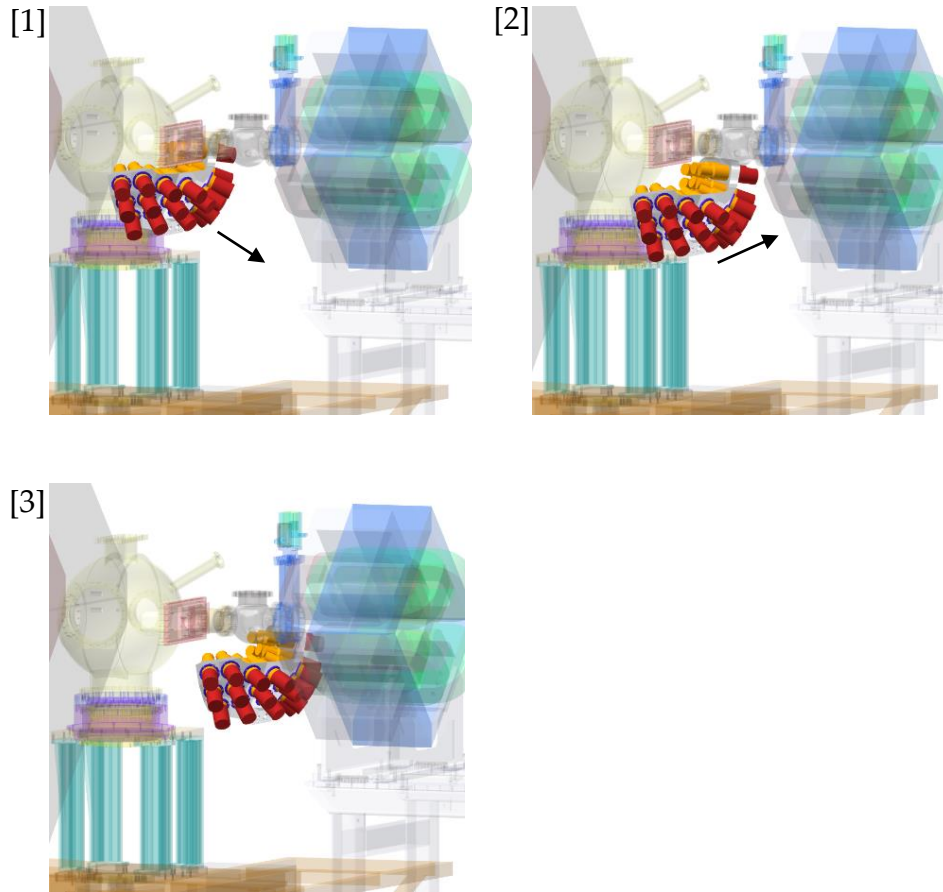


Figure 2.6: Upstream inferior quarter movement steps according to option 2.

- OPTION 3: Rotation of two octants around a vertical axis.
This last solution provides the subdivision of the quarter into two octants which can rotate around a vertical axis to disengage the scattering chamber's structure. Indeed, the first movement is composed by a 45° rotation of the two octants around the vertical axis, then, a second 250 mm vertical translation lower the structure below the beam line and finally a 500 mm horizontal movement allows to reach the maintenance position. This solution is much more complicated than the previous ones, but it does not need any detector to be removed and it requires two linear actuators and a rotary actuator. This last solution has not been simulated in the CAD environment. Therefore, the graphic representation is not available.

ORIGINAL SHELL VS REDUCED SHELL

As said before, the second option require the removal of one detector from the ideal number obtained from physical simulations to avoid the collision between the scattering chamber's supporting structure and the detector itself. Therefore, a reduced shell is designed by removing a lateral housing hole from the original one (figure 2.7).

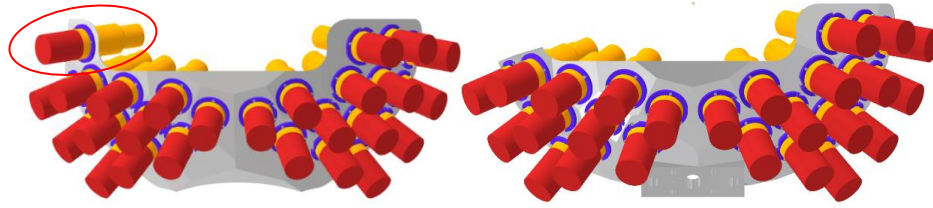


Figure 2.7: On the left side the original shell with 26 detectors.

On the right side the reduced shell with 25 detectors.

The analysis of the three possible solutions led to the choice of the second option. Indeed, even if this solution requires the removal of one detector, it is much easier than the other two to be performed. Moreover, removing the previously described detector avoids the possible collision between the detector itself and the system of pipes which can be required by the vacuum pump. This is also the cheapest solution since it requires only two actuators to obtain a fully automated movement of the support structure.

2.3.2 Upper hemisphere

The movement of the upper hemisphere does not require a particular study since the vertical translation [1] is the only choice to avoid the collision of the shell with the Faraday's cup without splitting into two quarter the entire shell. Moreover, the space over the scattering chamber is mostly free, so, once the hemisphere has been disengaged from the Faraday's cup, the movement to a maintenance position can be arbitrary chosen [2] (figure 2.8).

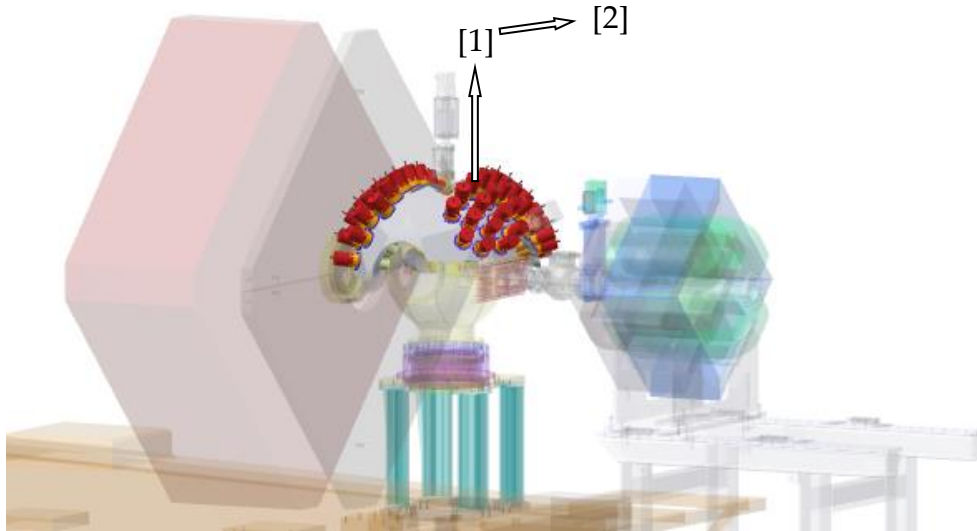


Figure 2.8: Global representation of the frontal part of MAGNEX with all transparent components except the upper hemisphere. The brackets identify the two main path zones (described below) in which the upper shell must pass to avoid collision with the Faraday's cup.

- Linear translation composed by two movements.

A first vertical linear movement [1] is performed to disengage the shell from the Faraday's cup. Then, a second horizontal translation [2] moves the hemisphere in a maintenance position. If needed, a third vertical movement can be implemented to lower the final position of the shell allowing an easier access to the detectors. This solution requires a minimum of 2 actuators to be performed.

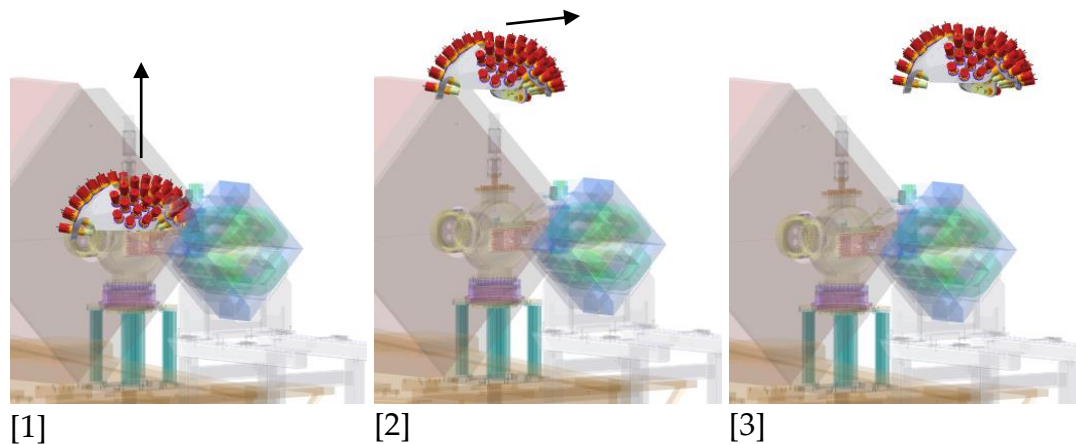


Figure 2.9: Upper hemisphere movement steps

2.3.3 Downstream right octant

The movement [1] of the rear right octant is not so critical since there are no components close to the shell on that side. The only constraint is that the final maintenance position must not be in the zone of the platform in front of the service stairs to allow technicians to stand near the scattering chamber (figure 2.10).

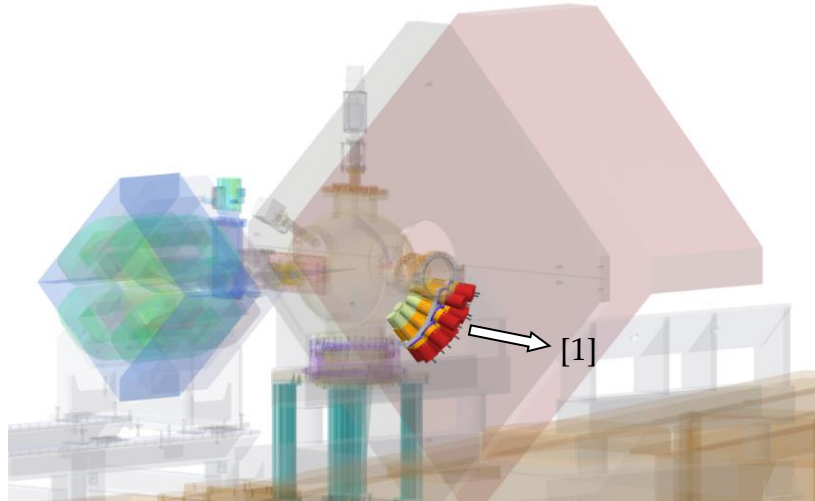


Figure 2.10: Global representation of the frontal part of MAGNEX with all transparent components except the downstream right octant. The bracket identifies the main path zone (described below) in which the shell must pass to avoid collision with the scattering chamber.

- Linear translation composed of one movement.

For this octant a single horizontal movement [1] is sufficient to disengage the shell from the scattering chamber (figure 2.11).

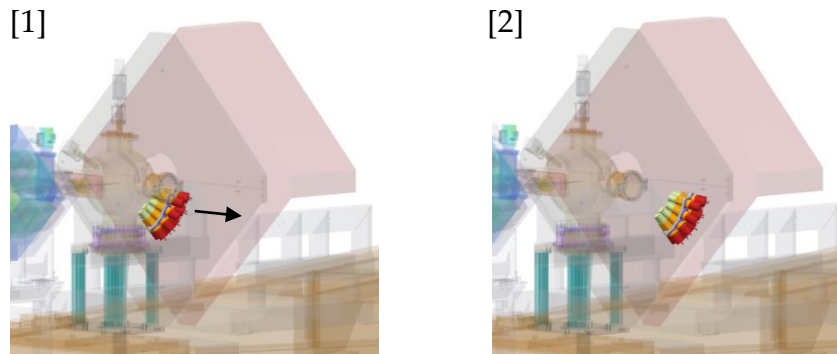


Figure 2.11: Downstream right octant movement steps.

2.3.4 Downstream left octant

The rear left octant is the more critical of the four shells since it is positioned in a small cavity between the scattering chamber and the MAGNEX shield (figure 2.12). Moreover, many other components are positioned in the proximity of this octant as the vacuum pump and the target manipulator which are not represented in figure 2.12 for ease of viewing. Then, finding a path to extract the shell from the cavity is complicated and some modification to the octant are necessary to avoid collisions during the movement. The selection of the correct path must then consider the complexity and the dimensions of the supporting structure since it must fit inside the previously described cavity.

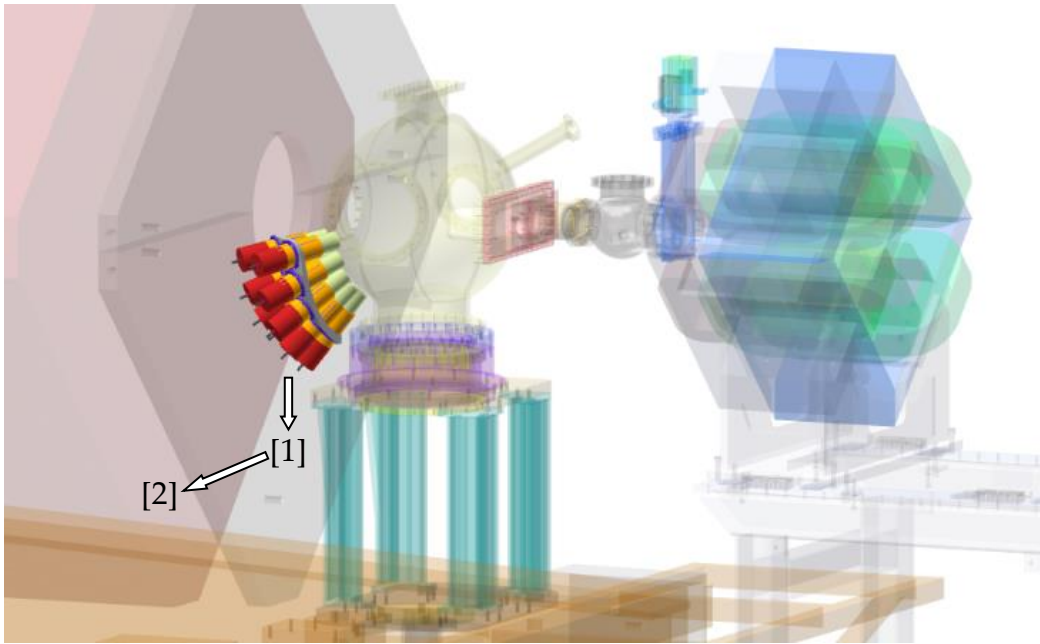


Figure 2.12: Global representation of the frontal part of MAGNEX with all transparent components except the downstream left octant. The bracket identifies the main path zones in which the shell must pass to avoid collision with the scattering chamber, the vacuum pump, and the target manipulator (not represented for ease of viewing).

Three different solutions have been found for this shell.

- **OPTION 1: Linear translation composed of three movements.**
This solution adopts three perpendicular movements to extract the octant from the cavity (figure 2.13). A first horizontal translation [1] allows to avoid the collision with the pump's collar, then, a second vertical translation [2] lowers the shell so that it can pass, with the third horizontal translation [3], below the manipulator's target holder. The three movements would require three actuators, however, since two translations are oriented along the same horizontal direction, the same actuator can be used to execute both the movements. To avoid collisions with the vacuum pump, the removal of three detectors is necessary (described later), nevertheless, the extraction of the shell is independent and do not require the removal of other components.

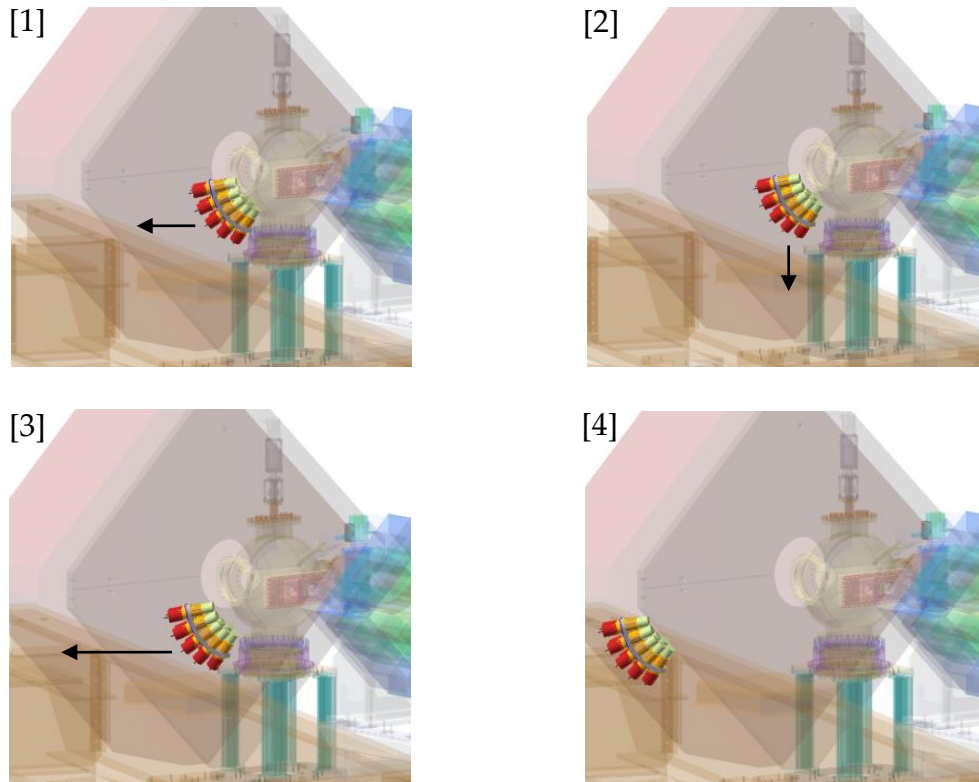


Figure 2.13: Downstream left octant movement steps according to option 1.

- OPTION 2: Linear translation composed of two movements.

The firsts two perpendicular movements of the previous solution are substituted by a single oblique translation. Then, a second horizontal movement slides the shell out of the cavity up to the maintenance position (figure 2.14). As in the first option the removal of three detectors is necessary to avoid the collision of the shell with the vacuum pump. This solution requires only two actuators, but it is slightly more difficult to design since the movements are not perpendicular, resulting in a system of linearly dependent translations.

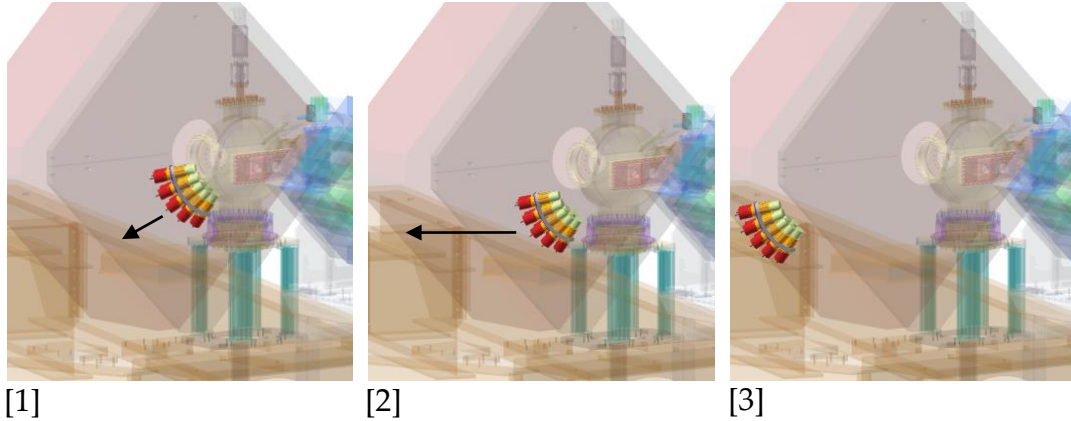


Figure 2.14: Downstream left octant movement steps according to option 2.

- OPTION 3: Rotation of the octant around the longitudinal axis.

This last solution is much more complicated than the previous ones since it is based on the rotation of the octant along the longitudinal axis corresponding with the ions' beam direction. By rotating the octant of 90° it will reach the upper part of the scattering chamber where it can be removed by performing a vertical translation like in the case of the upper hemisphere. The first rotation allows to avoid possible collision problems caused by the pump's pipes, but it requires to change the position of one of the four copper gates of the MAGNEX quadrupole. Even if the method

adopted in this solution is different from the first two, the removal of three detectors is necessary to avoid the collision of the octant with the pump's collar. Moreover, the extraction of the shell is not independent and first requires the upper hemisphere to move to allow the extraction of the octant. This last solution has not been simulated in the CAD environment. Therefore, the graphic representation is not available.

ORIGINAL SHELL VS REDUCED SHELL

As previously stated, all three options require the removal of three detectors from the ideal number obtained from physical simulations to avoid the collision between the pump's collar and the detectors. Therefore, a reduced shell is designed by removing three housing holes for the detector.

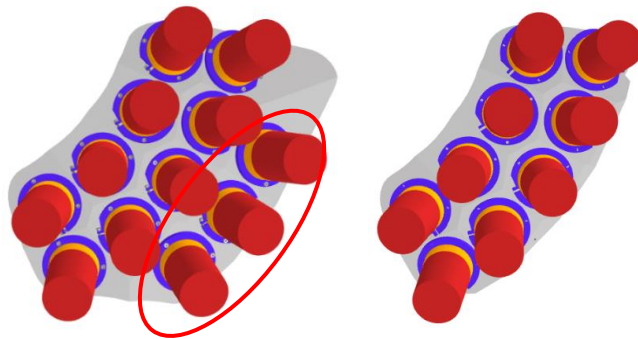


Figure 2.15: On the left side the original shell with 12 detectors. On the right side the reduced shell with 9 detectors.

As in the case of the frontal inferior quarter, the easiest and less expensive solution has been chosen. Therefore, the second option will be implemented since it requires only two movements and subsequently only two actuators. The first solution has been discarded since it requires an additional movement without adding any advantages with respect to the second case. The last solution has also been discarded for its complexity as it requires the redesign of the MAGNEX windows' system and the movement of the upper hemisphere.

3 Upstream inferior quarter's preliminary structure

The main purpose of this thesis is the study and the design of the support structure for the upstream inferior quarter (figure 3.1). The approach used in this part of the analysis is based on a trial-and-error strategy according to which a first design attempt is subsequently improved towards the best solution. Starting from a basic concept which will satisfy most of the requirements, a possible solution to the problem is found by iteratively changing the structure until all the construction requirements are satisfied.

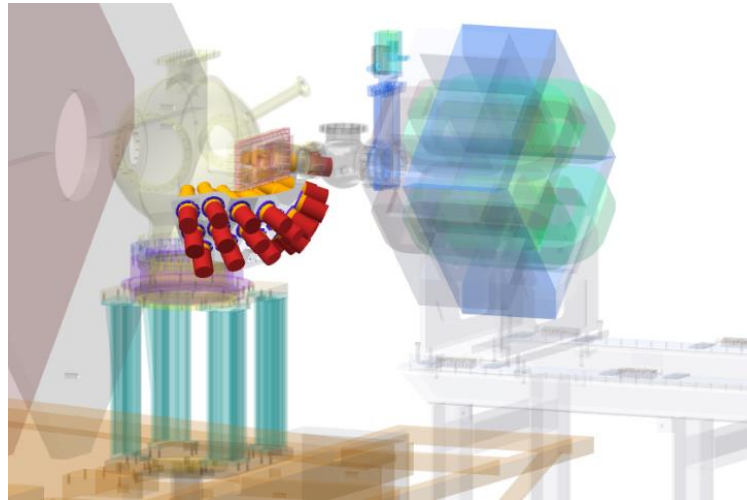


Figure 3.1: Global representation of the frontal part of MAGNEX with all transparent components except the upstream inferior quarter.

3.1 Requirements' analysis

Before moving to the design of the structure, a proper analysis is performed to understand which are the major properties that the structure must have to satisfy all the requirements. First, the structure must be designed in order to avoid collisions during the movement from the working to the maintenance position. So, the movement must follow one of the previously identified paths. Then, a six DOF regulation must be allowed by the structure to correctly position the shell in space

according to the imposed accuracy of 0,5 mm along the three main directions X, Y and Z and 1° in zenithal and azimuthal angular directions. Since the positioning calibration is a complex process, a proper system made of mechanical stoppers must be implemented to avoid the shell to be re-calibrated every time, thus guaranteeing the required repeatability. Moreover, the positioning precision of the shell is function of the mechanical properties of the entire structure, so a proper design and a flexural analysis of all the principal components must be performed. Another important property that cannot be neglected is the radiation resistance of all the used components. Indeed, as reported in literature, the mechanical properties of several materials are strongly affected by radiations ¹⁰. It is the case of some polymers used as piston's seals which can cause the gaskets an earlier loss of their sealing properties (figure 3.2).

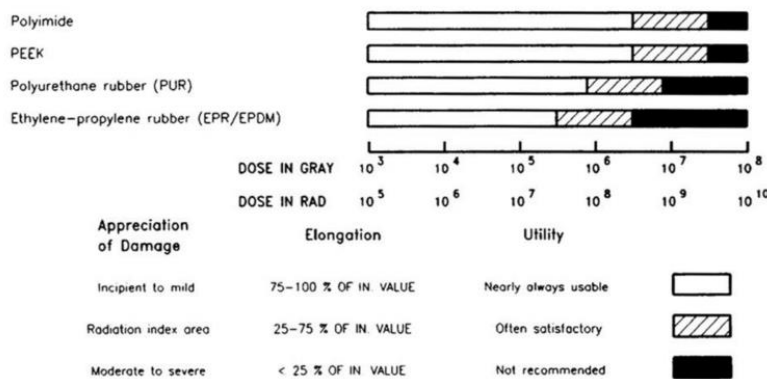


Figure 3.2: summary table of the effects of radiations on some plastic materials. The bars on the right allow to identify the operative range for different type of plastics depending on the equivalent radiation dose expressed in Grey (Gy).

¹⁰ CERN

Finally, the presence of a dispersed magnetic field imposed by the nearby MAGNEX's quadrupole can cause several problems to the electronic components. Therefore, if some electronics are required, they should be kept at a proper distance from the magnet or insulated with a protection shield.

3.2 Construction configurations

As previously stated, a preliminary structure which satisfies most of the requirements has been designed. Three different configurations have been developed in parallel to highlight the pros and the cons of each solution.

3.2.1 Central actuator with three cylindrical guides

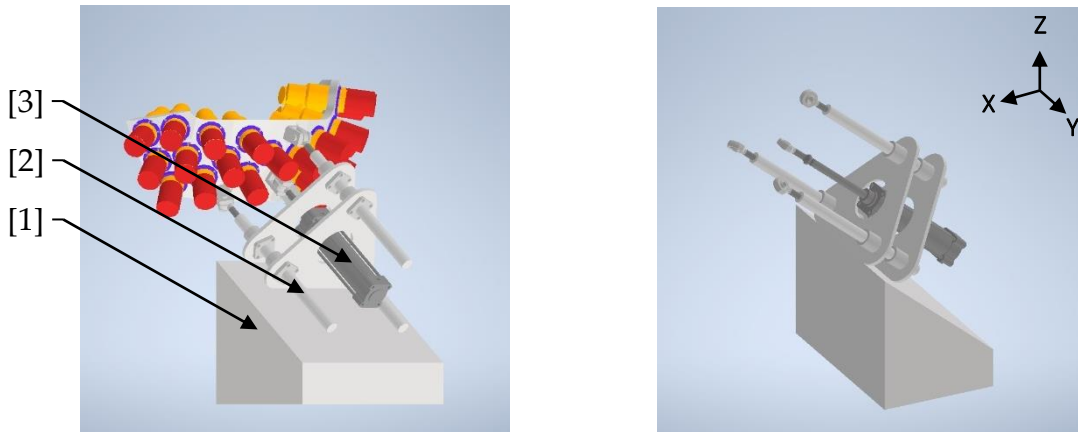


Figure 3.3: Representation of the support with the actuation structure fully designed (cylindrical guides [2], pneumatic actuator [3]) and the translating cart [1] schematized as a rigid parallelepiped structure. The two linear slides (not represented in figure) will be positioned below the cart allowing the lateral translation of the entire system.

This solution is composed by a base cart [1] able to horizontally translate over two linear slides (not represented in figure), that works as a support for a system composed by three cylindrical guides [2] and a pneumatic actuator [3]. The shell positioning procedure is composed by six steps:

- The base is translated from the maintenance position to the correct horizontal position (Y translation, see figure 3.3 for the reference frame).
- The actuator extends and moves the shell in oblique direction.
- Two of the three guides are blocked using pneumatic clamps (to be implemented in the CAD model).
- The X, Y and Z stoppers are regulated to impose the correct positioning of the shell along the three principal directions (to be implemented in the cart structure).
- The length of the two blocked guides is modified to impose the correct orientation to the shell (acting on the threaded end of the guides, that are connected to the shell by means of spherical joints), allowing the system to reach the working position.
- The free guide is blocked.

The idea behind this solution is that the three adjustments along X, Y and Z are assigned to three mechanical stoppers mounted on the base cart, while the adjustment of the pitch, yaw and roll are assigned to the system of cylindrical guides. Indeed, since the movements required for the adjustments are very small, it is possible to change the length of each guide to determine the position of three points of the shell which characterizes the unique detectors' orientation. The third guide must be free to move to avoid problems connected with hyperstaticity and it can be arbitrary chosen. It must follow the movement imposed by the variation of length of the other two guides and it can be blocked with a third pneumatic clamp only when the system reaches the steady state. The length variation of each guide is performed by acting on the bolted joint between the guides and the spherical joints mounted at their end when the guides have already been blocked by the

clamp. The distance between the detectors and the target can be imposed by acting on a mechanical stopper which limit the stroke of the pneumatic actuator. The three guides must be properly chosen in diameter to sustain all the weight of the shell since the actuator's rod is not designed to sustain radial load. In this first solution the pneumatic actuator does not require an integrated clamping mechanism since the shell is maintained in place with three blocked guides which allow the actuator to be discharged.

3.2.2 Lateral actuator with two cylindrical guides

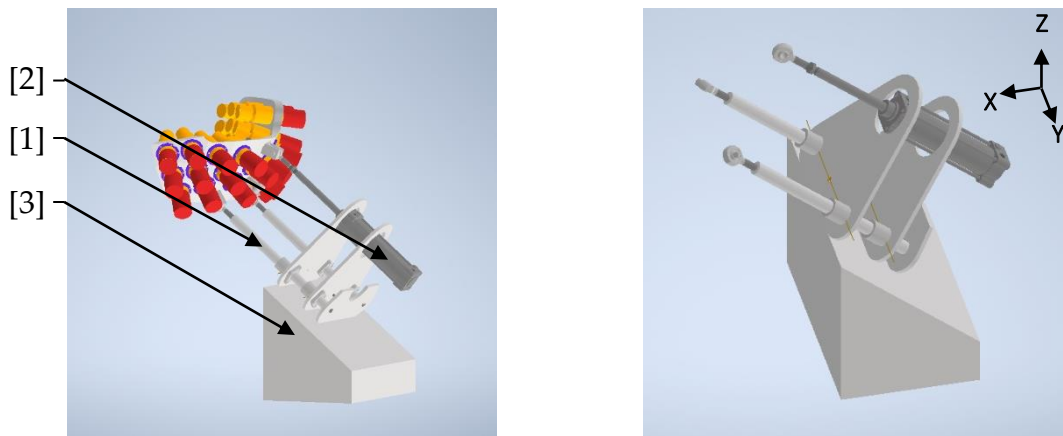


Figure 3.4: Representation of the support with the actuation structure fully designed (cylindrical guides [1], pneumatic actuator [2]) and the translating cart [3] schematized as a rigid parallelepiped structure. It differs from Figure 3.3 in the way the actuation elements are arranged.

This solution allows to avoid the problems connected with hyperstaticity by removing one of the three cylindrical guides [1] and by moving the actuator [2] in a lateral position. The positioning process is composed by 5 steps:

- The base is translated from the maintenance position to the correct horizontal position.
- The actuator moves the shell in oblique direction.

- The two guides are blocked using pneumatic clamps.
- The X, Y and Z stoppers are regulated to impose the correct positioning of the shell along the three principal directions.
- The length of the two blocked guides is modified to impose the correct orientation to the shell.

For this solution it is crucial to pay attention to the size of the guides since a relevant load can be discharged on the actuator rod, causing its bending. Moreover, the system is not balanced, and the extension of the actuator will inevitably rotate the whole shell causing it to hit the scattering chamber. Then, a proper system needs to be implemented to avoid this rotation.

3.2.3 Three pneumatic actuators

This solution solves both the hyperstaticity and the unbalancing related problems by substituting the cylindrical guides with three electrical actuators. Nevertheless, the weight of the shell will be supported by the actuators' rods, components which are not designed to resist to tangential load. To solve this problem guided actuators can be used, but they are much more expensive and require more maintenance. This last solution has not been represented in CAD environment due to the high cost, so a render of this structure is not available.

The positioning procedure is composed by four steps:

- The base is translated from the maintenance position to the correct horizontal position.
- The actuators move the shell in oblique direction.
- The X, Y and Z stoppers are regulated to impose the correct positioning of the shell along the three principal directions.

- The actuators' length is finely adjusted to correctly orient the shell in space.

Since the final position adjustment is directly assigned to the actuators, high precision linear actuators must be used. For this purpose, electrical actuators are more suitable than pneumatic ones since they can reach a higher accuracy using stepper motors and resolvers. This solution allows an automatic positioning of the shell which can be performed far from the scattering chamber, and it also solve the radiation degradation problem of the pneumatic actuators' seals. Nevertheless, using three electric actuators increases the total cost of the structure and the electronics can be susceptible to the dispersed magnetic field produced by the nearby quadrupole.

3.3 Development of the second configuration

After a feasibility analysis of the three configurations, the second one, based on a lateral actuator and two cylindrical guides, is selected as a starting point for the model implementation. Indeed, this configuration simplifies the positioning procedure, and it solves the problem of hyperstaticity. Moreover, the use of a single pneumatic actuator reduces the total cost of the structure making this solution more affordable than the others. Nevertheless, proper modification to the above represented structure must be done to solve the previously described balancing problem. Indeed, the lateral positioning of the actuator with respect to the barycenter of the shell will cause the entire structure to rotate when the actuator is extended.

To solve such behavior, it is possible to use an actuator with through rod [1] which allows the connection of both the cylindrical guides with the actuator by means of a metallic plate (figure 3.5).

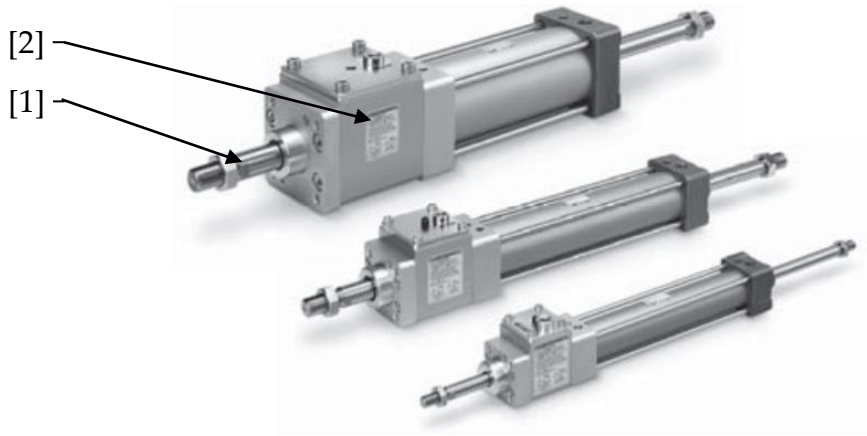


Figure 3.5: SMC through rod [1] actuators of the MWBW series with different piston diameters. They all have a pneumatic block [2] that can stop the rod at a precise stroke ¹¹

In this way, the translation of the rod will cause the two guides to follow the movement avoiding the rotation of the shell. Moreover, if an actuator with an integrated block [2] is used, the two pneumatic clamps used to stop the cylindrical guides in position could be avoided since the guides will be sustained directly by the actuator. This solution requires an appropriate design of the connection plate, that must resist the bending effect due to the longitudinal weight coming from the two cylindrical guides.

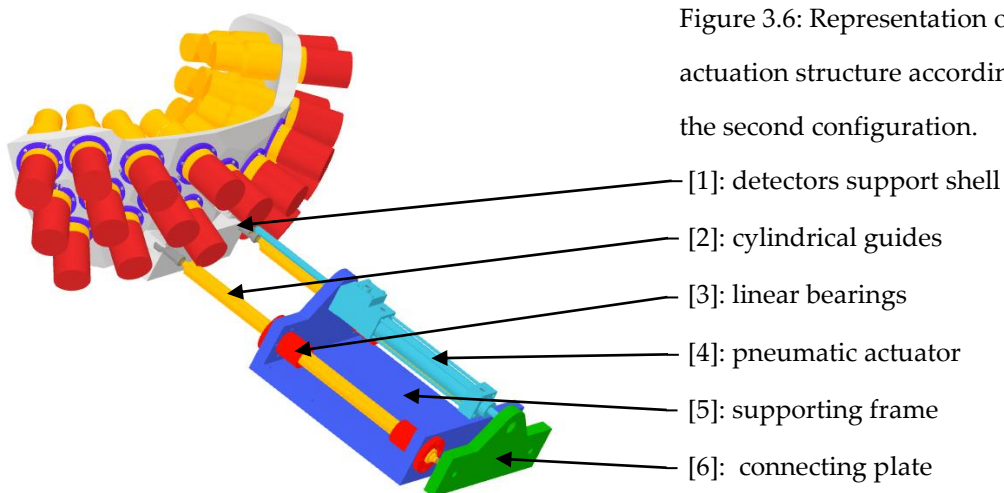


Figure 3.6: Representation of the actuation structure according to the second configuration.

¹¹ SMC, "Cylinder with lock, MWB series", p. 18.

Moreover, a structural analysis on the actuator rod must be performed to understand if it is suitable for the application. The use of a connecting plate allows another important modification to the regulation system. Indeed, the connection between the rod and the guides allows to change the length of the guides acting on a threaded connection positioned far from the shell, thus allowing an easier access to the regulation system. For this purpose, grooved guides must be used to avoid the rotation along the longitudinal axis during the regulation (figure 3.7).



Figure 3.7: MISUMI grooved guide of the BSYM series with one end stepped and threaded and a cylindrical linear bearing mounted on it. ¹²

3.4 Sizing of the components

Once established the general set-up for the system, a first sizing attempt is made to select the components from industrial catalogs and to start working on the CAD drawings.

3.4.1 Grooved guides' diameter

First, a bending analysis of the two grooved guides is performed at their maximum extension. Doing so, it is possible to determine the minimum diameter of the guides which guarantees a maximum deformation consistent with the actuator's rod. For this purpose, a simplified cantilever model is considered (figure 3.8).

¹² "Ball Splines/One End Stepped and Threaded", <https://uk.misumi-ec.com/>,
<https://uk.misumi-ec.com/vona2/detail/110302402950/?CategorySpec=00000421500%3a%3ab>

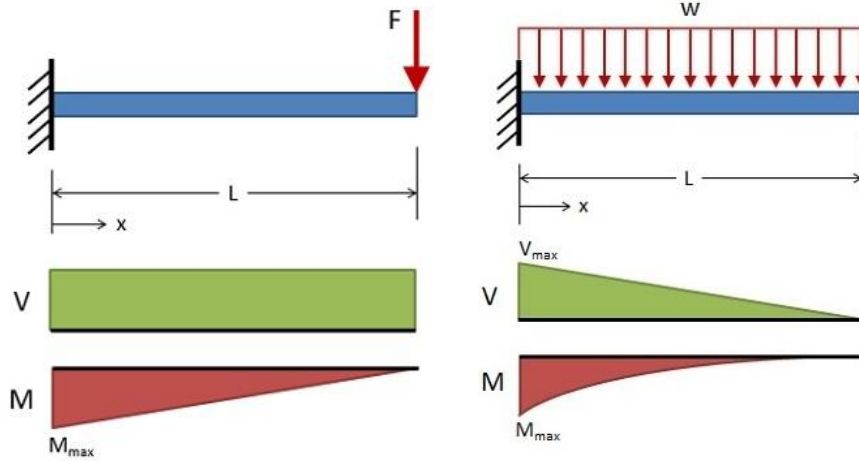


Figure 3.8: Cantilever beam stress analysis schemes for point load (on the left) and distributed load (on the right). The green distribution refers to shear tension and the red one to moment computed in each longitudinal section.

Before computing the deformation, the total weight of the suspended mass is calculated. It considers both the concentrated and the distributed weight forces.

The concentrated forces are composed by:

- Weight of the shell (considering three different materials: AISI 304, Anticorodal and Ergal).
- Weight of the detectors.
- Weight of the supporting collars.
- Weight of the universal joints.
- Weight of the screws.

The distributed forces consider the grooved guides' weight.

Since the system is tilted by a 40° angle, the total weight has been decomposed in the longitudinal and tangential components (figure 3.9).

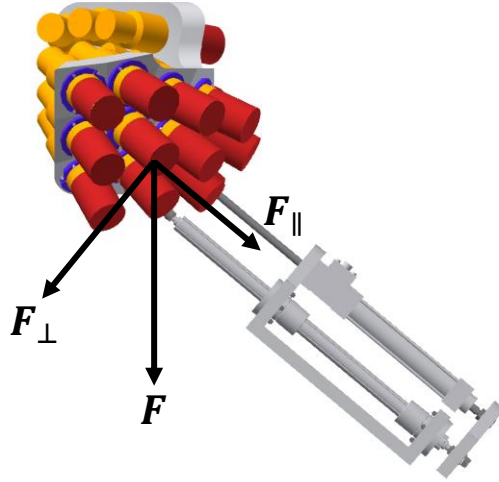


Figure 3.9: Schematic representation of the actuation structure with the weight force vector F and its decomposition in longitudinal F_{\parallel} and radial F_{\perp} directions.

Then, given the Young modulus, the moment of inertia and the length of the grooved guides, the total bending deformation is computed:

$$\delta = CS * \frac{\frac{F}{2} L^3}{3EI}$$

where:

- CS: is the safety factor which has been imposed equal to 3.
- $F/2$: half of the tangential load since the weight is supported by two guides [N]
- L: length of the cantilever [m]
- E: stainless steel Young modulus [N/m²]
- I: moment of inertia of the 30 mm guides [m⁴]

All the data needed for the calculations are collected in an Excel file and are not reported here. They are obtained from the CAD model and from the technical data sheets of the materials.

Since the specific weight of the three materials used for the shell is different, the total deformation computed assumes different values:

- AISI 304: 0,718 mm.
- Anticorodal: 0,515 mm.
- Ergal: 0,513 mm.

These results will be compared with the maximum actuator's rod deformation to understand whether the diameter of the guides is sufficiently large or it must be increased to lower the total deformation of the system.

The theoretical results were compared with the ones coming from the FEM analysis performed in the Inventor environment and a great difference between the two was observed. This is due to the high level of simplification used both in the FEM, where the system is approximated as a cantilever beam, and in the theoretical model. To obtain similar results between the two approaches, the threaded part of the guides and the extra length of the universal joints must be included in the computation. Nevertheless, this computation is purely indicative and will not be used in the next chapters of this thesis.

3.4.2 Actuator diameter

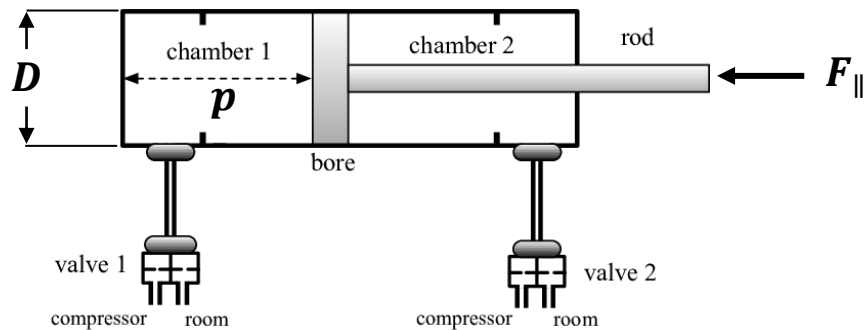


Figure 3.10: Simplified representation of a pneumatic actuator.

Since the longitudinal load discharged on the two guides has already been computed and it is fully sustained by the actuator, the minimum diameter of the piston can be computed:

$$D = \sqrt{\frac{4F_{\parallel}}{\pi p \eta}}$$

where:

- F_{\parallel} : total longitudinal load discharged on the piston's rod. [N]
- p : supply pressure (assumed 6 bar) [bar]
- η : efficiency of the actuator imposed to 0,9.

Even in this case the three different materials of the shell have been considered in the computation of the actuator's diameter giving as results:

- AISI 304: 25,471 mm
- Anticorodal: 21,418 mm
- Ergal: 21,358 mm

Then, even the SMC¹³ smallest actuator ($\phi 32$) of the MWB series is sufficient to ensure the extension of the rod under the shell's load (figure 3.11).



Figure 3.11: Render of the MWBW 32_160 SMC pneumatic actuator

¹³ SMC Corporation, Sotokanda, Chiyoda-ku, Tokyo 101-0021, Japan

3.4.3 Sustain plates

Once the guides and the piston's diameters are computed and the commercial components selected from proper catalogs, it is possible to proceed with the 3D modelling of the sustain plates used to connect the guides, the actuator, and the translating cart one with the other. A first design attempt is implemented in the Inventor environment considering the dimensions of each normalized component (figure 3.12). Special attention has been paid to the way the three sustain plates are connected one with the other choosing M6x1,5 calibrated bolt connections with reference pins to obtain a precise assembly of the frame. The sustain plates can accommodate the actuator and the two cylindrical guides thanks to five holes. The actuator is supported by the frontal plate only to avoid problems connected with the hyperstaticity of the structure. The sizing of the plates and bolts will be described later since it has been performed only for the final design solution.

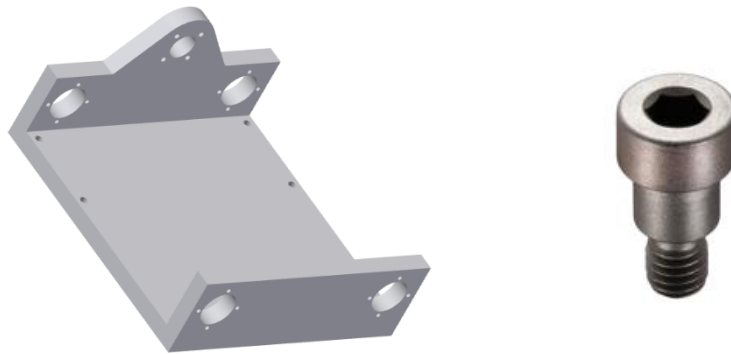


Figure 3.12: On the left: Render of actuation structure's sustain plates.

On the right: calibrated bolt with hex slot on the head.

3.5 Cart

The whole previously described structure composed by the actuator, the two guides and the sustain plates will be mounted on a sliding cart responsible for positioning the entire structure along the X, Y and Z directions.

A 50x50x5 mm tubular welded structure is designed to accomplish this role (figure 3.13).

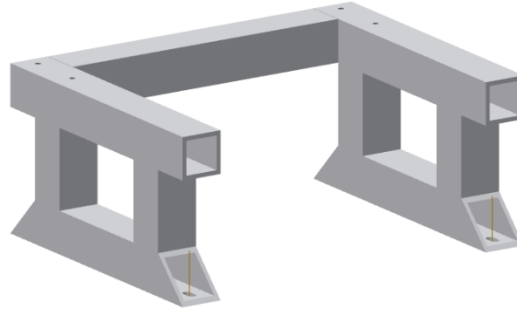


Figure 3.13: Tubular welded structure composing the upper part of the translating cart

The whole cart is divided into two main parts: the tubular welded structure [1] and the base plate [2], connected by means of four levellers [3] which allow a precise regulation of both the vertical and the longitudinal position by means of a system of slots realized on the tubular structure [4] (figure 3.14).

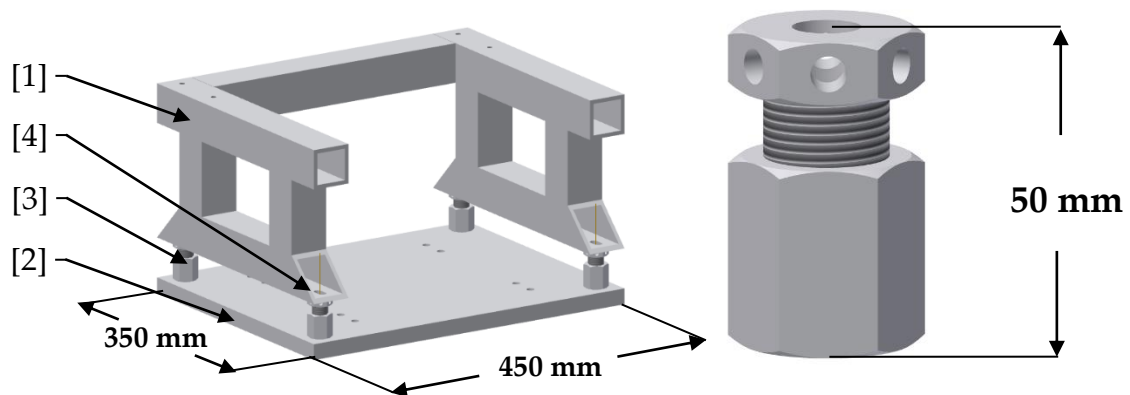


Figure 3.14: On the left: whole cart representation with the tubular welded structure [1], the base plate [2], the four levellers [3] and the slots [4].

On the right: render of the leveller composed by a bolt and a nut whose reciprocal position can be manually set by acting on the threaded connection.

The longitudinal positioning of the upper part of the cart can be set acting on a threaded stopper (not represented in figure), while the vertical positioning is obtained by directly acting on the height of the levellers. The entire cart is mounted on a sliding system composed by two linear guides which allow the horizontal movement of the structure (figure 3.15).

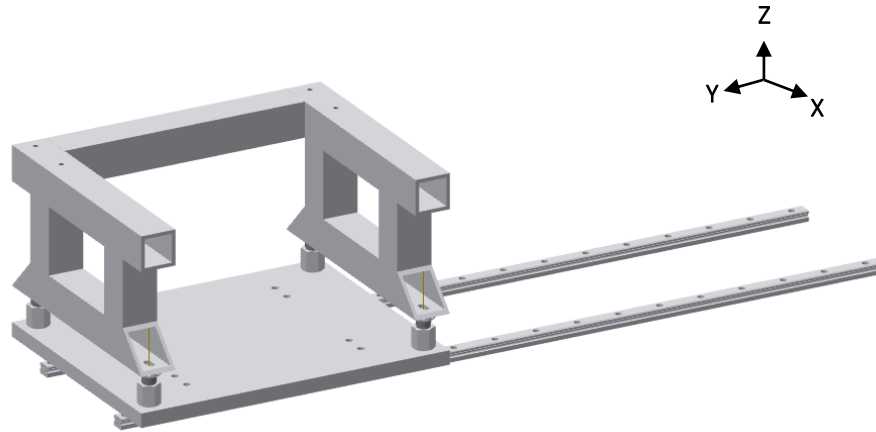


Figure 3.15: Representation of the translating cart mounted on the two linear guides by means of four cursors bolted behind the base plate.

The fine positioning along the horizontal direction is obtained by means of a threaded stopper (not represented in figure) which imposes the correct position along the Y direction of the whole cart. To block the cart in place a manual clamp system is mounted on the guides behind the base plate (figure 3.16).



Figure 3.16: Zimmer manual clamp system for linear guides of the HK series

The connection between the cart and the automation structure composed by the actuator, the two guides and the sustain plates is entrusted to a system of bearings which allows the upper structure to rotate around a shaft changing the angle of attack of the shell (figure 3.17).

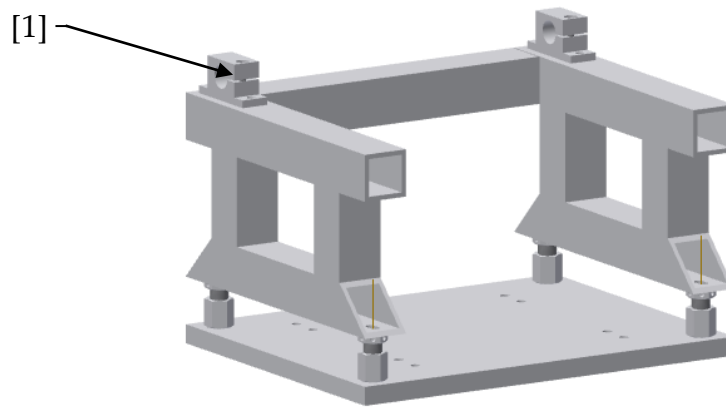


Figure 3.17: Representation of the translating cart with the system of bearings

[1] bolted on it.

The correct angle is imposed by means of a threaded stopper (not represented in figure) which act as a counterpart in the rotation movement of the structure limiting the rotation and imposing a certain angle.

The horizontal movement of the entire cart is performed manually. The design of a sufficiently long handle allows to translate the cart by hand without entering the dangerous radiation zone. Then, a proper handle is designed so that the movement can be performed both from the ground or from the Numen platform (figure 3.17).

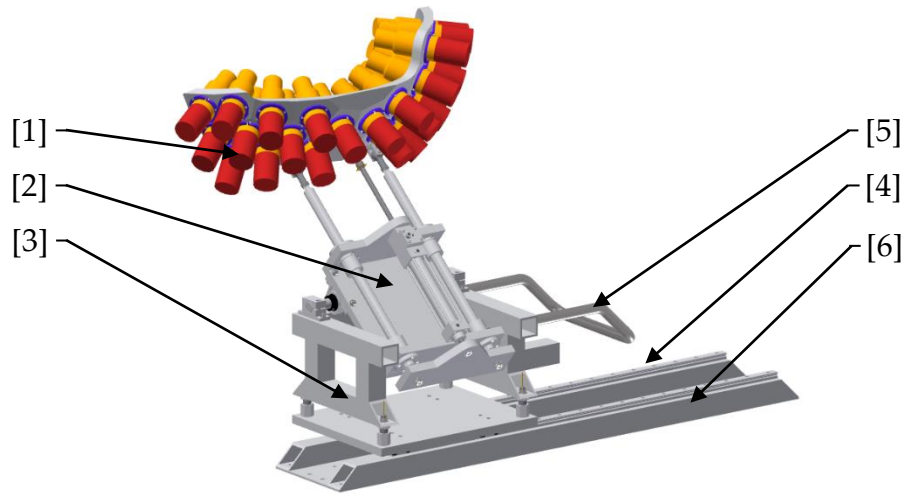


Figure 3.17: Representation of the upstream inferior quarter support structure with all the main components: [1] upstream inferior quarter, [2] actuation structure, [3] translating cart, [4] system of linear bearings, [5] handle, [6] supporting base.

Once the CAD design of the cart is completed, a proper solution to accommodate the wiring coming from the detectors is studied. Since it could be needed to repair each detector singularly, a patch panel mounted on the cart could drastically reduce the disassembly time, allowing to quickly isolate the detector from the data acquisition system. Then, a structure to support the patch panels is integrated in the cart design (figure 3.18). The patch panel structure is designed, in this early stage, as a metallic plate on which 50-ohm BNC connectors are uniformly mounted allowing the rapid disconnection of each detector's cable from the long cable coming from the data acquisition system. Since the shell is symmetrical with respect to the cart, two identical patch panels are mounted on the two sides of the cart reducing the distance of the detectors from the patch panels themselves.

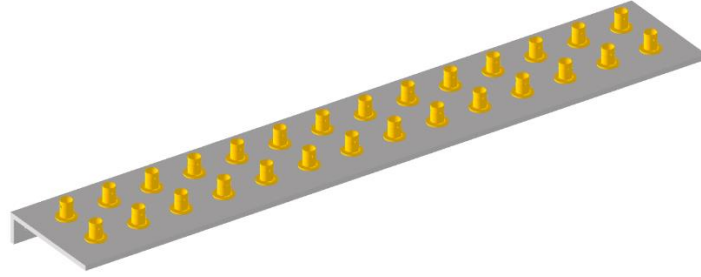


Figure 3.18: Patch panel for both the power supply and the electric signal which can power up to 14 detectors. The BNC connectors are linked to the detectors from the top and to the data acquisition system from the bottom.

Moreover, since from the maintenance to the working position the cart follows a linear horizontal path, a cable drag chain must be used to facilitate the wiring roll-up and unroll during the movement. Thanks to the two linear guides which lift the cart structure from the Numen platform, a suitable space for the cable drag chain is obtained under the cart itself, allowing a more compact design for the structure avoiding the positioning of the drag chain beside the cart (figure 3.19).

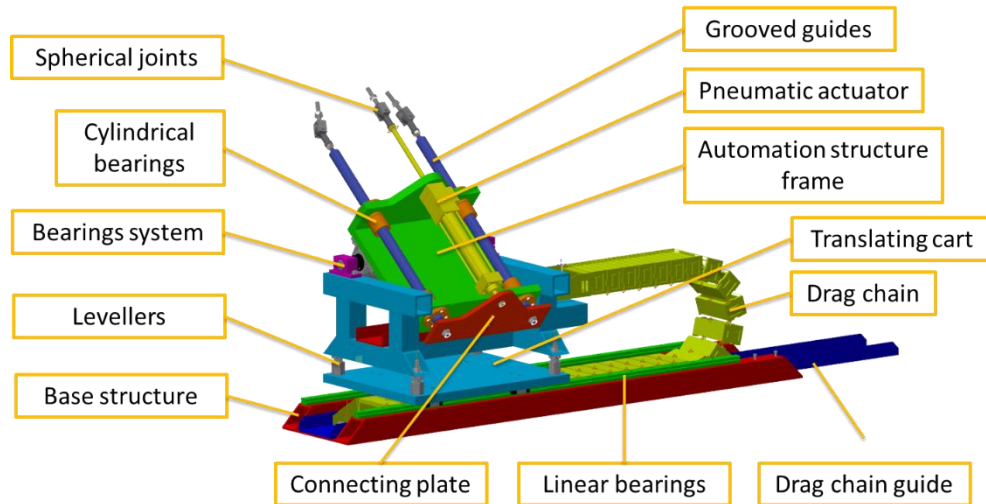


Figure 3.19: Upstream inferior quarter supporting structure with all the main components included the drag chain.

3.6 Global consideration on preliminary solution

The previously proposed solution is a good starting point for the design of a final sustain structure. Indeed, it satisfies most of the problem's requirements and, at first glance, it seems very simple to be used.

However, during the design, some criticalities connected to the positioning regulation system emerged and a proper solution must be found to obtain a working system. The main criticalities are directly connected with the six fine regulations that the system must be able to perform. First, the kinematics of the proposed solution has not been solved yet since it can be very complex due to the mutual dependence of the regulations. Then, even if the starting and the final position are known, it is not easy to define which regulations must be performed to reach the final configuration. Moreover, the system used to modify the azimuthal and zenithal orientation angles has a geometrical problem which does not allow the orientation to change. Indeed, the fixed center distance between the three spherical joints connected to the shell does not allow the length of the cylindrical guides to be modified independently.

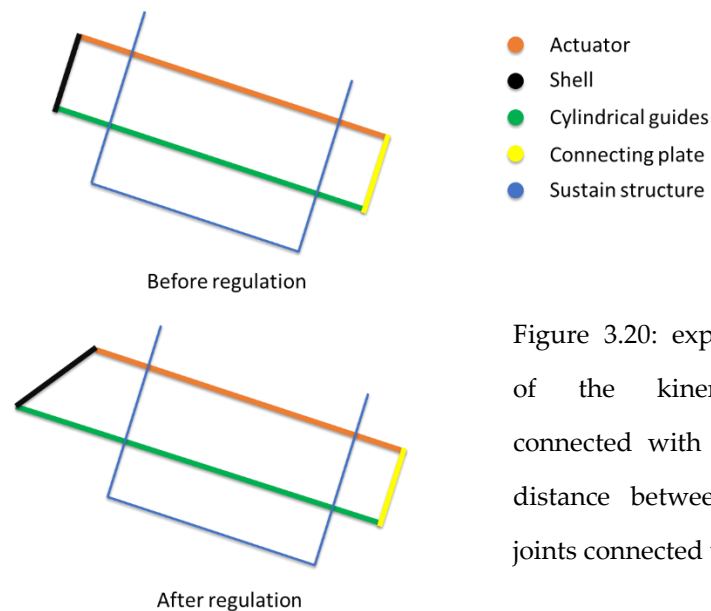


Figure 3.20: explanatory scheme of the kinematic problem connected with the fixed centre distance between the spherical joints connected with the shell.

These two main problems made it necessary to redesign the supporting structure by changing the orientation regulation system and considering a solution with a more straightforward solution of the inverse kinematics problem, which is necessary to find the corrections needed to achieve the final shell positioning.

Two possible solutions have been identified for this purpose: a first one consists in substituting the translating cart with a three dof platform, a second one is based on the use of a Stewart platform to perform the fine regulation.

4 Frontal inferior quarter's intermediate solution

This second solution partially solves the previously described problems by substituting the translating cart with a structure composed by two parallel metallic plates connected one with the other by means of three manual mechanical jacks (figure 4.1). This configuration allows to obtain a three dof parallel system whose inverse cinematic in easily solvable.

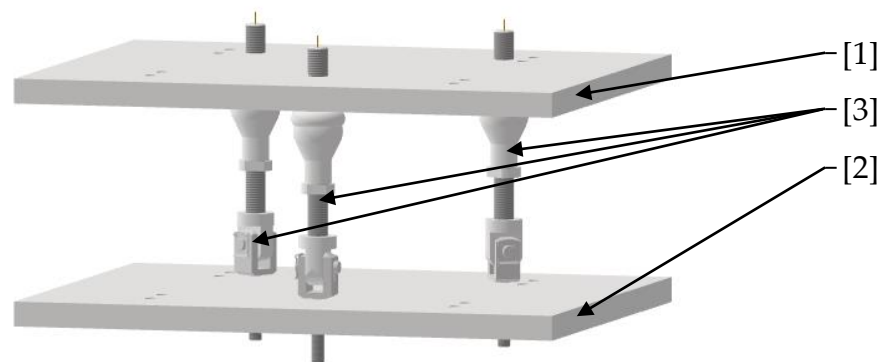


Figure 4.1: Three DOF parallel structure composed by two base plates [1] and [2] connected by three mechanical jacks [3].

4.1 Structure design

The design process is started by locally modifying the structure of solution 1 maintaining the overall functioning unchanged. Indeed, the system of linear guides has not been modified, while the cart is changed by substituting the tubular welded structure with the previously described system. The use of three mechanical jacks connected to the two parallel plates by means of a spherical joint on one end and a hinge on the other side allows to perform a fine regulation along the vertical Z axis and around the two axis Y and Z. Moreover, a system of axial bearings is mounted on the moving platform to allow the rotation around the Z axis of the automation structure (figure 4.2).

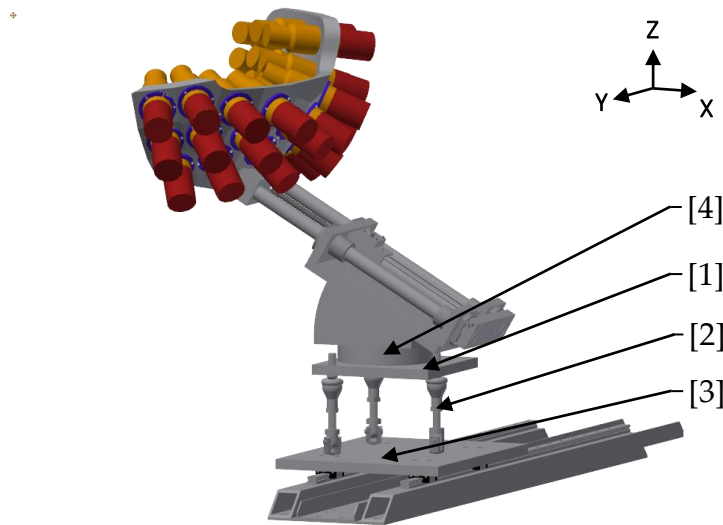


Figure 4.2: Representation of the upstream inferior quarter support structure according to solution 2 with the two parallel plates [1] and [3] connected by the mechanical jacks [2]. The whole actuation structure is mounted over the system of axial bearings [4].

The regulation along Y axis is entrusted to the linear guides as happens in the solution 1, while the regulation along axis X is performed by limiting the pneumatic actuator stroke using a threaded mechanical stopper.

Since the actuator is tilted by 40° with respect to the horizontal direction, a mutual regulation of the actuator stroke and of the 3 dof platform height is necessary to obtain a final displacement along the X axis only.

Since the regulation of the azimuthal and zenithal directions has been moved from the automation structure to the three dof platform, the system of cylindrical guides of the first solution can be simplified by moving the two guides near the actuator's rod (figure 4.3). Indeed, it is no longer required to have a triangle configuration of the guides and the actuator.

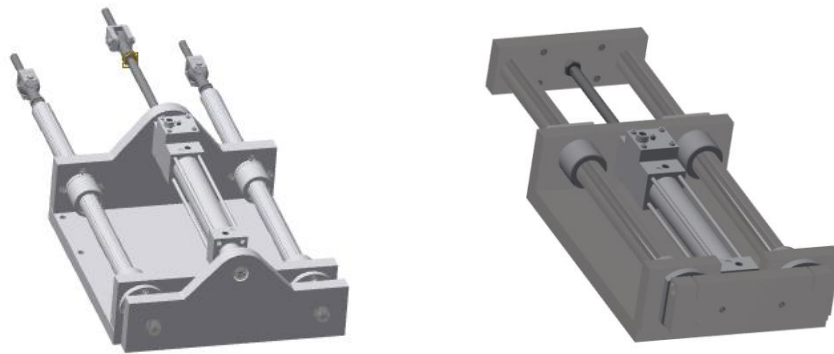


Figure 4.3: Comparison between the actuation structure of solution 1 on the left and the actuation structure of solution 2 on the right.

With this configuration the connection between the automation structure and the shell can be entrusted to a positioning plate which has a proper counterpart on the shell and, thanks to two precision's pins, the connection between the two components earns a high level of repeatability (figure 4.4). For this purpose, the shell has been properly modified to accommodate the connecting plate.

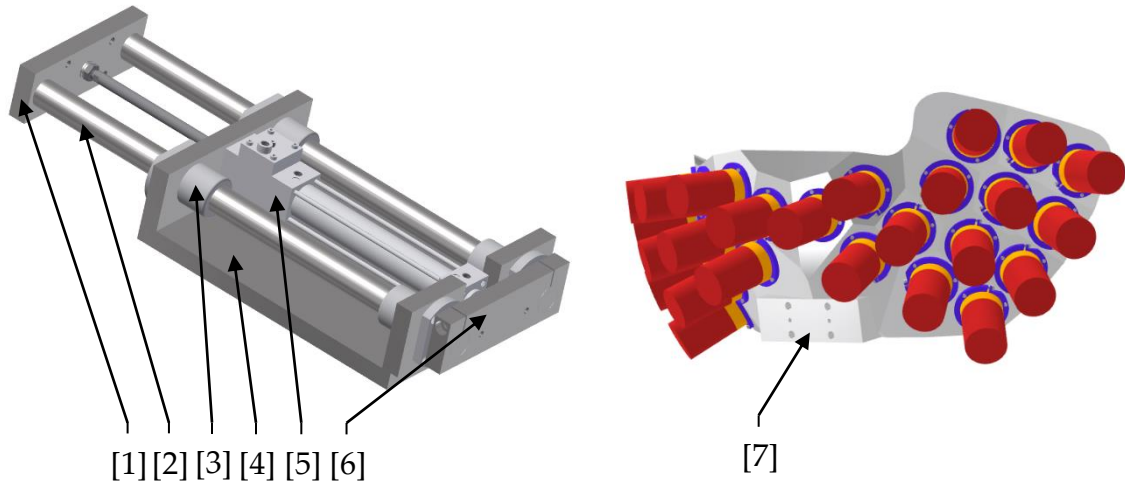


Figure 4.4: On the left: actuation structure according to solution 2 with the positioning plate [1], the cylindrical guides [2], the linear bearings [3], the supporting frame [4], the pneumatic actuator [5] and the connecting plate [6].

On the right: the modified shell which allows the easy connection with the actuation structure thanks to the rectangular plane [7] obtained on the external surface.

4.2 Global consideration on solution 2

Even if this configuration seems to solve all the main issues of solution 1, it is not the best solution for this problem. Indeed, the inverse kinematic of this system is not as simple as it seems since the three dof platform is not the unique regulator component which compose the whole structure. The bearing in charge of rotate the shell around the vertical axis and the dependence of the X axis regulation from the vertical displacement drastically complicate the solution of the inverse kinematics leading to a very complex regulation process. However, most of the changes which have been made will be maintained in the third solution since it represents an evolution of this second one.

5 Frontal inferior quarter's final structure

The critical issues encountered in the two previously described solutions have been totally solved in the design of a third structure. The idea behind this last configuration is to entrust the role of fine regulation to a single component, so that the inverse kinematic is easily solvable. In this regard, the Stewart platform represents the most well-known system which can perform this type of task ¹⁴. Use a six DOF parallel robot in between the translating cart and the automation structure allows to treat the fixed and the movable part as two independent entities whose reciprocal position is defined by the Stewart platform itself.

5.1 The Stewart's platform

Was the Englishman Eric Gough in 1954 the first man to design and study a six degree of freedom parallel robot based on the length variation of six independent mechanical jacks. Only in 1965, the platform's design was made public in a document by D. Stewart concerning a flight simulator structure ¹⁵. Even if the "Stewart platform" title is now used for this type of parallel robot, it would be more appropriate to call it as "Gough-Stewart platform" in honor of its inventor.

In his book *"Parallel Robots"* ¹⁶, J. P. Merlet gives a definition of parallel manipulator, defining it as a "closed-loop kinematic chain mechanism whose end effector is linked to the base by several independent kinematic chains".

¹⁴ P. Cruz, R. Ferreira, J. Silva Sequeira, *"Kinematic modeling of Stewart-Gough platform"*, ICINCO, 2005.

¹⁵ D. Stewart, *"A platform with six degrees of freedom"*, *Proc. Instn. Mech. Engrs.*, 1965.

¹⁶ J. Merlet, *"Parallel Robots"*, Springer Netherlands, Dordrecht, The Netherlands, 2006

Each kinematic chain, which is composed by multiple links and actuators, gives to the global robot one degree of freedom. A parallel robot can have up to six DOF which corresponds to the maximum number of DOF a body can have if free suspended.

A Gough-Stewart platform is a six degrees of freedom parallel robot which use six actuators [1] attached on one side to a fixed base plate [2] and on the other side to a moving top plate [3] by means of twelve universal joints [4] (figure 5.1). Acting on the length of each actuator it is possible to move the top plate in the three possible linear directions (T_x, T_y, T_z) and rotate it around the three main coordinate axes (R_x, R_y, R_z). Since the length variation of each leg change the position of the top platform, a synergic combination of length variations is necessary to reach a certain position of the moving plate in the space.

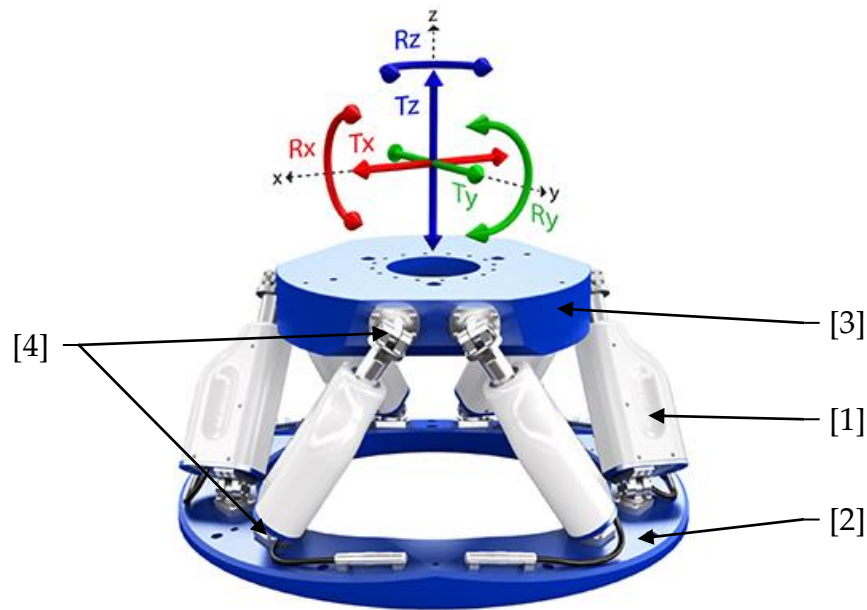


Figure 5.1: Symétrie fully automatic Stewart platform of the BREVA series ¹⁷.

[1] actuators, [2] fixed base plate, [3] moving top plate, [4] universal joints

¹⁷ BREVA, symetrie.fr, <https://symetrie.fr/hexapodes/breva/>

5.1.1 Geometry and inverse kinematic

As a parallel robot, the Gough-Stewart platform inverse kinematic is uniquely determined. This means that, knowing the final position of the moving platform, it is possible to compute the exact length of each of the six actuators which globally return that desired position. On the contrary, the direct kinematic is not unique in this type of systems and an iterative method must be implemented to find the final orientation of the top plate starting from the known legs' length.

Since in the NUMEN experiment the mutual position of the detectors' shell with respect to the target will be a known information, and the position's corrections will be based on that measurement, an inverse kinematic model will characterize the study of the system drastically simplifying the solution of the problem.

The main idea behind the inverse kinematic of a parallel robot is to consider a change of coordinates. Considering the fixed plate to have coordinate system B while the top moving plate having coordinate system P , it is possible to express the universal joints centers mounted on the base frame referenced in the coordinate system B and the top universal joints centers referenced in the local coordinate system P (figure 5.2).

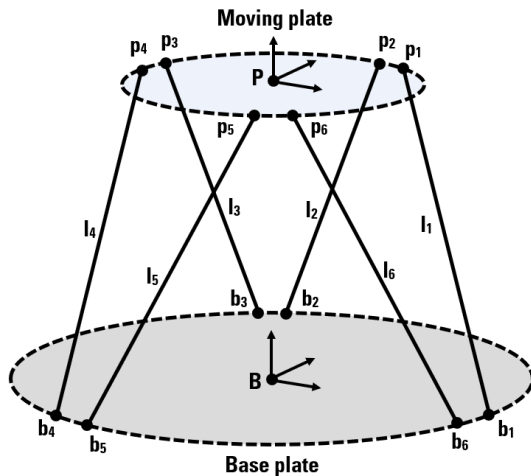


Figure 5.2: Simplified scheme of a Stewart platform with represented both B and P reference frames, the base universal joints centre b_i , the moving universal joints centre p_i , and the six actuators l_i .

As the top platform moves, the coordinate of the moving universal joints center never change according to their coordinate system P, but they move with respect to the fixed base frame B. It is then necessary to find a mathematical relationship between the coordinates expressed in the moving reference frame P and the fixed reference system B to solve the inverse kinematic of the Stewart platform.

This procedure starts from the definition of the geometry of the base plate and the top plate expressing the coordinates of the universal joints in their respective reference frame. Several configurations can be adopted in the definition of the geometry (figure 5.3):

- 3-3 type: the top and the base plates are composed by two equilateral triangles tilted by 60° with respect to the vertical axis. The joints belonging to the same plate are spaced by a 120° angle.
- 3-6 type: the top plate has a triangular shape, while the base is composed by a hexagon. The top plate's joints are spaced by a 120° angle, while the bases' ones are spaced by 60° .
- 6-6 type: both the top and the base plates have a hexagon shape. The joints belonging to the same plate are spaced by a 60° angle.

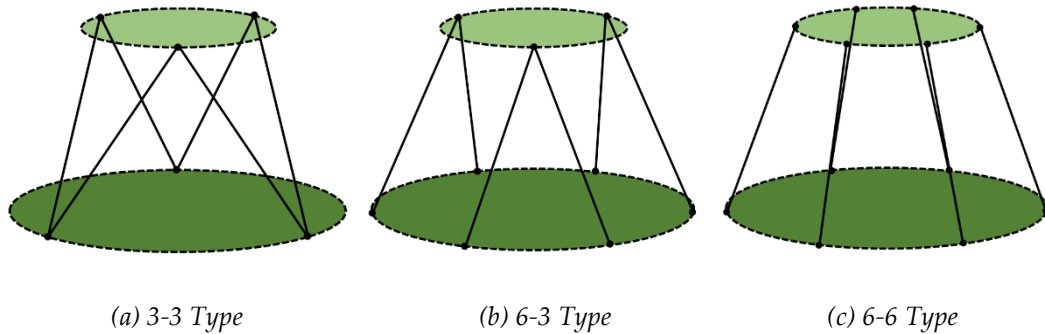


Figure 5.3: Different Stewart platform geometry configurations.

Even if the 6-6 configuration is theoretically possible, it is never used in practice since it has been demonstrated that this configuration suffers an instability problem (figure 5.4). Indeed, if the joints of both the plates are spaced by a 60° angle and each actuator does not share the joint with another one, the structure is not able to counter the rotation of the top platform around the vertical axis resulting in a global collapse of the system.

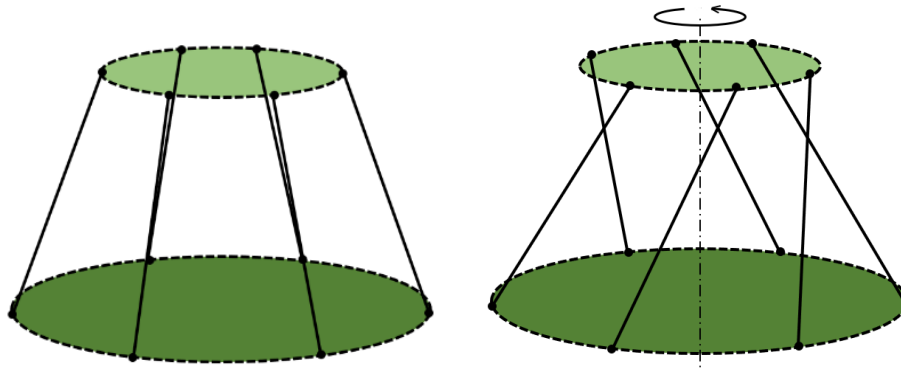


Figure 5.4: Schematic representation of a 6-6 type Stewart platform showing the instability problem described above.

To solve this problem and to give high stability to the entire structure a mixed design between the 3-3 and the 6-6 configurations is usually used (figure 5.5). It consists in add a small gap between the universal joints sharing the same position in a 3-3 type platform. The resulting geometry has the stability of a 3-3 platform, but the small gap between the joints solves the problem of overlap of the universal joints sharing the same position.

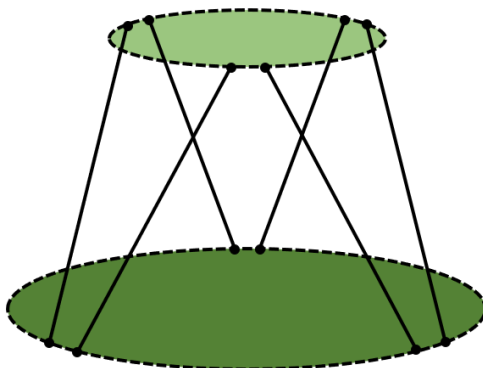


Figure 5.5: Schematic representation of a typical Stewart platform configuration.

Once the global geometry is identified, it is necessary to define the coordinates of each universal joints with their respective reference frame.

Assuming the joints connected with the fixed base lying on a circumference having radius “R” centered in the origin “O” of the fixed reference frame B and the ones connected with the moving base lying on a circumference having radius “r” centered in the origin “o” of the moving reference frame P, the coordinates of the universal joints are expressed as:

$$B1 = (R \cos(60 - \gamma) ; R \sin(60 - \gamma) ; 0)$$

$$B2 = (R \cos(60 + \gamma) ; R \sin(60 + \gamma) ; 0)$$

$$B3 = (-R \cos(\gamma) ; R \sin(\gamma) ; 0)$$

$$B4 = (-R \cos(\gamma) ; -R \sin(\gamma) ; 0)$$

$$B5 = (R \cos(60 + \gamma) ; -R \sin(60 + \gamma) ; 0)$$

$$B6 = (R \cos(60 - \gamma) ; -R \sin(60 - \gamma) ; 0)$$

for the universal joints connected to the fixed base, and:

$$P1 = (r \cos(\gamma) ; r \sin(\gamma) ; 0)$$

$$P2 = (-r \sin(30 - \gamma) ; r \cos(30 - \gamma) ; 0)$$

$$P3 = (-r \sin(30 + \gamma) ; r \cos(30 + \gamma) ; 0)$$

$$P4 = (-r \sin(30 + \gamma) ; -r \cos(30 + \gamma) ; 0)$$

$$P5 = (-r \sin(30 - \gamma) ; -r \cos(30 - \gamma) ; 0)$$

$$P6 = (r \cos(\gamma) ; -r \sin(\gamma) ; 0)$$

for the universal joints connected with the moving base (figure 5.6).

These relationships are obtained by considering a 3-3 configuration and by adding and subtracting a constant γ angle from the 60° that characterize the 3-3 types.

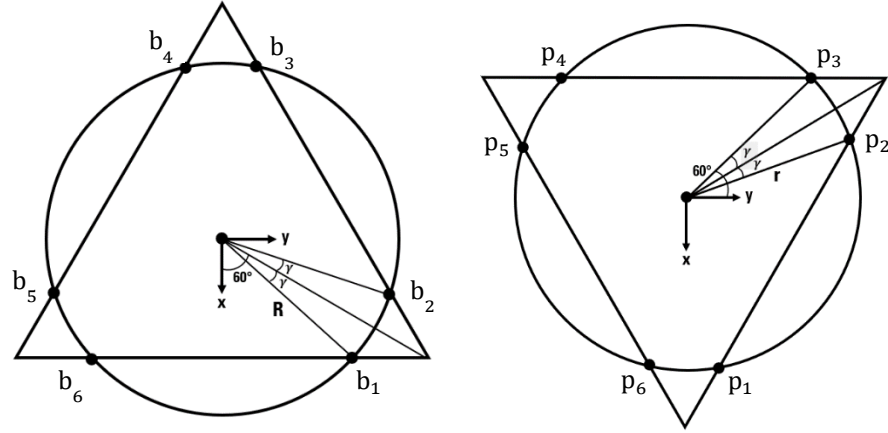


Figure 5.6: Top view of the base plate on the left and the moving plate on the right with their respective coordinate systems and the points of connection for the universal joints.

Knowing the position of the twelve joints and the two reference systems' centers allows to compose each kinematic chain that, once solved, lead to the solution of the global inverse kinematic problem.

For the Stewart platform the inverse kinematic problem consists in the solution of six kinematic chains each of which is characterized by four vectors: \bar{R} connects the origin "O" of the fixed reference frame and one generic base spherical joint ($b_1, b_2, b_3, b_4, b_5, b_6$), \bar{r} connects the origin "o" of the moving reference frame and one generic moving spherical joint ($p_1, p_2, p_3, p_4, p_5, p_6$), \bar{l} connects two spherical joints, \bar{h} connects the two centers of the reference frames "B" and "P" (figure 5.7).

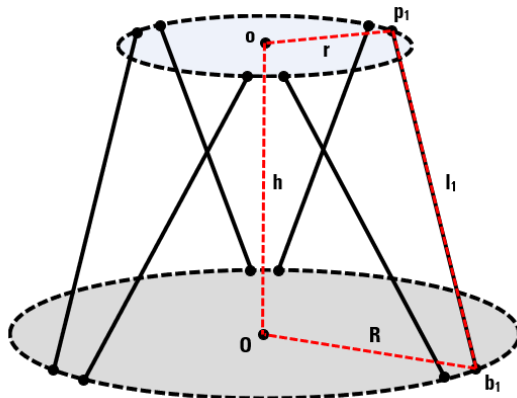


Figure 5.7: In red the kinematic chain connected to leg 1.

To solve the kinematic chains, it is necessary to express the coordinate of p1, p2, p3, p4, p5, p6 and "o" with respect to the fixed reference frame to have all the points of the chain belonging to the same reference system. It is then required to know the position of the center "o" with respect to "O" and the rotation of the reference frame "P" with respect to the fixed frame "B". Since the position of center "o" will be an input of the inverse kinematic and it is not affected by the rotation of the reference frame "P", it is possible to express it as ${}^{O_B}o = [X, Y, Z]$.

The process to obtain the coordinate of the six movable universal joints in the fixed reference frame is much more complicated since they do not depend only on the position of the center of the reference system, but they depend also on the rotation of the moving reference system with respect to the fixed one. The concept of rotation matrix must, therefore, be introduced.

The rotation of a vector around one of the three axis of a reference frame is called "basic" or "elemental" rotation and can be performed multiplying the vector by one of the three possible rotation matrices. These matrices are obtained by projecting the rotated vector on the axis of the system of coordinate and are here reported:

$$R(x, \psi) = \begin{bmatrix} 1 & 0 & 0 \\ 0 & \cos \psi & -\sin \psi \\ 0 & \sin \psi & \cos \psi \end{bmatrix}$$

$$R(y, \theta) = \begin{bmatrix} \cos \theta & 0 & \sin \theta \\ 0 & 1 & 0 \\ -\sin \theta & 0 & \cos \theta \end{bmatrix}$$

$$R(z, \varphi) = \begin{bmatrix} \cos \varphi & -\sin \varphi & 0 \\ \sin \varphi & \cos \varphi & 0 \\ 0 & 0 & 1 \end{bmatrix}$$

where ψ is the rotation around axis X, θ is the rotation around axis Y and φ is the rotation around axis Z.

If a combined rotation must be performed, the previous matrices must be multiplied together to obtain a unique rotation matrix which considers all the possible rotations:

$$R = [R(z, \varphi)][R(y, \theta)][R(x, \psi)]$$

This multiplication can be performed firstly by multiplying the two matrices $[R(z, \varphi)][R(y, \theta)]$ obtaining:

$$\begin{bmatrix} \cos \varphi & -\sin \varphi & 0 \\ \sin \varphi & \cos \varphi & 0 \\ 0 & 0 & 1 \end{bmatrix} \begin{bmatrix} \cos \theta & 0 & \sin \theta \\ 0 & 1 & 0 \\ -\sin \theta & 0 & \cos \theta \end{bmatrix} \\ = \begin{bmatrix} \cos \varphi \cos \theta & -\sin \varphi & \cos \varphi \sin \theta \\ \sin \varphi \cos \theta & \cos \varphi & \sin \varphi \sin \theta \\ -\sin \theta & 0 & \cos \theta \end{bmatrix}$$

and subsequently by multiplying the obtained matrix by $[R(x, \psi)]$:

$$R = \begin{bmatrix} \cos \varphi \cos \theta & -\sin \varphi & \cos \varphi \sin \theta \\ \sin \varphi \cos \theta & \cos \varphi & \sin \varphi \sin \theta \\ -\sin \theta & 0 & \cos \theta \end{bmatrix} \begin{bmatrix} 1 & 0 & 0 \\ 0 & \cos \psi & -\sin \psi \\ 0 & \sin \psi & \cos \psi \end{bmatrix} \\ = \begin{bmatrix} \cos \varphi \cos \theta & \cos \varphi \sin \theta \sin \psi - \sin \varphi \cos \psi & \sin \varphi \sin \psi + \cos \varphi \sin \theta \cos \psi \\ \sin \varphi \cos \theta & \cos \varphi \cos \psi + \sin \varphi \sin \theta \sin \psi & \sin \varphi \sin \theta \cos \psi - \cos \varphi \sin \psi \\ -\sin \theta & \cos \theta \sin \psi & \cos \theta \cos \psi \end{bmatrix}$$

The rotation matrix R here obtained allows to rotate the \vec{r} vector initially belonging to the moving reference frame knowing the three angles of rotation φ, θ and ψ which will be inputs of the inverse kinematic problem. Rotating the \vec{r} vector

is necessary to express it in the fixed reference frame, so that it is possible to solve the connected kinematic chain. To perform the rotation, it is sufficient to multiply the vector \bar{r} by the rotation matrix R obtaining a new vector \bar{r}_B expressed in the fixed reference system:

$$\begin{bmatrix} r_x \\ r_y \\ r_z \end{bmatrix}_B = \begin{bmatrix} \cos \varphi \cos \theta & \cos \varphi \sin \theta \sin \psi - \sin \varphi \cos \psi & \sin \varphi \sin \psi + \cos \varphi \sin \theta \cos \psi \\ \sin \varphi \cos \theta & \cos \varphi \cos \psi + \sin \varphi \sin \theta \sin \psi & \sin \varphi \sin \theta \cos \psi - \cos \varphi \sin \psi \\ -\sin \theta & \cos \theta \sin \psi & \cos \theta \cos \psi \end{bmatrix} \begin{bmatrix} r_x \\ r_y \\ r_z \end{bmatrix}_P$$

$[r]_P$ is known from the imposed geometry and the three angles of rotation are inputs of the problem, therefore the equation can be solved.

It is now possible to set up the vectorial equations which, once solved, lead to the computation of the length of the six Stewart platform's legs:

$$\bar{l}_i = \bar{h}_i + \bar{r}_i - \bar{R}_i$$

or expanding the vector equation:

$$\begin{bmatrix} l_{ix} \\ l_{iy} \\ l_{iz} \end{bmatrix}_B = \begin{bmatrix} h_{ix} \\ h_{iy} \\ h_{iz} \end{bmatrix}_B + \begin{bmatrix} r_{ix} \\ r_{iy} \\ r_{iz} \end{bmatrix}_B - \begin{bmatrix} R_{ix} \\ R_{iy} \\ R_{iz} \end{bmatrix}_B$$

for $i = 1 \div 6$.

Once the six vectorial equations have been solved, the length of each actuator can be computed by performing the Euclidean norm of the corresponding vector:

$$\|l_i\| = \sqrt{(l_{ix})^2 + (l_{iy})^2 + (l_{iz})^2}$$

for $i = 1 \div 6$.

The inverse kinematic problem is then solved since, starting from the known position and orientation of the moving top plate, the length of each leg can be computed and imposed to the physical system.

The computation of the inverse kinematic of the Stewart platform used in this thesis has been implemented using Matlab. A proper script is coded to solve the problem and to return the legs length given the position and the orientation of the moving plate. The script also considers the structure above the Stewart platform which act as a lever when the orientation of the moving base is changed. Indeed, a small movement in correspondence of the center “o” generate a big movement of the center of the shell. Then, a proper algorithm based on a trial-and-error method is developed to convert the known shell displacement correction into the Stewart platform orientation correction.

5.1.2 Global geometry

It is now necessary to find a mathematical relationship between the movements of the top plate of the Stewart platform and the corresponding movements of the center of the detectors’ shell.

First, it is necessary to create a geometrical model of the global structure with some characteristic dimensions imposed by the CAD model (figure 5.8). Thanks to the already developed geometry of the first two design attempts, it has

been possible to create a geometrical model which allows the entire structure to enter in the small area in front of the scattering chamber and to pass behind the high intensity line when translated.

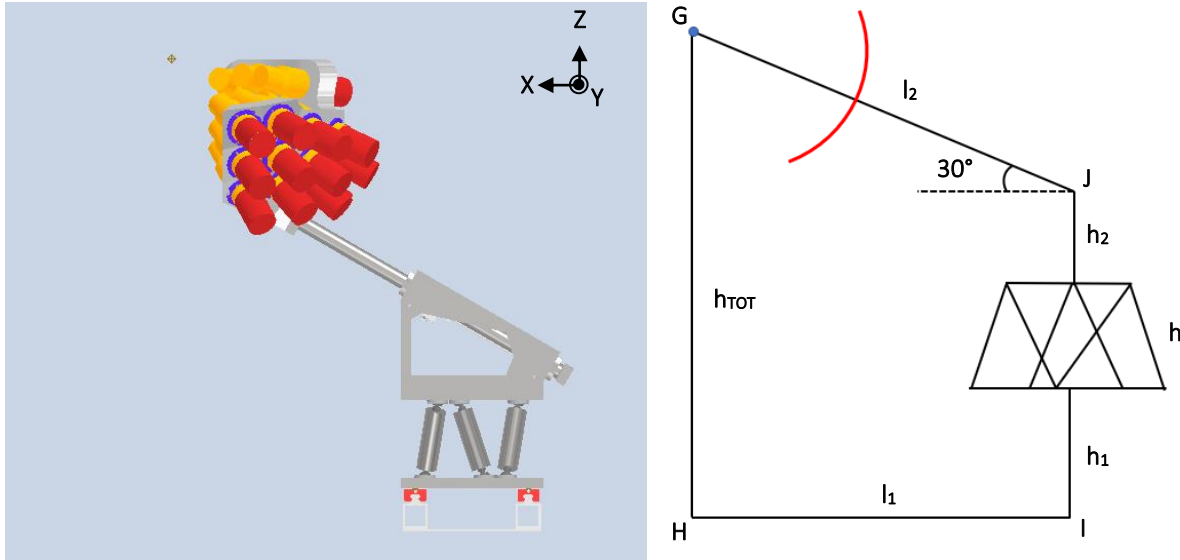
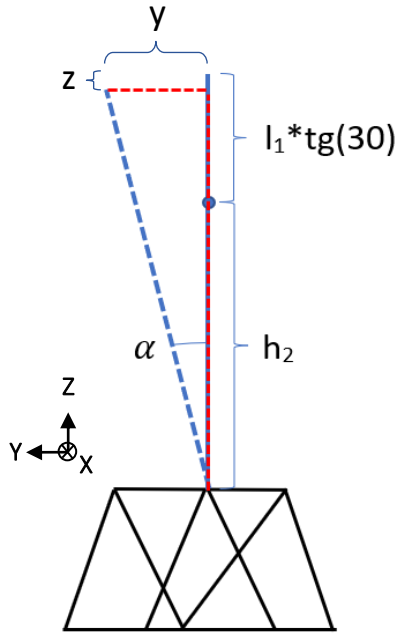


Figure 5.8: On the left the lateral view of the upstream inferior quarter support structure according to solution 3. On the right a schematic representation of the structure which allows to simplify the geometrical understanding of the system.

From the above drawing it is easy to understand that a movement along the X, Y and Z directions of the Stewart platform's moving plate corresponds to an equal movement of the center of the shell. Instead, the rotation of the moving plate in the space produces a roto-translation of the end effector making it necessary to compensate the not desired movement along the three principal axis.

Considering one rotation at time, it is possible to find a relation between the rotation of the Stewart platform and the translation of the end effector:

Rotation in X direction:



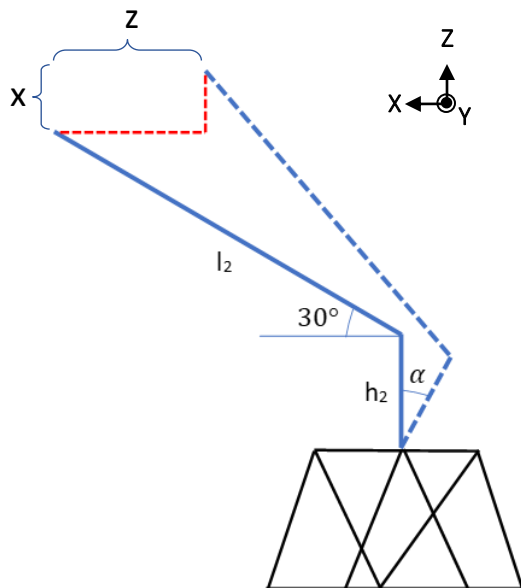
$$(l_1 \operatorname{tg}(30) + h_2) \sin \alpha + y = 0$$

$$y = -(l_1 \operatorname{tg}(30) + h_2) \sin \alpha$$

$$(l_1 \operatorname{tg}(30) + h_2) \cos \alpha + z = l_1 \operatorname{tg}(30) + h_2$$

$$z = l_1 \operatorname{tg}(30) + h_2 - (l_1 \operatorname{tg}(30) + h_2) \cos \alpha$$

Rotation in Y direction:



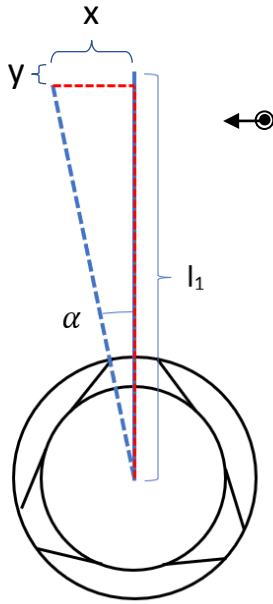
$$h_2 \sin \alpha - l_2 \cos(\alpha + 30) + x = -l_2 \cos(30)$$

$$x = l_2(\cos(\alpha + \gamma) - \cos \gamma) - h_2 \sin \alpha$$

$$h_2 \cos \alpha + l_2 \sin(\alpha + 30) + y = h_2 + l_2 \sin(30)$$

$$y = h_2(1 - \cos \alpha) + l_2(\sin(30) - \sin(\alpha + 30))$$

Rotation in Z direction:



$$l_1 \cos(\alpha) + x = l_1$$

$$x = l_1(1 - \cos\alpha)$$

$$l_1 \sin\alpha + y = 0$$

$$y = -l_1 \sin\alpha$$

These relations are implemented in the Matlab environment to correct the translation of the shell when the Stewart platform is tilted, and it came out that they perform well only when a single rotation of the moving plate is considered. Indeed, if a multiple rotation around different axis is made, the geometrical relations previously obtained decay, and a combination of them does not allow to obtain the required result. It is then necessary to find another method to compensate the translation of the shell.

Thanks to some tests performed with the Matlab model, a practical method to solve the problem of translation compensation due to multiple rotations has been identified.

The procedure consists of three steps:

- The multiple rotations are imposed to the system without performing any displacement compensation.

- Using the software, the new position of the end effector is obtained and the distance between the center of the shell and the target is computed. This distance must then be projected along the three main axis X, Y and Z to obtain the required displacement corrections which allows the two centers to align one with the other.
- The obtained corrections are then inserted in the script and the code is run again. Since the corrections are applied only as translations and not as rotations, the result is an overlap of both the centers of the shell and the target with a rotation of the detectors with respect to the scattering chamber.

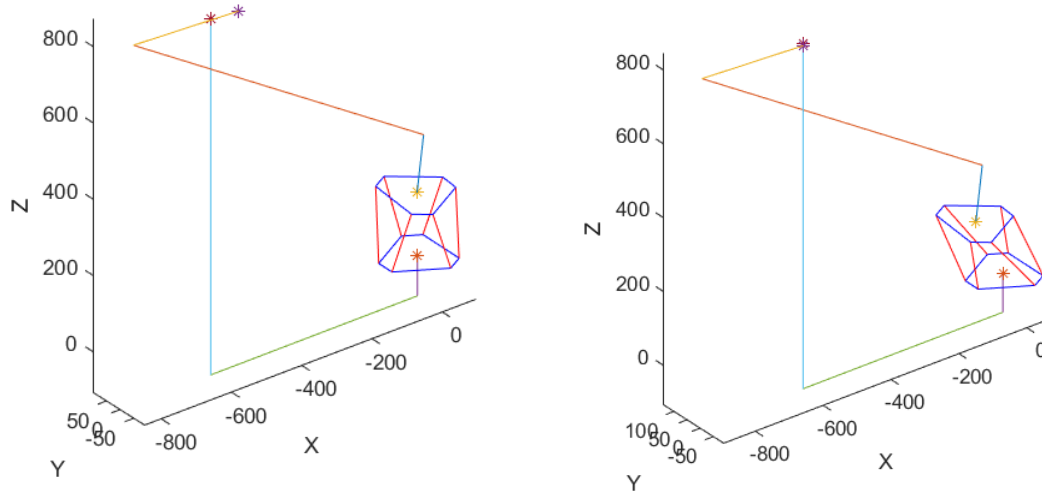


Figure 5.9: On the left the MATLAB model of the system with an imposed rotation of the shell. It is possible to notice that the centre of the shell (blue star) and the centre of the scattering chamber (red star) are not aligned even if any translation of the shell is imposed to the system.

On the right the Stewart platform correction which allows to obtain a final rotation of the shell with respect to the scattering chamber leaving the two centres aligned.

This method allows to compensate any translation caused by the rotations of the shell without affecting the rotations themselves. It is then possible to compute the length of the six legs of the Stewart platform given any translation or rotation of the end effector with respect to the fixed base.

The inverse kinematic problem of the entire system is then solved, and the physical model can be designed.

5.1.3 Commercial Stewart platform

Several hexapod robots are already available on the market and some of them satisfy most of the requirements needed for the construction of the structure treated in this thesis. The use of an already existing Stewart platform will simplify the design phase and will avoid several tests needed to calibrate the structure. However, the use of a fully automated robot will drastically increase the costs as demonstrate some quotes done by mechanical companies.

As an example, a quote from a well-known manufacturer is here reported:

- Compact hexapod microrobot, brushless DC gear motor, absolute encoder, 30 kg load capacity, 2.5 mm/s velocity: 26637,30 €
- Data transmission cable for hexapods, drag chain compatible, 3m: 318,60€
- Power supply cable for hexapod, drag chain compatible, 3 m: 41,40 €
- Six-axis controller for hexapod: 4500 €

The total cost for the Stewart platform amounted to 31497,30 € which must be then added to the cost of all the other components needed to realize the support structure. The so high price is mainly due to the high precision actuators used in the hexapod and to the electronic required to control them. A cheaper solution can then be obtained by substituting the fully automated structure with a manual one which use precision mechanical jacks instead of the electric actuators.

5.1.4 Manual Stewart platform design

The main problem of a fully manually operated Stewart platform is the impossibility to modify simultaneously the length of the six legs. This led to a direct kinematic problem since the intermediate positions that the moving plate acquired during the calibration of the legs' length is not determined a priori until all the six regulations have been performed. It is then necessary to have an estimation of the positions that the moving plate will occupy during the calibration to prevent any collisions of the shell with the scattering chamber during the intermediate phases. As noticed in the previous chapters, the direct kinematic problem of a parallel robot is difficult to be solved since its solution is not unique. Some mathematical algorithms are available in literature to solve the direct kinematic of a parallel robot, but they all require a high computational cost, and they usually return only an estimation of the position assumed by the moving plate. A possible solution to avoid the collision with the surrounding components is to divide the procedure of length variation required by each leg into steps. In this way, the uncontrolled movement of the Stewart platform upper plate is divided into sub-movements which allows the operator to better control the regulation process. Increasing the number of steps needed to reach the final configuration will lead to a regulation similar to the one performed by the fully automated Stewart platform, reducing the risk of collisions, and obtaining a controlled movement.

5.2 Design and sizing of the elements of the supporting structure

Once the Stewart platform has been studied and the inverse kinematic has been generally solved, it is necessary to design the physical model in the CAD environment. The global geometry of the entire support is described in the previous chapters based on the dimensions obtained from the firsts two solutions.

Then, all the components must be properly sized both in dimensions and in strength to comply with the available space and the mechanical requirements.

Each component is designed in Inventor and it is subsequently analyzed thanks to a FEM analysis in order to understand the theoretical behavior of the component when subjected to all the forces acting on it. The FEM analysis returned the value of the Von Mises stresses, the safety factor based on the mechanical properties of the material, and the deformation of the analyzed component in the three main directions X, Y and Z.

For the sizing of the connection bolts, it is necessary to mathematically compute the axial and the tangential forces acting on the stem and subsequently enters the data obtained in the relative Inventor's tool which, giving the entity of the known forces and the number of bolts used in the threaded connection, return the minimum dimensions of the bolts.

5.2.1 Upstream inferior quarter shell

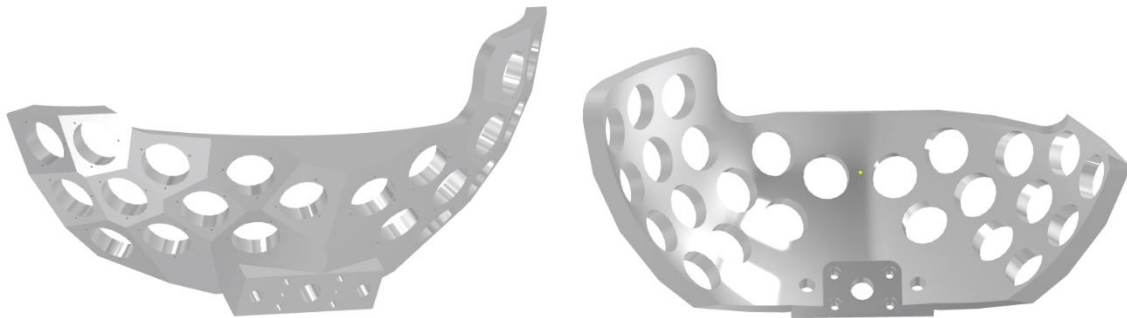


Figure 5.10: Frontal and rear view of the upstream inferior quarter shell.

It is the element entrusted to support all the 25 detectors in the working position. It is made by Anticorodal aluminum (6000 series) which is selected from the three possible materials mentioned in chapter 3.4: Anticorodal, Ergal and AISI 304. Indeed, it is the easiest to be machined, and, since the shape of the shell is

very complex, the easier the machining process, the cheaper the total cost of the shell.

The faceted geometry of the shell has been obtained by considering the ideal position of the detectors coming from physical simulations and by removing material from the solid metal so that all the detectors could be accommodated in their hosting holes all pointing towards the center of the scattering chamber. Each flat surface is perpendicular to the related hole, and it is used to screw the detector's collar in place blocking the detector in the right position (the internal face of the detectors is positioned 240 mm from the target).

To connect the shell with the automation structure, a proper connecting plate has been designed (figure 5.11). It is tilted by 30° with respect to the horizontal line to be perpendicular to the actuator's direction described later. The position of the tilted plane on which the connecting plate is located has been identified considering the following geometries:

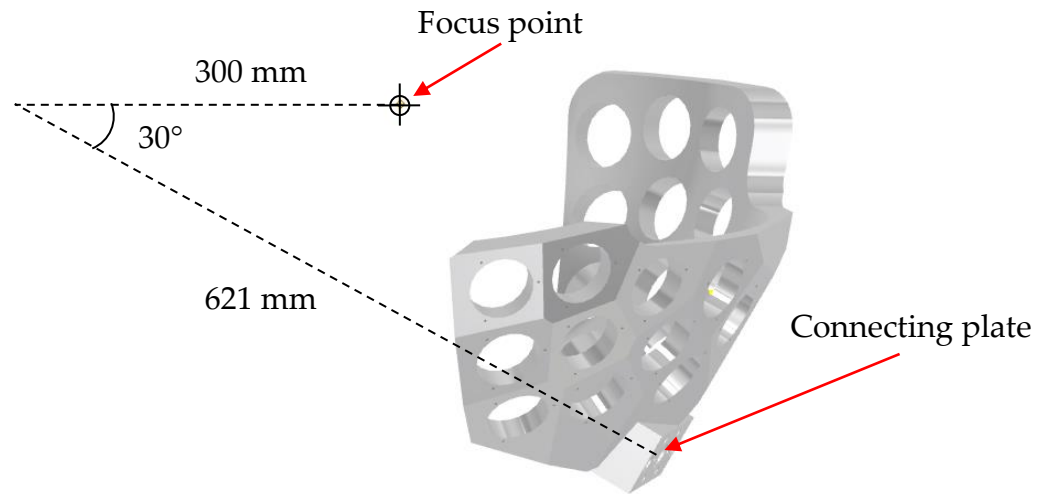


Figure 5.11: Lateral view of the upstream inferior quarter shell with the positioning dimensions of the connecting plate with respect to the focus point of the shell.

These dimensions are obtained considering the global geometry of the structure and will be taken into account for the sizing of the components connected with the shell.

In the internal part of the shell some material has been removed in correspondence of the connecting plate to lighten the structure, but a minimum thickness equal to 30 mm has been guaranteed not to weaken the strength of the shell (figure 5.12).

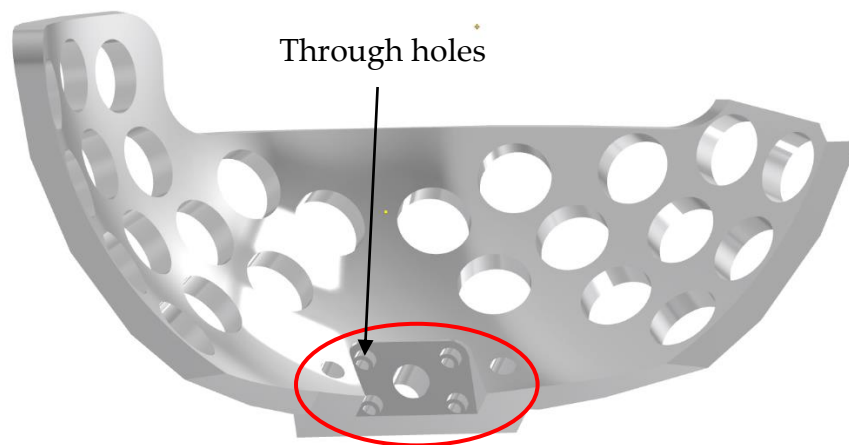


Figure 5.12: Frontal view of the upstream inferior quarter shell with the internal connecting zone highlighted in red.

The connection between the shell and the automation structure is entrusted to a system of four M10x1,5 bolts which could be inserted from the inside of the shell thanks to four through holes (figure 5.12). The sizes of these bolts will be confirmed in the following dedicated chapter.

Two $\phi 6$ pins located on the external surface of the shell ensure the correct positioning of the shell guaranteeing a high level of repeatability to the connection (figure 5.13).

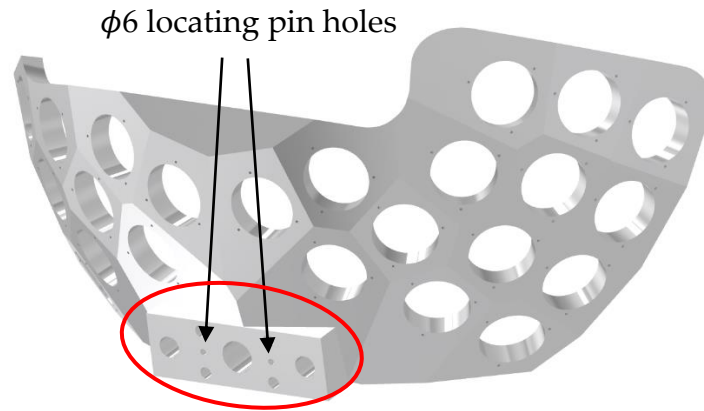
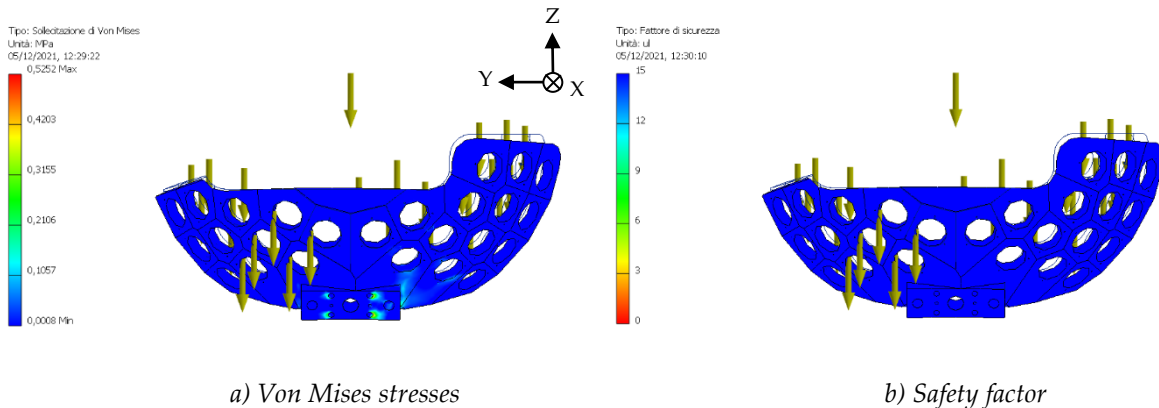
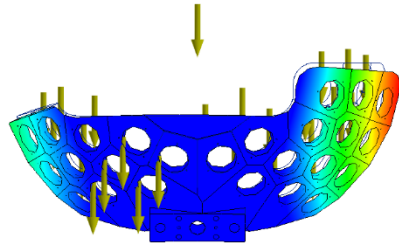


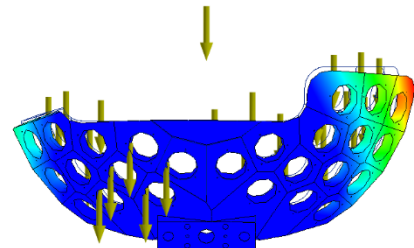
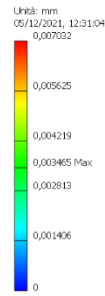
Figure 5.13: Rear view of the upstream inferior quarter shell with the external connecting zone highlighted in red.

To ensure a correct performance of the shell, the CAD model is mechanically tested by performing a FEM analysis. The anticorodal aluminum shell is considered constrained in correspondence of the connecting plate using as constraints the four bolt's holes. Then a 7 N vertical forces is imposed to each of the 25 radial holes simulating the weight of the detectors (0,7 kg each). Moreover, the gravitational force is added to the simulation to consider the weight of the shell itself (around 26 kg). Here are reported the main results of the analysis:

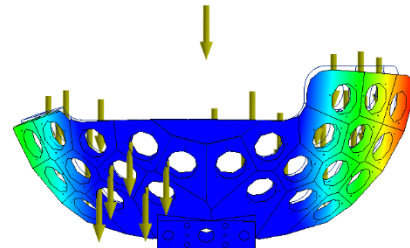
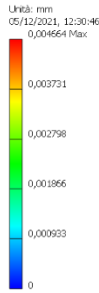




c) X displacement



d) Y displacement



e) Z displacement

From the above results it is possible to notice that the shell is sufficiently strong to sustain all the 25 detectors without being subjected to excessive stresses. The safety factor is higher than 15 in the whole component and the Von Mises stresses are much lower than the $R_{p0,2}$ of the aluminum equal to 250 MPa. The so high safety factor, which will also characterize all the other components described below, is justified by the fact that the main purpose of the structure is to reach a high positioning precision. All the structure's components are then oversized with respect to the optimized ones in order to reduce all the possible flexural deformations. This lead to a maximum deformation of the shell in the three main directions strictly below the admissible displacement of the entire structure and it is mainly concentrated on the top right of the shell affecting the positioning of only few detectors.

5.2.2 Shell's connecting bolts

The size of the four M10x1,5 bolts chosen to connect the shell with the automation structure is confirmed by computing the axial forces acting on their stems and by inserting the computed values into the dedicated Inventor's tool.

To compute the forces, it is previously required to know the position of the barycenter of the shell with respect to the center of the connecting plate. Indeed, since the computation will be performed in static condition, all the weight of the shell is considered concentrated in the barycenter, and its position influences the entity of the momentums acting on the connection.

The identification of the shell's barycenter is possible thanks to the dedicated Inventor's tools which compute its position starting from the geometries and the materials of the analyzed component (figure 5.14).



Figure 5.14: Frontal and lateral view of the upstream inferior quarter with indicated the position of the barycentre which is computed considering both the weight of the shell and the weight of the 25 detectors.

As can be seen from figure 5.14, the concentrated weight force is translated with respect to the connecting plate. This generate some moments on the connection which are converted into axial forces acting on the bolts. Since the connecting plate is tilted by a 30° angle, the weight force F can be decomposed into two perpendicular components: $F_{\parallel} = F * \sin(30)$ aligned to the direction of the

actuator (perpendicular to the connecting plate) and $F_{\perp} = F * \cos(30)$ perpendicular to the actuator's direction (figure 5.15).

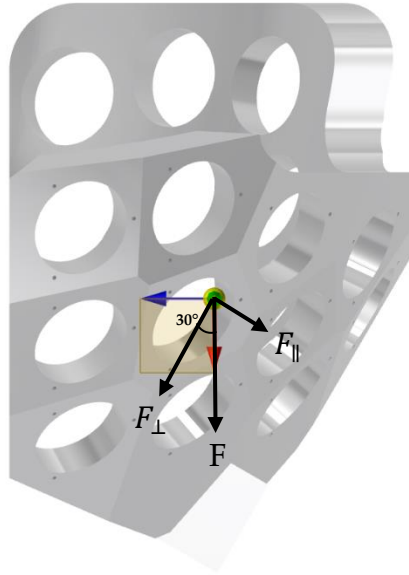


Figure 5.15: Lateral view of the upstream inferior quarter. The concentrated weight force is positioned in the barycentre pointing downwards in Z direction and it is decomposed into the two vectors F_{\parallel} and F_{\perp} described above.

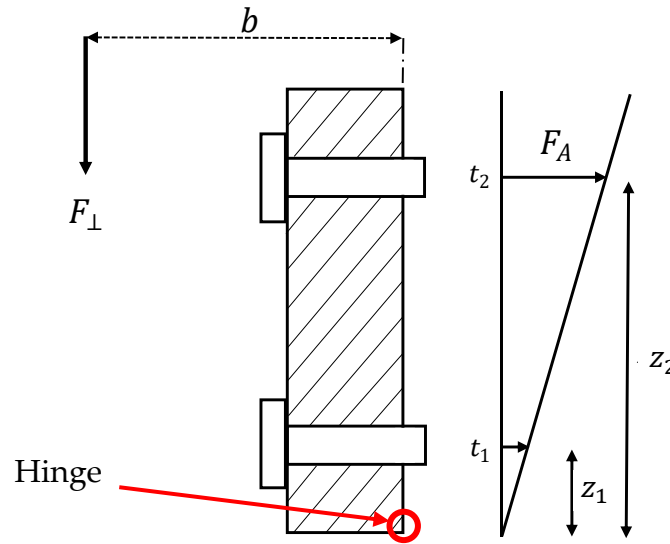
Data:

- $F = 25,659 \text{ kg} * g = 251,71 \text{ N}$
- $F_{\parallel} = 251,71 * \sin(30) = 125,86 \text{ N}$
- $F_{\perp} = 251,71 * \cos(30) = 217,99 \text{ N}$

It is then possible to compute the resultant force acting on each bolt by considering the superposition of effects of the different forces and moments generated by the two previously computed force coming from the decomposition of the weight force in the two axial and tangential components:

1) Axial force due to moment in Y direction

The moment generated by the X displacement of F_{\perp} with respect to the center of the connection plate is converted into an axial force on the bolts thanks to the hinge effect produced by the lower edge of the plate. The entity of the axial force acting on the bolts is directly proportional to the distance of the bolts themselves from the hinge. Considering the following drawing:



the generic axial force t_i is expressed as:

$$t_i = F_A * \frac{z_i}{z_n}$$

with:

- F_A : axial force acting on the most stressed bolt
- z_i : distance of the i-th bolt from the hinge
- z_n : distance of the furthest bolt from the hinge

Since the axial force is unknown it is possible to express it as function of the known moment M_y considering the following relation:

$$M_y = 2 * \left(F_A * z_n + F_A * \frac{z_{n-1}}{z_n} + \dots + F_A * \frac{z_1}{z_n} \right)$$

from which it is possible to derive the value of the axial force F_A as:

$$F_A = \frac{M_y * z_n}{2 * (z_n^2 + z_{n-1}^2 + \dots + z_1^2)}$$

Then, since the geometry of the connecting plate and the entity of the momentum are known it is possible to compute the axial forces acting on each bolt (figure 5.16).

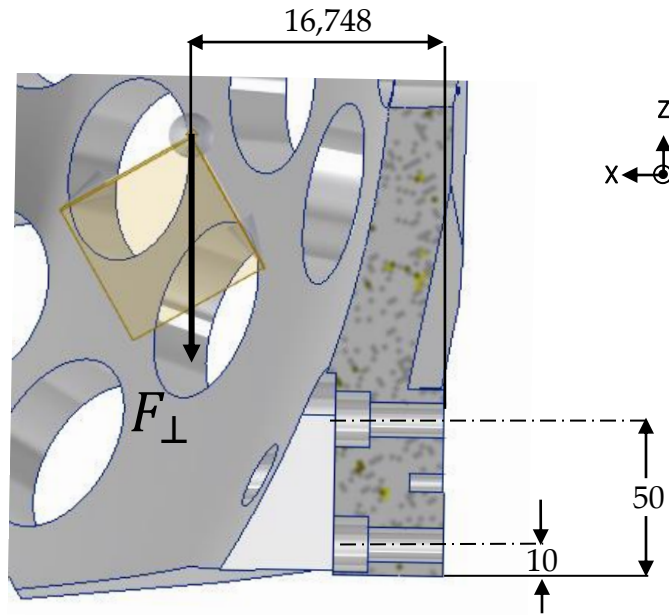


Figure 5.16: Detail of the section of the shell showing the geometry of the connecting plate.

Data:

- $F_{\perp} = F * \cos(30) = 217,99 \text{ N}$
- $b = 16,748 \text{ mm}$
- $M_y = F_{\perp} * b = 3650,90 \text{ Nmm}$
- $z_1 = 10 \text{ mm}$
- $z_2 = 50 \text{ mm}$

Computations:

$$F_A = \frac{M_y * z_2}{2 * (z_2^2 + z_1^2)} = 35,10 \text{ N}$$

$$t_1 = F_A * \frac{z_1}{z_2} = 7,02 \text{ N} \quad t_2 = F_A * \frac{z_2}{z_2} = F_A = 35,10 \text{ N}$$

2) Axial force due to moment in Z direction

Since the barycenter of the shell is displaced from the center of the connecting plate also in the Y direction, the component of the shell's weight F_{\parallel} , parallel to the direction of the actuator, generate an M_z momentum.

As happens for the M_y momentum, it is possible to compute the axial force generated by M_z on the bolts by considering the right edge of the connecting plate as a hinge and computing the axial loads as done before (figure 5.17):

$$t_i = F_A * \frac{y_i}{y_n}$$

with:

- F_A : axial force acting on the most stressed bolt
- y_i : distance of the i-th bolt from the hinge
- y_n : distance of the furthest bolt from the hinge

$$M_z = 2 * \left(F_A * y_n + F_A * \frac{y_{n-1}}{y_n} + \dots + F_A * \frac{y_1}{y_n} \right)$$

$$F_A = \frac{M_z * y_n}{2 * (y_n^2 + y_{n-1}^2 + \dots + y_1^2)}$$

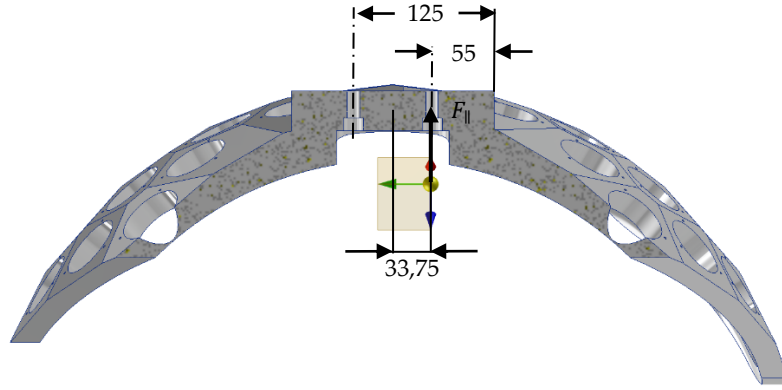


Figure 5.17: Section of the shell showing the geometry of the connecting plate.

Data:

- $F_{\parallel} = F * \sin(30) = 125,86 \text{ N}$
- $b = 33,75 \text{ mm}$
- $M_z = F_{\parallel} * b = 4247,40 \text{ Nmm}$
- $y_1 = 55 \text{ mm}$
- $y_2 = 125 \text{ mm}$

Computations:

$$F_A = \frac{M_z * y_2}{2 * (y_2^2 + y_1^2)} = 14,23 \text{ N}$$

$$t_1 = F_A * \frac{y_1}{y_2} = 6,27 \text{ N}$$

$$t_2 = F_A * \frac{y_2}{y_2} = F_A = 14,23 \text{ N}$$

3) Tangential force due to moment in X direction

The last moment generated by the displacement of the shell's barycenter with respect to the center of the connecting plate is pointing along the X direction. In this case, the tangential forces produced are discharged on the two centering pins only. Indeed, the bolts are not designed to sustain tangential loads then, the through holes realized in the shell's connecting plate are bigger in diameter

(+10%) with respect to the bolt's outer diameter, while the centering pins holes are calibrated and allows to discharge the bolts from the tangential load.

The first step to compute the tangential forces acting on the two centering pins is the identification of the centroid location (figure 5.18). It corresponds to the rotational point of the plate when subjected to the M_x momentum. To compute the position of the centroid it is necessary to consider a point which will be the reference for all the length measurements. Since it can be chosen arbitrary it is better to choose a physical point of the considered component so that all the measurements could be easily done. In this case the lower left corner of the connecting plate has been considered as the reference point.

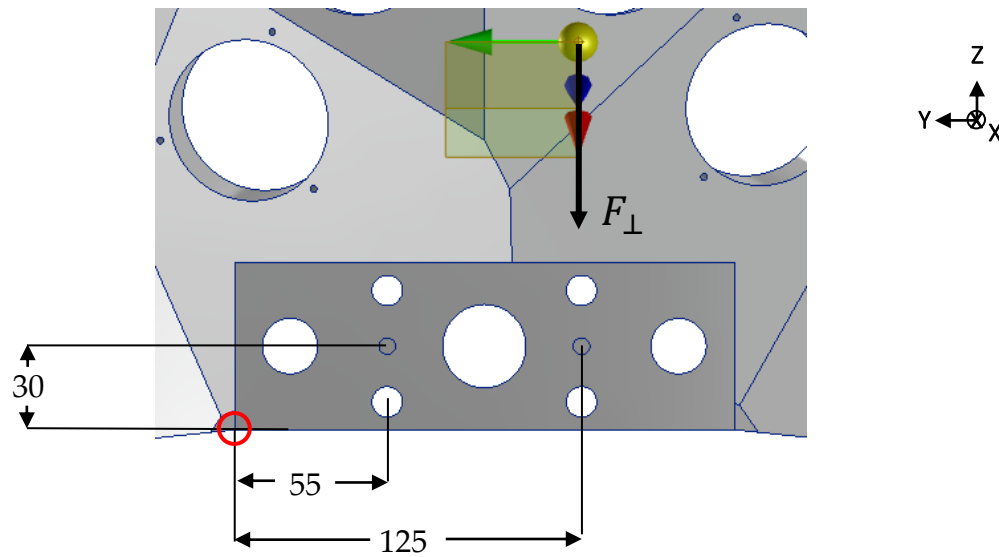


Figure 5.18: Detail of the frontal view of the upstream inferior quarter shell with the reference point highlighted in red.

Once the reference point has been identified it is possible to express the position of the centroid with respect to that point by computing the mean value of the distances of the two centering pins' holes from the reference point. For simplicity the position of the centroid has been computed by combining the distance in Z and Y directions:

$$z_c = \frac{z_1 + z_2}{2} = \frac{30 + 30}{2} = 30$$

$$y_c = \frac{y_1 + y_2}{2} = \frac{55 + 125}{2} = 90$$

Since the pins' holes are symmetric with respect to the center of the plate, the centroid is located exactly in the middle of it (figure 5.19).

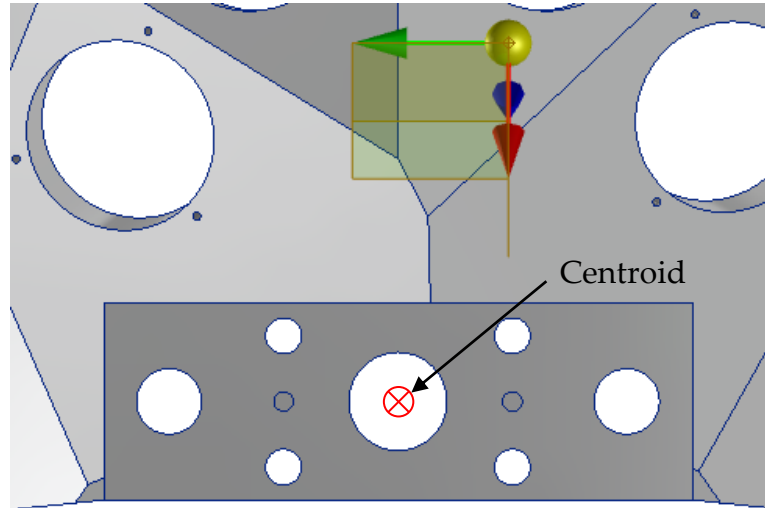


Figure 5.19: Detail of the frontal view of the upstream inferior quarter shell with the centroid highlighted in red.

Once the centroid has been located on the plate, it is necessary to compute the distance of each pin's hole with respect to the centroid (figure 5.20).

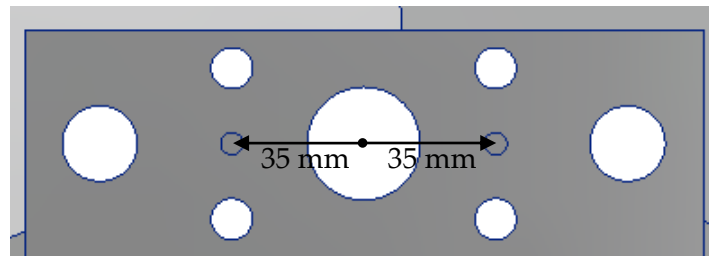


Figure 5.20: Detail of the connecting plate showing the distance of the two centering pins holes from the centroid.

$$r_1 = r_2 = 35 \text{ mm}$$

Then the tangential force acting on each pin is computed using the following formula coming from the shear stress definition:

SHEAR STRESS

$$\tau = \frac{M * r}{J}$$

TANGENTIAL FORCE

$$F_{T,i} = \frac{M_x * r_i}{\sum r_i^2}$$

- τ : shear stress [MPa]
- M : moment [Nmm]
- r : distance from the centroid [mm]
- J : polar moment of area [mm²]
- $F_{T,i}$: tangential force [N]
- M_x : moment [Nmm]
- r_i : distance from the centroid [mm]

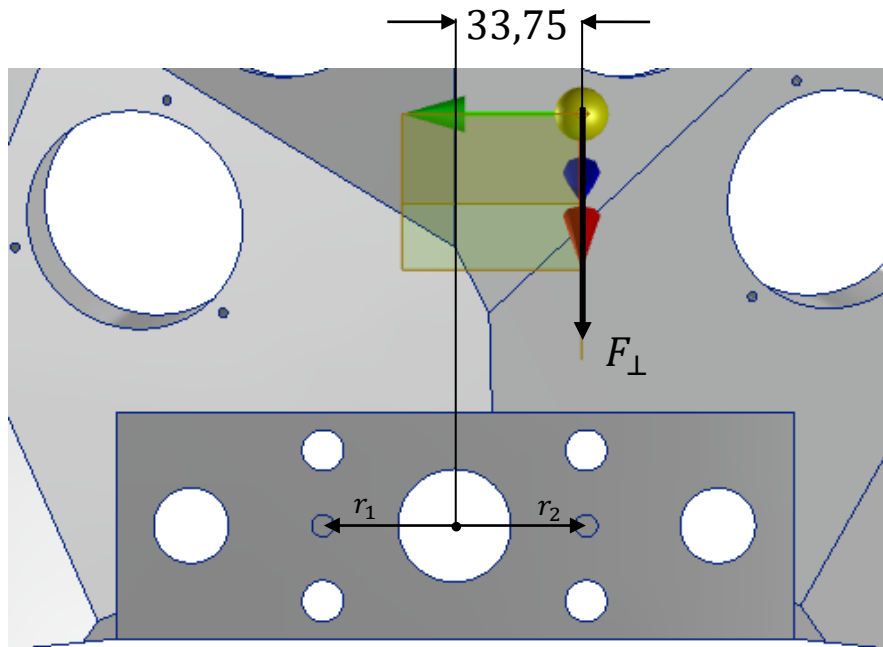


Figure 5.21: Detail of the connecting plate with all the data needed for the computation of the tangential forces acting on the centering pins.

Data:

- $F_{\perp} = 217,99 \text{ N}$
- $b = 33,75 \text{ mm}$
- $M_x = F_{\perp} * b = 7356,56 \text{ Nmm}$
- $\sum r_i^2 = 35^2 * 2 = 2450 \text{ mm}^2$

Computation:

$$F_{T,1} = F_{T,2} = \frac{M_x * r_1}{\sum r^2} = 105,09 \text{ N}$$

These forces have direction perpendicular to the radius connecting the centroid to the hole on which the forces are acting (figure 5.22).

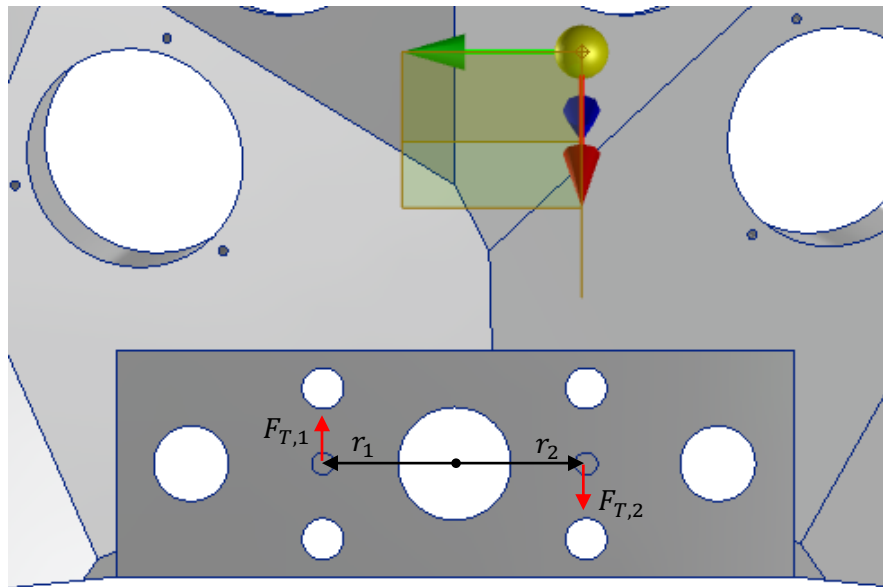


Figure 5.22: Detail of the connecting plate showing direction of the tangential forces due to M_x acting on the centering pins.

4) Tangential force due to weight

The perpendicular force F_{\perp} is not only responsible for the generation of the two moments M_y and M_x . It needs to be considered also as it is, a tangential force directly acting on the centering pins. This force is subdivided equally on the two pins:

$$F_T = \frac{F_{\perp}}{2} = 109 \text{ N}$$

This force must be vectorially added to the previously computed tangential forces and the most loaded pin must be identified. Indeed, even though the tangential forces due to the shell's weight are all pointing downwards, the tangential forces due to the M_x moment change in direction according to the position of the pins with respect to the centroid. Then, the summation of the two forces could be constructive or destructive depending on the position of the pins (figure 5.23).

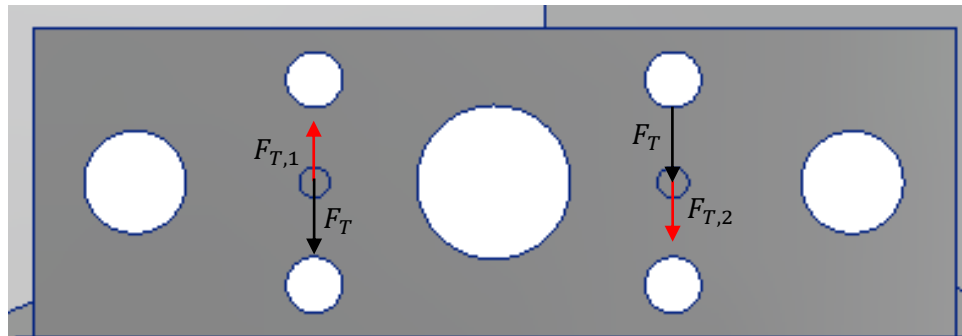


Figure 5.23: Detail of the connecting plate showing direction of the two tangential forces acting on the centering pins.

As can be seen from Figure 5.23, the most loaded pin is the n.2. Indeed, both the tangential force due to weight and the tangential force due to M_x are pointing in the same direction resulting in a constructive summation. The value of the resultant can then be computed by adding them together:

$$F_{TOT} = F_T + F_{T,2} = 214.09 \text{ N}$$

For the sake of completeness also the resultant tangential force acting on pin 1 has been computed:

$$f_{TOT} = F_T - F_{T,1} = 3,91 \text{ N}$$

5) Most loaded bolt

Once all the forces acting on both the bolts and the centering pins have been computed, it has been necessary to combine them considering the superposition of all the previously computed forces:

| | | | |
|---------|-------------------|------------|------------|
| BOLT 1: | Axial loads → | $t_2(M_y)$ | $t_2(M_z)$ |
| BOLT 2: | Axial loads → | $t_2(M_y)$ | $t_1(M_z)$ |
| BOLT 3: | Axial loads → | $t_1(M_y)$ | $t_1(M_z)$ |
| BOLT 4: | Axial loads → | $t_2(M_y)$ | $t_2(M_z)$ |
| PIN 1: | Tangential load→ | f_{TOT} | |
| PIN 2: | Tangential load → | F_{TOT} | |

With all these data computed it is then possible to enter them into the Inventor's tool to get the minimum diameter required by each bolt to withstand the loads (figure 5.24).

| | | |
|------------------------------------|------------------|------------------|
| Carichi | | |
| Fattore di tenuta | k | 1,50 su |
| Forza assiale massima | F _a | 49 N |
| Fattore input forza | n | 0,50 su |
| Forza tangente massima | F _t | 0 N |
| Fattore di attrito giunto | f | 0,40 su |
| Bullone | | |
| Numero bulloni | z | 1 su |
| Diametro filettatura | d | 2,500 mm |
| Passo filettatura | p | 0,800 mm |
| Diametro bullone medio | d _s | 1,980 mm |
| Diametro minimo bullone | d _{min} | 1,519 mm |
| Materiale | | Materiale utente |
| Resistenza allo snervamento | S _y | 689 MPa |
| Fattore di sicurezza richiesto | k _s | 3,00 su |
| Pressione filettatura ammissibile | p _a | 40 MPa |
| Modulo di elasticità | E | 206700 MPa |
| Fattore di attrito filettatura | f ₁ | 0,20 su |
| Fattore di attrito testa | f ₂ | 0,25 su |
| Materiale | | |
| Larghezza funzionale giunto | L | 15,500 mm |
| Modulo di elasticità | E | 206700 MPa |
| Risultati | | |
| Forza di precarico | F _v | 70,096 N |
| Forza operativa | F _{max} | 73,500 N |
| Momento serrante richiesto | M _u | 0,057 N m |
| Sollecitazione di trazione | σ _t | 38,705 MPa |
| Sollecitazione torsionale | τ _k | 82,551 MPa |
| Sollecitazione ridotta | σ _{red} | 148,129 MPa |
| Sollecitazione dalla forza massima | σ _{max} | 40,585 MPa |
| Pressione filettatura | p _c | 10,456 MPa |
| Verifica resistenza | | Positiva |

a) Sizing data of bolt 1

| | | |
|------------------------------------|------------------|------------------|
| Carichi | | |
| Fattore di tenuta | k | 1,50 su |
| Forza assiale massima | F _a | 41 N |
| Fattore input forza | n | 0,50 su |
| Forza tangente massima | F _t | 0 N |
| Fattore di attrito giunto | f | 0,40 su |
| Bullone | | |
| Numero bulloni | z | 1 su |
| Diametro filettatura | d | 2,500 mm |
| Passo filettatura | p | 0,800 mm |
| Diametro bullone medio | d _s | 1,980 mm |
| Diametro minimo bullone | d _{min} | 1,519 mm |
| Materiale | | Materiale utente |
| Resistenza allo snervamento | S _y | 689 MPa |
| Fattore di sicurezza richiesto | k _s | 3,00 su |
| Pressione filettatura ammissibile | p _a | 40 MPa |
| Modulo di elasticità | E | 206700 MPa |
| Fattore di attrito filettatura | f ₁ | 0,20 su |
| Fattore di attrito testa | f ₂ | 0,25 su |
| Materiale | | |
| Larghezza funzionale giunto | L | 15,500 mm |
| Modulo di elasticità | E | 206700 MPa |
| Risultati | | |
| Forza di precarico | F _v | 58,652 N |
| Forza operativa | F _{max} | 61,500 N |
| Momento serrante richiesto | M _u | 0,047 N m |
| Sollecitazione di trazione | σ _t | 32,386 MPa |
| Sollecitazione torsionale | τ _k | 69,074 MPa |
| Sollecitazione ridotta | σ _{red} | 123,945 MPa |
| Sollecitazione dalla forza massima | σ _{max} | 33,959 MPa |
| Pressione filettatura | p _c | 8,749 MPa |
| Verifica resistenza | | Positiva |

b) Sizing data of bolt 2

| | | |
|------------------------------------|----------------|------------------|
| Carichi | | |
| Fattore di tenuta | k | 1,50 su |
| Forza assiale massima | F_a | 13 N |
| Fattore input forza | n | 0,50 su |
| Forza tangente massima | F_t | 0 N |
| Fattore di attrito giunto | f | 0,40 su |
| Bullone | | |
| Numero bulloni | z | 1 su |
| Diametro filettatura | d | 2,500 mm |
| Passo filettatura | p | 0,800 mm |
| Diametro bullone medio | d_s | 1,980 mm |
| Diametro minimo bullone | d_{min} | 1,519 mm |
| Materiale | | Materiale utente |
| Resistenza allo snervamento | S_y | 689 MPa |
| Fattore di sicurezza richiesto | k_s | 3,00 su |
| Pressione filettatura ammissibile | p_a | 40 MPa |
| Modulo di elasticità | E | 206700 MPa |
| Fattore di attrito filettatura | f_1 | 0,20 su |
| Fattore di attrito testa | f_2 | 0,25 su |
| Materiale | | |
| Larghezza funzionale giunto | L | 15,500 mm |
| Modulo di elasticità | E | 206700 MPa |
| Risultati | | |
| Forza di precarico | F_v | 18,597 N |
| Forza operativa | F_{max} | 19,500 N |
| Momento serrante richiesto | M_u | 0,015 N m |
| Sollecitazione di trazione | σ_t | 10,269 MPa |
| Sollecitazione torsionale | τ_k | 21,901 MPa |
| Sollecitazione ridotta | σ_{red} | 39,300 MPa |
| Sollecitazione dalla forza massima | σ_{max} | 10,767 MPa |
| Pressione filettatura | p_c | 2,774 MPa |
| Verifica resistenza | | Positiva |

c) Sizing data of bolt 3

| | | |
|------------------------------------|----------------|------------------|
| Carichi | | |
| Fattore di tenuta | k | 1,50 su |
| Forza assiale massima | F_a | 21 N |
| Fattore input forza | n | 0,50 su |
| Forza tangente massima | F_t | 0 N |
| Fattore di attrito giunto | f | 0,40 su |
| Bullone | | |
| Numero bulloni | z | 1 su |
| Diametro filettatura | d | 2,500 mm |
| Passo filettatura | p | 0,800 mm |
| Diametro bullone medio | d_s | 1,980 mm |
| Diametro minimo bullone | d_{min} | 1,519 mm |
| Materiale | | Materiale utente |
| Resistenza allo snervamento | S_y | 689 MPa |
| Fattore di sicurezza richiesto | k_s | 3,00 su |
| Pressione filettatura ammissibile | p_a | 40 MPa |
| Modulo di elasticità | E | 206700 MPa |
| Fattore di attrito filettatura | f_1 | 0,20 su |
| Fattore di attrito testa | f_2 | 0,25 su |
| Materiale | | |
| Larghezza funzionale giunto | L | 15,500 mm |
| Modulo di elasticità | E | 206700 MPa |
| Risultati | | |
| Forza di precarico | F_v | 30,041 N |
| Forza operativa | F_{max} | 31,500 N |
| Momento serrante richiesto | M_u | 0,024 N m |
| Sollecitazione di trazione | σ_t | 16,588 MPa |
| Sollecitazione torsionale | τ_k | 35,379 MPa |
| Sollecitazione ridotta | σ_{red} | 63,484 MPa |
| Sollecitazione dalla forza massima | σ_{max} | 17,394 MPa |
| Pressione filettatura | p_c | 4,481 MPa |
| Verifica resistenza | | Positiva |

d) Sizing data of bolt 4

Figure 5.24: Bolts' sizing data obtained by imposing the previously computed forces on all the four connecting bolts.

As expected, the most loaded bolt is the n.1. Indeed, it is subjected to both the maximum axial forces due to M_y and M_z . However, the Inventor sizing tool return a minimum diameter for the bolt n.1 equal to 2,5 mm which is much lower

than the M10x1,5 bolt used in the CAD model. The selected bolts are therefore compatible with the application and give to the connection a high safety factor.

Even the two centering pins can be sized using the same Inventor's tool entering as inputs the tangential forces acting on them (figure 5.25):

| | | |
|------------------------------------|------------------|------------------|
| Carichi | | |
| Fattore di tenuta | k | 1,50 su |
| Forza assiale massima | F _a | 0 N |
| Fattore input forza | n | 0,50 su |
| Forza tangente massima | F _t | 214 N |
| Fattore di attrito giunto | f | 0,40 su |
| Bullone | | |
| Numero bulloni | z | 1 su |
| Diametro filettatura | d | 5,000 mm |
| Passo filettatura | p | 0,800 mm |
| Diametro bullone medio | d _s | 4,480 mm |
| Diametro minimo bullone | d _{min} | 4,019 mm |
| Materiale | | Materiale utente |
| Resistenza allo snervamento | S _y | 689 MPa |
| Fattore di sicurezza richiesto | k _s | 3,00 su |
| Pressione filettatura ammissibile | p _a | 40 MPa |
| Modulo di elasticità | E | 206700 MPa |
| Fattore di attrito filettatura | f ₁ | 0,20 su |
| Fattore di attrito testa | f ₂ | 0,25 su |
| Materiale | | |
| Larghezza funzionale giunto | L | 15,500 mm |
| Modulo di elasticità | E | 206700 MPa |
| Risultati | | |
| Forza di precarico | F _v | 802,838 N |
| Forza operativa | F _{max} | 802,838 N |
| Momento serrante richiesto | M _u | 1,235 N m |
| Sollecitazione di trazione | σ _t | 63,301 MPa |
| Sollecitazione torsionale | τ _k | 96,913 MPa |
| Sollecitazione ridotta | σ _{red} | 179,398 MPa |
| Sollecitazione dalla forza massima | σ _{max} | 63,301 MPa |
| Pressione filettatura | p _c | 25,845 MPa |
| Verifica resistenza | | Positiva |

| | | |
|------------------------------------|------------------|------------------|
| Carichi | | |
| Fattore di tenuta | k | 1,50 su |
| Forza assiale massima | F _a | 0 N |
| Fattore input forza | n | 0,50 su |
| Forza tangente massima | F _t | 4 N |
| Fattore di attrito giunto | f | 0,40 su |
| Bullone | | |
| Numero bulloni | z | 1 su |
| Diametro filettatura | d | 2,500 mm |
| Passo filettatura | p | 0,800 mm |
| Diametro bullone medio | d _s | 1,980 mm |
| Diametro minimo bullone | d _{min} | 1,519 mm |
| Materiale | | Materiale utente |
| Resistenza allo snervamento | S _y | 689 MPa |
| Fattore di sicurezza richiesto | k _s | 3,00 su |
| Pressione filettatura ammissibile | p _a | 40 MPa |
| Modulo di elasticità | E | 206700 MPa |
| Fattore di attrito filettatura | f ₁ | 0,20 su |
| Fattore di attrito testa | f ₂ | 0,25 su |
| Materiale | | |
| Larghezza funzionale giunto | L | 15,500 mm |
| Modulo di elasticità | E | 206700 MPa |
| Risultati | | |
| Forza di precarico | F _v | 14,663 N |
| Forza operativa | F _{max} | 14,663 N |
| Momento serrante richiesto | M _u | 0,012 N m |
| Sollecitazione di trazione | σ _t | 8,096 MPa |
| Sollecitazione torsionale | τ _k | 17,268 MPa |
| Sollecitazione ridotta | σ _{red} | 30,985 MPa |
| Sollecitazione dalla forza massima | σ _{max} | 8,096 MPa |
| Pressione filettatura | p _c | 2,086 MPa |
| Verifica resistenza | | Positiva |

Figure 5.25: Sizing data obtained by imposing the previously computed forces on the two centering pins.

As can be noticed from the results of the pins' sizing, to sustain all the tangential load coming from the superposition of the weight force and the M_x momentum, it is required a centering pin with a minimum 5 mm diameter. The two $\phi 6$ pins are then compatible with their application.

5.2.3 Automation structure's connecting plate

It is the component in charge of connecting the automation structure with the detectors' shell. It is a 60x180x20 mm stainless steel plate on which proper holes have been made to accommodate the shell's supporting bolts on one side and both the actuator and the cylindrical guides' bolts on the other side (figure 5.27). As made for the detectors' shell, a FEM analysis is performed on this component to verify its stresses and deformations when subjected to all the forces coming from the mechanical coupling.

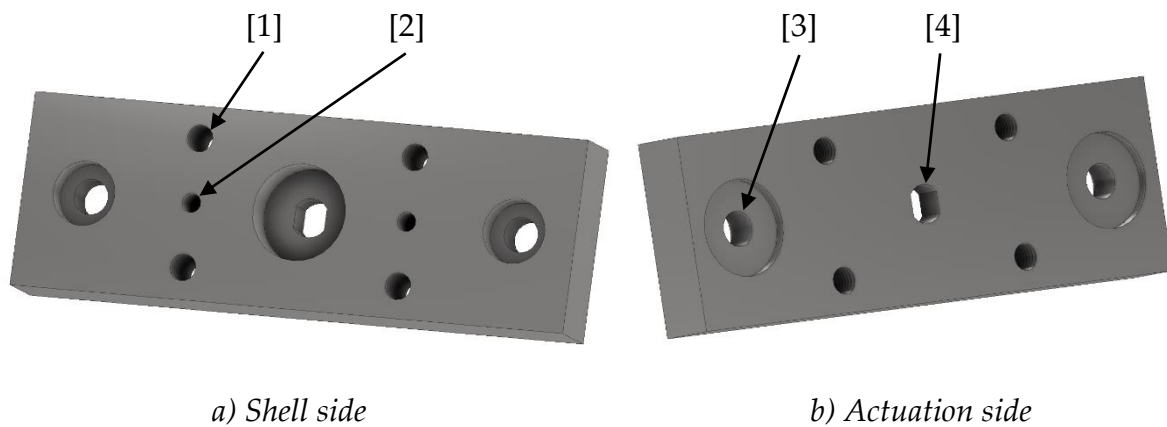


Figure 5.27: Frontal and rear view of the connecting plate. [1] threaded holes for the four bolts sized in chapter 5.2.2, [2] calibrated holes for two centering pins, [3] counterbore holes for the centering and the connection of the two cylindrical guides, [4] connection hole for the actuator stem.

1) Constraints

The two cylindrical guides' housing are used as FEM's constraints (figure 5.28). Indeed, the counterbore hole block the guides in place when they are screwed to the plate avoiding the possibility of the guides to move on the plate surface.

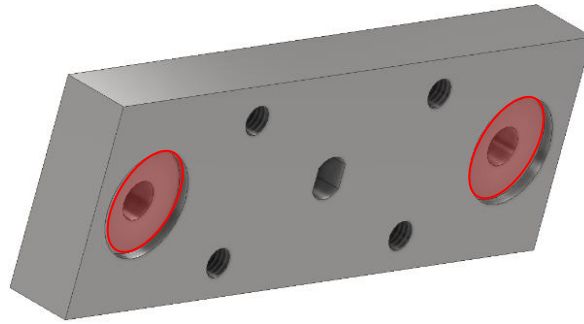



Figure 5.28: Rear view of the connecting plate with highlighted in red the two counterbore holes used as FEM's constraints.

2) Forces

Since the forces acting on the shell's connecting bolts have been previously computed, they are directly added in the FEM analysis by imposing the correct force combination to each bolt's hole. Moreover, it is necessary to consider the actuator force acting on the plate when the two cylindrical guides' end stops block the actuator extension. These data are obtained from the actuator data sheet considering an operating pressure equal to 6 bar.

Forza teorica


(Unità: N)

| Diametro [mm] | Diametro stelo [mm] | Pressione d'esercizio | Area pistone [mm ²] | Pressione di esercizio [MPa] | | | | | | | | |
|------------------|---------------------------|--------------------------|------------------------------------|------------------------------|-----|-----|-----|------|------|------|------|------|
| | | | | 0.2 | 0.3 | 0.4 | 0.5 | 0.6 | 0.7 | 0.8 | 0.9 | 1.0 |
| 32 | 12 | OUT | 804 | 161 | 241 | 322 | 402 | 482 | 563 | 643 | 724 | 804 |
| | | IN | 691 | 138 | 207 | 276 | 346 | 415 | 484 | 553 | 622 | 691 |
| 40 | 16 | OUT | 1257 | 251 | 377 | 503 | 629 | 754 | 880 | 1006 | 1131 | 1257 |
| | | IN | 1056 | 211 | 317 | 422 | 528 | 634 | 739 | 845 | 950 | 1056 |
| 50 | 20 | OUT | 1963 | 393 | 589 | 785 | 982 | 1178 | 1374 | 1570 | 1767 | 1963 |
| | | IN | 1649 | 330 | 495 | 660 | 825 | 989 | 1154 | 1319 | 1484 | 1649 |

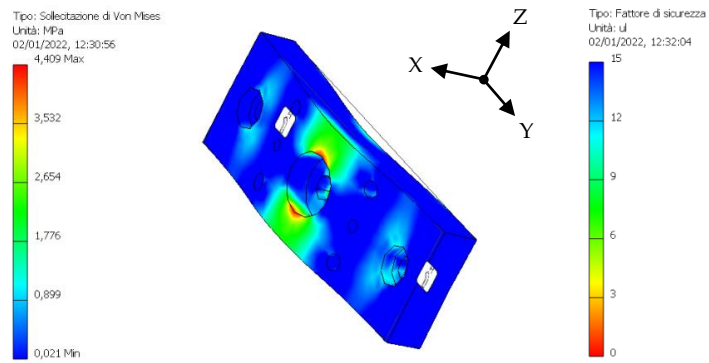
Figure 5.29: Table of theoretical extension and retraction forces of the MWB pneumatic actuator taken from the data sheet¹⁸

For the selected 32 mm actuator, the axial force acting on the connecting plate is equal to 482 N.

¹⁸ SMC, "Cilindro con bloccaggio, serie MWB", Tokyo, p. 9

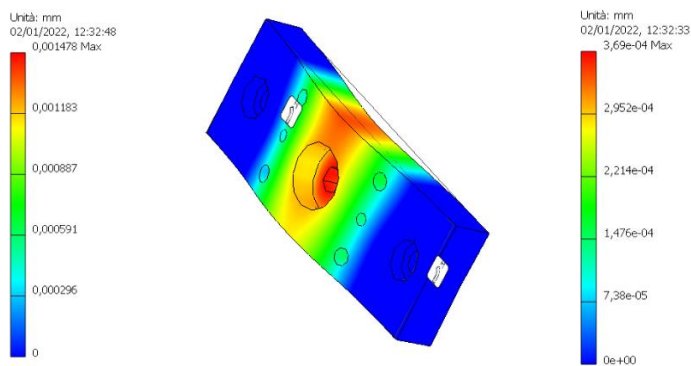
3) Results

The FEM analysis results are reported:



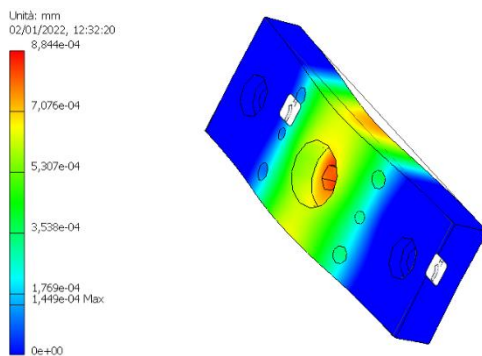
a) Von Mises stresses

b) Safety factor



c) X displacement

d) Y displacement



e) Z displacement

The FEM analysis results show the deformation of the plate in X-direction caused by the thrust of the actuator applied in the center of the plate. However, the safety

factor is higher than 15 in the whole component and the Von Mises stresses are much lower than the $R_{p0,2}$ of the stainless steel equal to 205 MPa. Moreover, the Y and the Z deformations are negligible, and the X deformation is two orders of magnitude lower than the admissible total displacement of the structure.

The designed connecting plate is then compatible with its application.

5.2.4 Cylindrical guides' connecting bolts

The automation structure's plate is connected to the cylindrical guides by means of two M10x1,5 bolts. It is then necessary to check if their size is compatible with the acting forces.

Thanks to the two guides' grooves machined on the plate, all the tangential loads coming from the shell's weight are discharged directly on the guides, leaving to the two bolts the task of sustain the axial load only. For simplicity, since the hinge effect coming from the geometry of the grooves is negligible (small distance of the "hinge" from the bolts' holes) the axial loads due to M_y and M_z are neglected. Moreover, according to a conservative perspective, the compressive axial force due to F_{\parallel} is not considered as acting on the bolts since it is absorbed directly by the two guides. The only force that is considered in the sizing is the axial force produced by the pneumatic actuator when the mechanical end stops blocked the actuator stroke. Indeed, when the shell reaches the working position, the two end stops connected to the cylindrical guides by means of the dedicated plate stop the translation of the shell and all the actuator thrust is discharged on the connecting plate and subsequently on the two considered bolts.

The axial load produced by the considered pneumatic actuator when fed by an inlet pressure equal to 6 bar is 482 N as described before. Then, each of the two bolts must be able to withstand 241 N which correspond to half of the total axial

force. This force is used as input in the Inventor sizing tool. Here are reported the main results:

Carichi

| | | |
|---------------------------|-------|---------|
| Fattore di tenuta | k | 1,50 su |
| Forza assiale massima | F_a | 482 N |
| Fattore input forza | n | 0,50 su |
| Forza tangente massima | F_t | 0 N |
| Fattore di attrito giunto | f | 0,40 su |

Bullone

| | | |
|-----------------------------------|-----------|------------------|
| Numero bulloni | z | 2 su |
| Diametro filettatura | d | 5,000 mm |
| Passo filettatura | p | 1,500 mm |
| Diametro bullone medio | d_s | 4,026 mm |
| Diametro minimo bullone | d_{min} | 3,160 mm |
| Materiale | | Materiale utente |
| Resistenza allo snervamento | S_y | 689 MPa |
| Fattore di sicurezza richiesto | k_s | 3,00 su |
| Pressione filettatura ammissibile | p_a | 40 MPa |
| Modulo di elasticità | E | 206700 MPa |
| Fattore di attrito filettatura | f_1 | 0,20 su |
| Fattore di attrito testa | f_2 | 0,25 su |

Materiale

| | | |
|-----------------------------|---|------------|
| Larghezza funzionale giunto | L | 23,000 mm |
| Modulo di elasticità | E | 206700 MPa |

Risultati

| | | |
|------------------------------------|----------------|-------------|
| Forza di precarico | F_v | 341,600 N |
| Forza operativa | F_{max} | 361,500 N |
| Momento serrante richiesto | M_u | 0,550 N m |
| Sollecitazione di trazione | σ_t | 43,565 MPa |
| Sollecitazione torsionale | T_k | 88,722 MPa |
| Sollecitazione ridotta | σ_{red} | 159,726 MPa |
| Sollecitazione dalla forza massima | σ_{max} | 46,103 MPa |
| Pressione filettatura | p_c | 12,690 MPa |
| Verifica resistenza | | Positiva |

Imposing a 482 N axial force on the threaded connection and considering two bolts, the recommended diameter for each bolt is equal to 5 mm. The selected M10X1,5 bolts are therefore compatible with the application and give the connection a high safety factor.

5.2.5 Cylindrical guides

They are the two components in charge of sustain all the shell's weight when the actuator is fully extended. They must be properly sized to avoid the excessive bend of the actuator's stem which can cause the locking of the actuation structure.

A preliminary sizing has already been made in solution 1, then a 30 mm diameter guides is used in this third solution. Since in this last solution it is not required the anti-rotation effect ensured by grooved guides, simpler cylindrical stainless-steel guides are selected. Their length equal to 590 mm is obtained by considering the

global structure's geometry and by ensuring a minimum distance between the sustain structure and the detectors when the actuator is fully retracted to avoid collisions. Moreover, a minimum 10 mm distance is considered between the end of the guides and the rear linear bearings when the actuator is fully extended to allow a proper regulation of the end stops (figure 5.30).

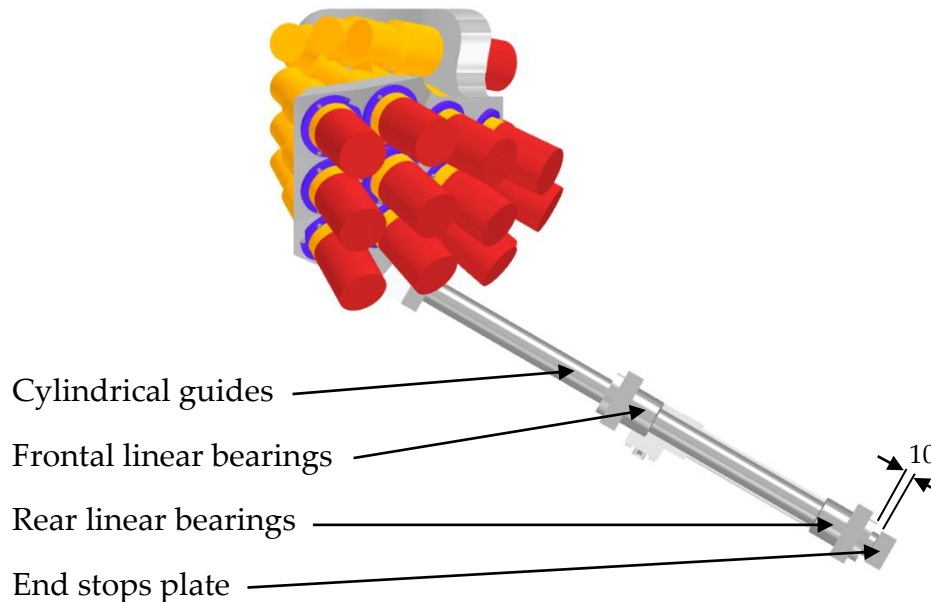
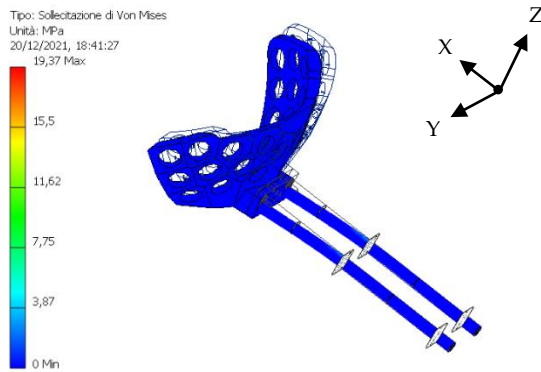


Figure 5.30: Lateral view of the system with the indication of the minimum distance between the end of the guides and the rear linear bearings when the actuator is fully extended.

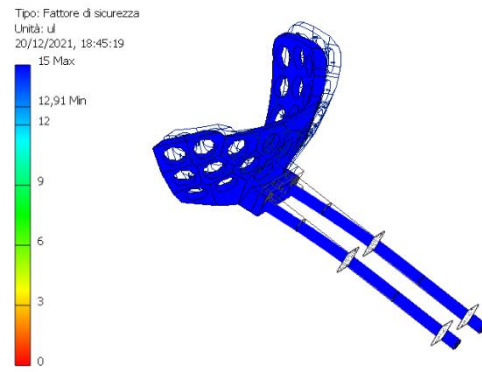
Since these components will work in different configurations depending on the positioning phase (actuator fully extended, actuator fully retracted, ...) four most critical configuration are considered during the FEM analysis.

1) Actuator fully extended

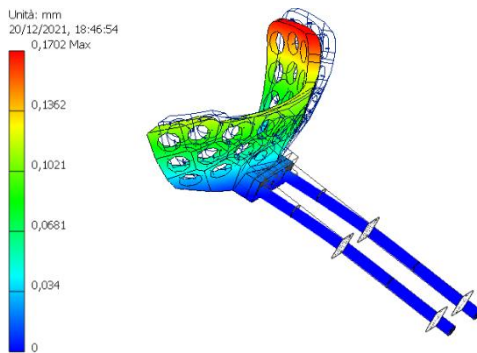
When the actuator is fully extended the frontal and the rear linear bearings are positioned at 257,655 mm and 560,971 mm respectively from the shell



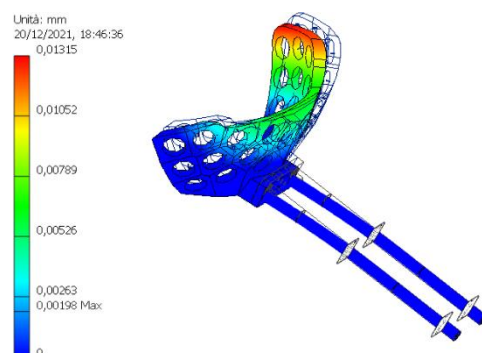
a) Von Mises stresses



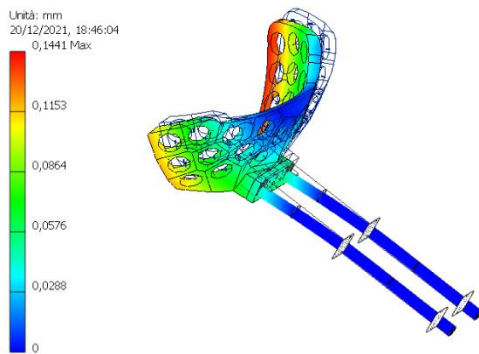
b) Safety factor



c) X displacement



d) Y displacement



e) Z displacement

The FEM analysis results show a great deformation of the two cylindrical guides as expected. In both the X and Z directions the maximum displacement exceeds 0,1 mm. However, the safety factor never drops below 12 in the whole

component and the Von Mises stresses are much lower than the $R_{p0,2}$ of the stainless steel equal to 205 MPa.

The two cylindrical guides are then compatible with their application, but their deformation must be kept under control in the physical structure to verify that the mathematical model is respected. If more deformation is found in the physical model, the two guides must be replaced with larger diameter ones to avoid excessive bending of the system that can cause the rupture of the actuator stem and an incorrect positioning of the shell.

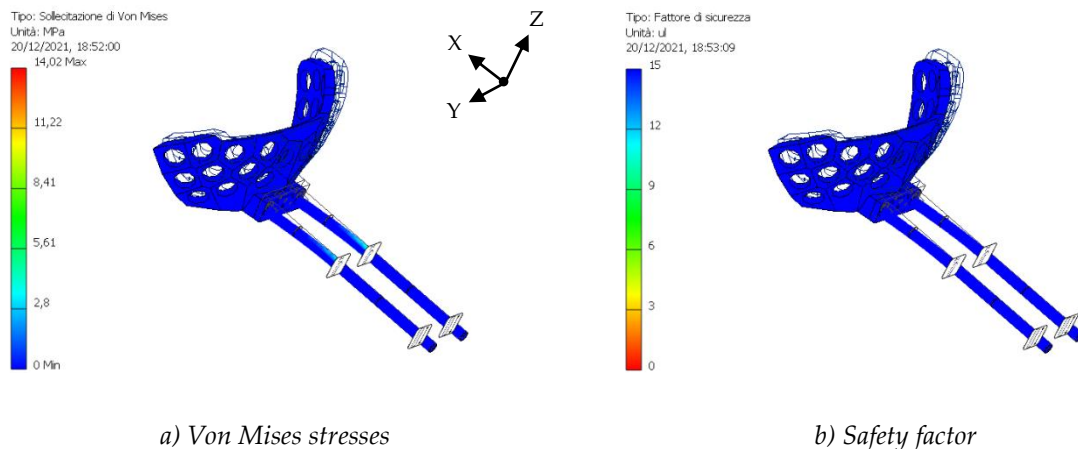
1b. Frontal linear bearings locked

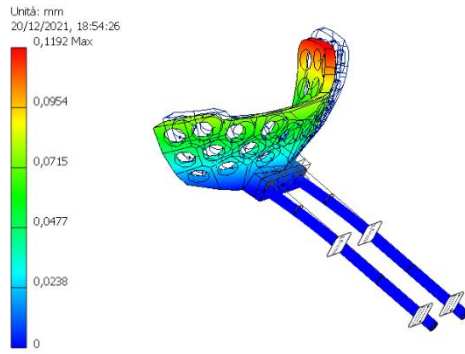
For this second configuration the two constraints are exchanged resulting in a simple clamped cantilever beam.

The forces acting on this second configuration are the same as the previous case.

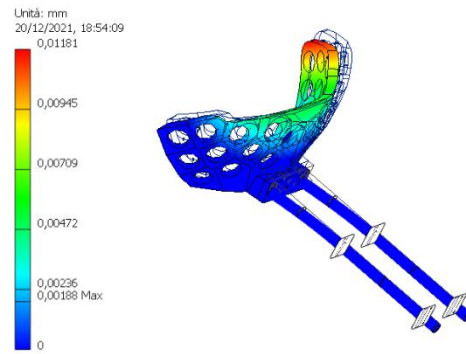
The FEM analysis is then straightforward since it only requires the exchange of the previously imposed constraints.

The main results are here reported:

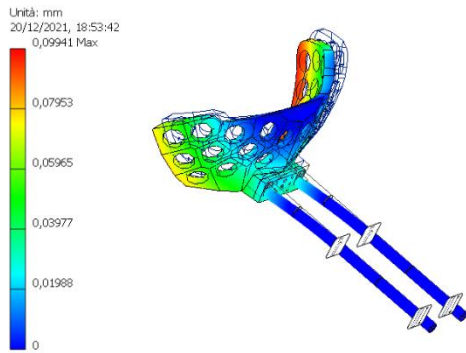




c) X displacement



d) Y displacement



e) Z displacement

This second configuration is less critical than the previous one. The two cylindrical guides reach a maximum tension equal to 14 MPa, more than 5 MPa lower than in the other simulation. Even the deformations are lower by about 30% confirming the higher rigidity of the system if considered clamped in correspondence of the frontal linear bearings.

2) Actuator fully retracted

Since the total actuator's stroke which allow the shell not to collide with the high intensity line during the horizontal translation is equal to 150 mm, the two bearings' positions of this second configuration are translated by a 150 mm with respect to previous ones. The frontal bearings are then located 107,655 mm far from the end of the guides and the rear ones 410,971 mm.

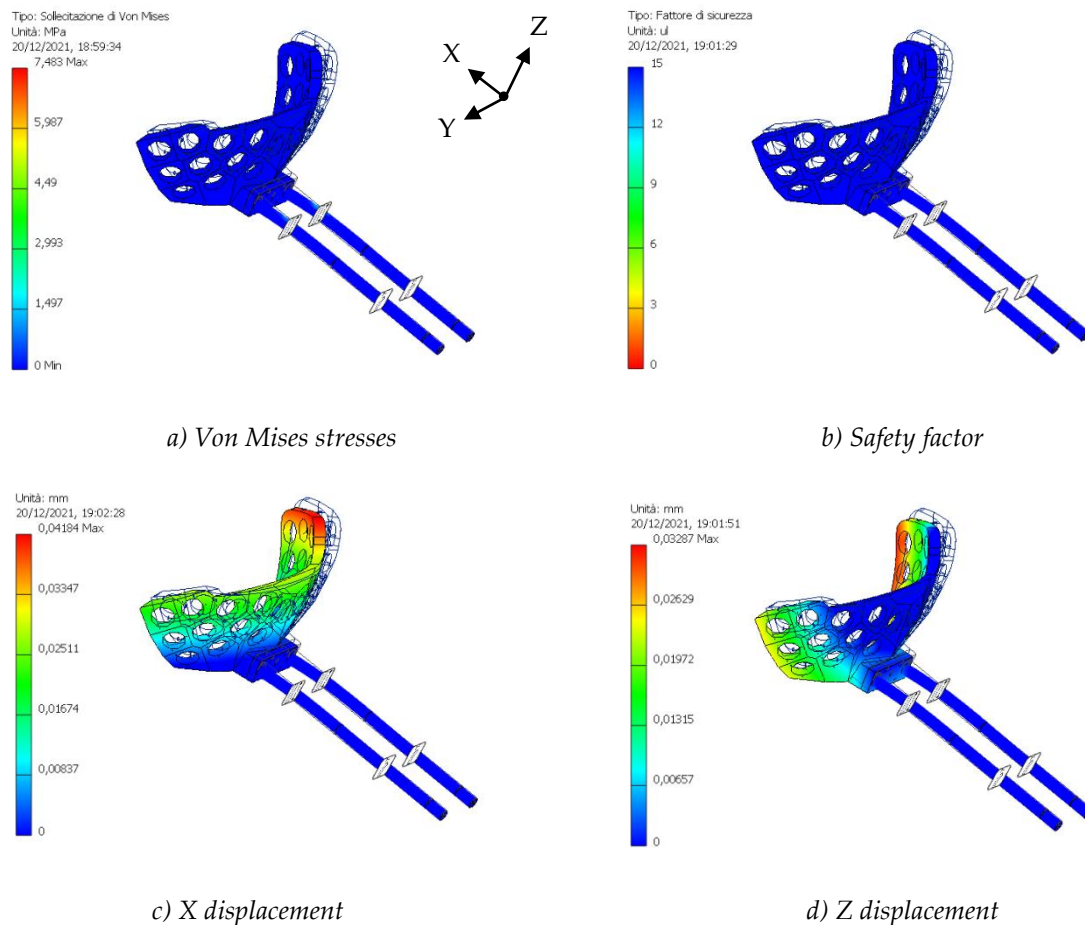
Here too, the possible clamping configuration are two:

2a. Rear linear bearings locked

As happens in case 1a, the rear bearings are considered as clamps, while the frontal ones are considered as carts.

The forces acting on the system are the same of case 1a.

The same FEM analysis of case 1a is performed on the system considering the positioning variation of the four linear bearings. Here are reported the main results:



As expected, reducing the cantilever part of the two guides, the deformation is drastically reduced and the Von Mises stresses are more than halved. Since the

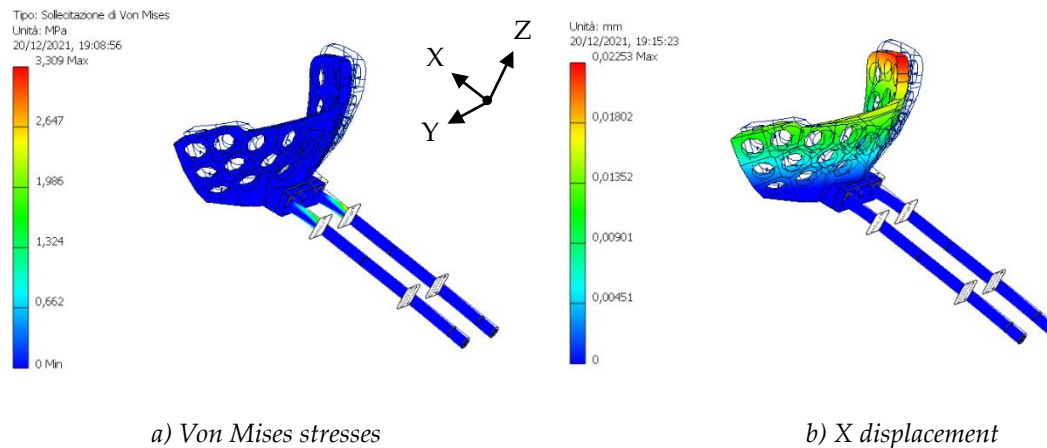
deformation increase together with the length of the cylindrical guides, to minimize the uncontrolled deformation of the system, the minimum admissible stroke of the actuator which allows the shell to be lowered below the high intensity line is selected.

2b. Frontal linear bearings locked

As happens in case 1b, the frontal bearings are considered as clamps, while the rear ones are considered as carts. Globally the system is considered as a simple cantilever beam.

The forces acting on the guides are the same of the previous cases.

The same FEM analysis of case 1b is performed on the system considering the positioning variation of the four linear bearings. Here are reported the main results:



In this last case, for sake of simplicity, only the Von Mises stresses and the X displacement are reported. As noticed in case 1b, by considering the frontal bearings as clamps, both the deformations and the stresses decrease. In this second configuration the difference between case 2a and 2b is much more evident since the Von Mises stresses decrease by about 50%, from 7,5 MPa to 3,3 MPa.

5.2.6 End stops plate's bolts

On the other side of the guides with respect to the shell a 190x40x20 mm stainless steel plate is bolted to the end of the guides (figure 5.32).

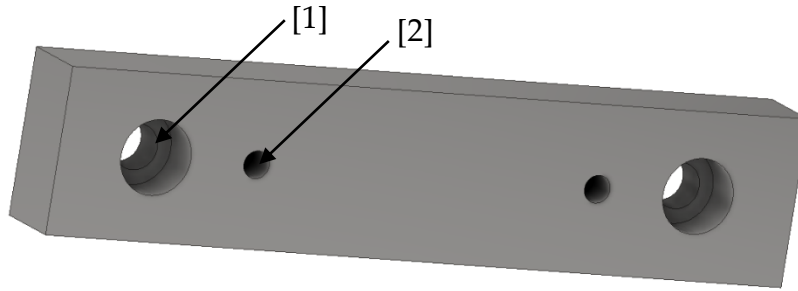


Figure 5.32: Render of the end stop plate.

[1] cylindrical guides bolts' holes, [2] end stop threaded holes.

This component oversees limiting the stroke of the actuator to the correct length obtained from the mathematical model. Indeed, two mechanical end stops are mounted on this plate thanks to two threaded holes [2]. The regulation is performed by simply imposing the correct length to the end stops which will collide with the rear linear bearings when the actuator reaches a certain extension. These components must then be properly sized to withstand all the load produced by the actuator. It is necessary to size both the bolt's couples connecting the guides with the plate and the end stops bolts. These two bolt's couples are subjected to the same force, then their sizing can be simultaneously done. Since the only force acting on these bolts is the axial load produced by the actuator, the sizing has already been done in section 5.2.4 and it is here reported:

Carichi

| | | |
|---------------------------|----------------|---------|
| Fattore di tenuta | k | 1,50 su |
| Forza assiale massima | F _a | 482 N |
| Fattore input forza | n | 0,50 su |
| Forza tangente massima | F _t | 0 N |
| Fattore di attrito giunto | f | 0,40 su |

Bullone

| | | |
|-----------------------------------|------------------|------------------|
| Numero bulloni | z | 2 su |
| Diametro filettatura | d | 5,000 mm |
| Passo filettatura | p | 1,500 mm |
| Diametro bullone medio | d _s | 4,026 mm |
| Diametro minimo bullone | d _{min} | 3,160 mm |
| Materiale | | Materiale utente |
| Resistenza allo snervamento | S _y | 689 MPa |
| Fattore di sicurezza richiesto | k _s | 3,00 su |
| Pressione filettatura ammissibile | p _a | 40 MPa |
| Modulo di elasticità | E | 206700 MPa |
| Fattore di attrito filettatura | f ₁ | 0,20 su |
| Fattore di attrito testa | f ₂ | 0,25 su |

Materiale

| | | |
|-----------------------------|---|------------|
| Larghezza funzionale giunto | L | 23,000 mm |
| Modulo di elasticità | E | 206700 MPa |

Risultati

| | | |
|------------------------------------|------------------|-------------|
| Forza di precarico | F _v | 341,600 N |
| Forza operativa | F _{max} | 361,500 N |
| Momento serrante richiesto | M _u | 0,550 N m |
| Sollecitazione di trazione | σ _t | 43,565 MPa |
| Sollecitazione torsionale | τ _k | 88,722 MPa |
| Sollecitazione ridotta | σ _{red} | 159,726 MPa |
| Sollecitazione dalla forza massima | σ _{max} | 46,103 MPa |
| Pressione filettatura | p _c | 12,690 MPa |
| Verifica resistenza | | Positiva |

Carichi

| | | |
|---------------------------|----------------|---------|
| Fattore di tenuta | k | 1,50 su |
| Forza assiale massima | F _a | 482 N |
| Fattore input forza | n | 0,50 su |
| Forza tangente massima | F _t | 0 N |
| Fattore di attrito giunto | f | 0,40 su |

Bullone

| | | |
|-----------------------------------|------------------|------------------|
| Numero bulloni | z | 1 su |
| Diametro filettatura | d | 5,500 mm |
| Passo filettatura | p | 1,500 mm |
| Diametro bullone medio | d _s | 4,526 mm |
| Diametro minimo bullone | d _{min} | 3,660 mm |
| Materiale | | Materiale utente |
| Resistenza allo snervamento | S _y | 689 MPa |
| Fattore di sicurezza richiesto | k _s | 3,00 su |
| Pressione filettatura ammissibile | p _a | 40 MPa |
| Modulo di elasticità | E | 206700 MPa |
| Fattore di attrito filettatura | f ₁ | 0,20 su |
| Fattore di attrito testa | f ₂ | 0,25 su |

Materiale

| | | |
|-----------------------------|---|------------|
| Larghezza funzionale giunto | L | 22,000 mm |
| Modulo di elasticità | E | 206700 MPa |

Risultati

| | | |
|------------------------------------|------------------|-------------|
| Forza di precarico | F _v | 679,475 N |
| Forza operativa | F _{max} | 723,000 N |
| Momento serrante richiesto | M _u | 1,192 N m |
| Sollecitazione di trazione | σ _t | 64,594 MPa |
| Sollecitazione torsionale | τ _k | 123,827 MPa |
| Sollecitazione ridotta | σ _{red} | 223,990 MPa |
| Sollecitazione dalla forza massima | σ _{max} | 68,732 MPa |
| Pressione filettatura | p _c | 20,612 MPa |
| Verifica resistenza | | Positiva |

a) Two bolts analysis

b) Single bolt analysis

Figure 5.33: End stops' bolts sizing

Since during the set-up of the experiment it could happens that only one of the two end stops effectively enters in contact with the back of the linear bearings, the end stops analysis is performed considering only one bolt sustaining all the axial force (figure 5.33 b).

In this last case the sizing tool return a minimum diameter equal to 5,5 mm which is smaller than the M6x0,75 bolts used as end stops in the CAD model. Even

the two M10x1,5 bolts used for the connection of the cylindrical guides are strong enough to withstand the load generated by the pneumatic actuator.

5.2.7 End stops' plate

It is a 190x40x20 mm stainless steel plate bolted to the opposite side of the guides with respect to the shell (figure 5.33). It has the task of stopping in the right position the actuator stroke so that the shell can reach the ideal working position. A FEM analysis on this component is useful to understand if the plate is sufficiently robust to withstand the actuator force and how it bends when the two end stops block the travel of the two cylindrical guides.

1) Constraints

The two cylindrical surfaces corresponding to the end stops' holes are selected as constraints. Indeed, when the two fine pitch bolts collide with the two linear bearings, the plate stops to move while the two guides continue to pull (figure 5.34)



Figure 5.34: Render of the end stop plate with highlighted in red the two surfaces imposed as constraints in the FEM analysis.

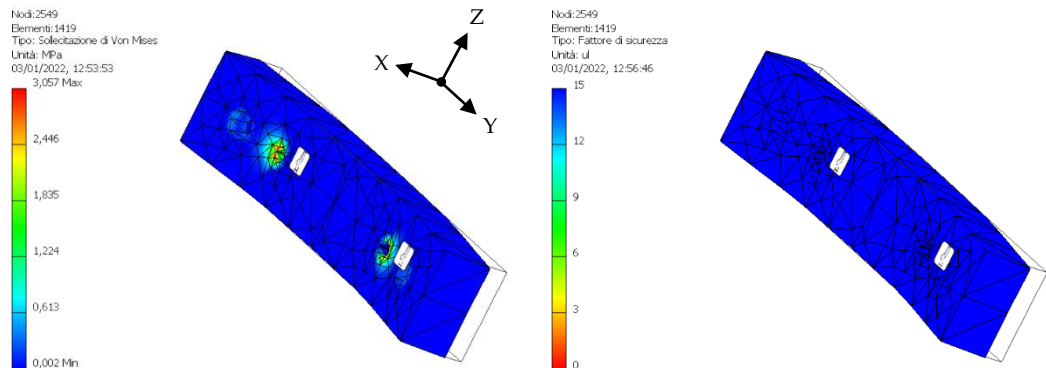
2) Forces

The only force that has been considered in the FEM analysis is the axial force coming from the actuator which is transmitted by the two cylindrical guides. Since the guides are two, the 482 N forces has been split into two symmetrical

components acting on the guides connecting bolts' holes. The gravity force has not been considered since it is negligible.

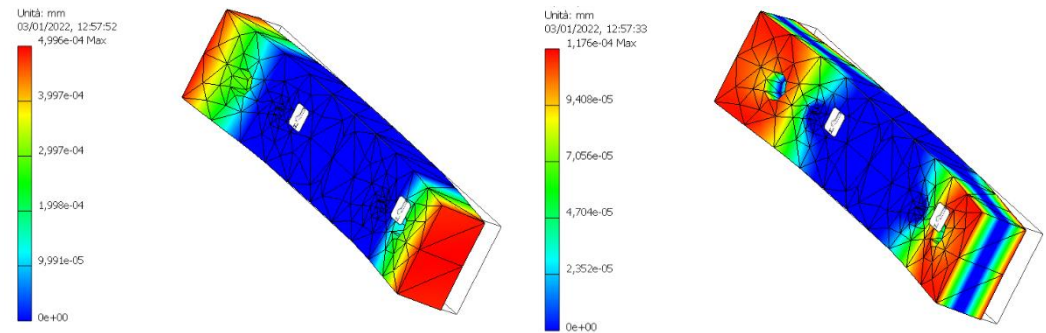
3) Results

The main results of the FEM analysis are here reported:



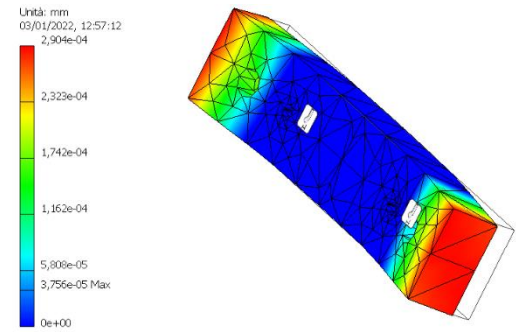
a) Von Mises stresses

b) Safety factor



c) X displacement

d) Y displacement



e) Z displacement

The main results of the application of an axial force on the extremities of the plate is the deformation of the plate itself along the X direction. All the stresses are concentrated in correspondence of the end stop bolts, but they are much lower than the stainless steel $R_{p_{0,2}}$. Moreover, all the deformations are negligible with respect to the admissible shell displacement error, reaching a maximum value two order of magnitude lower than the allowed one. The plate is then compatible with its application.

5.2.8 Cylindrical bearings

Four SLHFCS30 stainless steel Misumi flanged linear bushings are used to sustain the two cylindrical guides (figure 5.35).

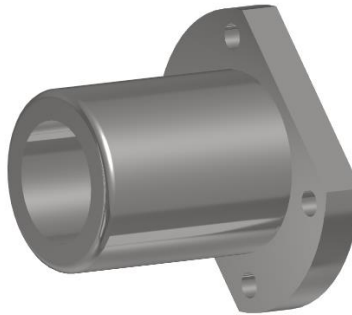


Figure 5.35: Render of the SLHFCS30 Misumi flanged linear bearing.

They are mounted on their respective supporting plates thanks to four M6x1,5 mm bolts and provide both the weight support and the linear translation of the shell. Their principle is based on the use of preloaded recirculating balls which allows the smooth translation of the guides without leaving any clearance between the balls and the guides themselves. Since they are responsible for the weight support of the shell, it is necessary to check if they can withstand both the forces and the momentums acting on them. As happens for the sizing of the cylindrical guides, it is necessary to consider four different setup configurations depending on the positioning step (actuator fully extended/retracted, frontal/rear bearings blocked).

Indeed, each of these configurations will return a different value for each reaction force, and the worst case will be used for the sizing of the bearings.

1) Actuator fully extended – rear bearings blocked

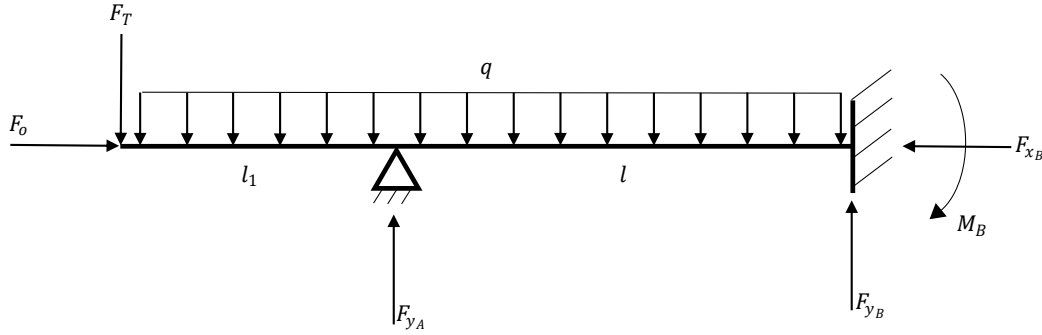


Figure 5.36: Representation of the system of cylindrical guides schematized as a hyperstatic cantilever beam with a clamped end and a cart support.

As can be seen from the above image, the system can be schematized into an hyperstatic beam subjected to a couple of perpendicular forces representing the shell's weight. The two linear bearings are considered as clamps on one end and as carts positioned at a distance l from the clamped end.

To solve this hyperstatic system it is firstly necessary to consider the superposition of effects caused by the simultaneous action of different forces on the guides and then to add to the system of equations the so-called compatibility equations which make the number of unknowns equal to the number of equations making the whole system solvable.

First, all the forces acting on the cantilever part of the beam must be transported in proximity of the cart (figure 5.37). This can be done by moving the forces in correspondence of the cart section and by introducing a transport bending moment which takes into account the force displacement.

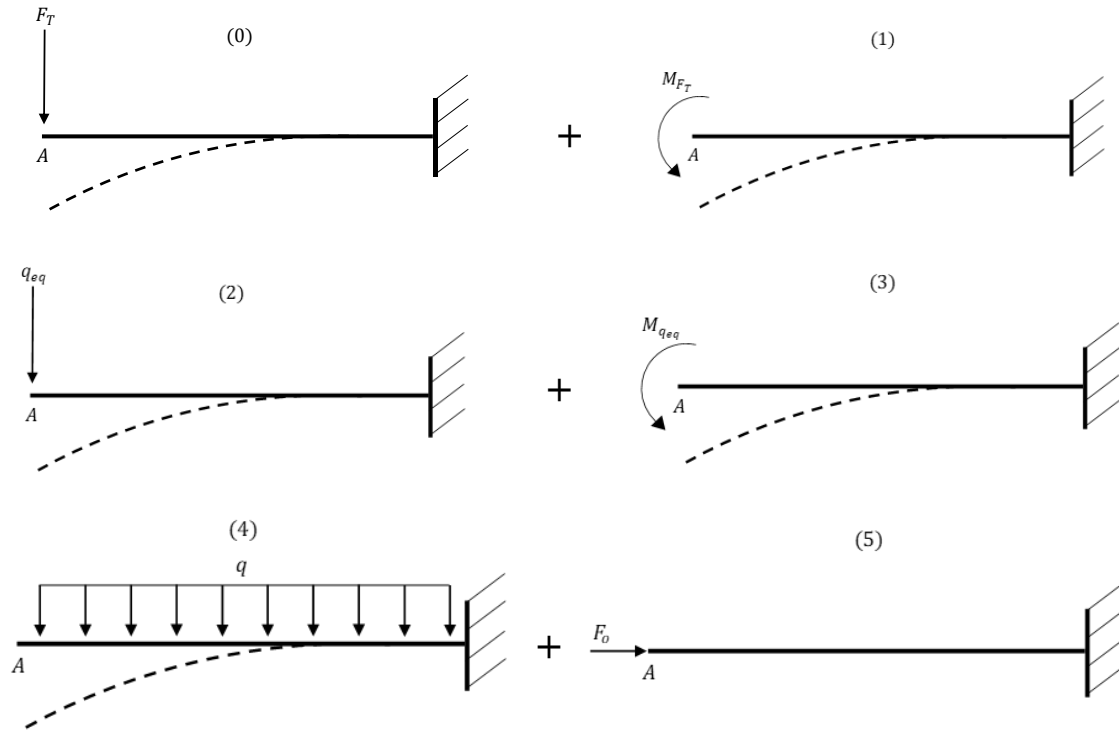


Figure 5.37: Schematic representation of all the forces acting on the system transported to A point corresponding to the cart placement.

Then, the cart can be removed from the model by inserting a vertical reaction force in correspondence of it whose entity is unknown (figure 5.38).

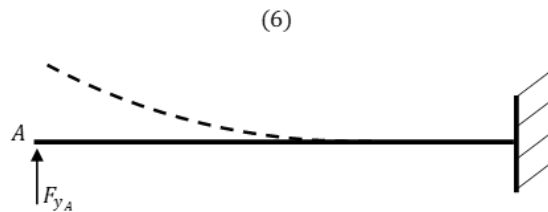


Figure 5.38: Schematic representation cantilever beam with the sustain cart substituted by its vertical reaction force.

Finally, it is possible to introduce the compatibility equation which allows the whole hyperstatic system to be solved. Indeed, it is possible to observe that the presence of a cart in the middle of the beam does not allow the system to vertically move in correspondence of the cart itself. Then, a null vertical

displacement δ_A must be assigned to the A section. It is important to notice that the vertical displacement δ_A is theoretically produced by the superposition of effects caused by all the previously computed forces, then, it is necessary to express it as:

$$\delta_A = \delta_A(F_T) + \delta_A(M_{F_t}) + \delta_A(q_{eq}) + \delta_A(M_{q_{eq}}) + \delta_A(F_{y_A}) + \delta_A(q_{\perp}) = 0$$

with:

| | |
|--|---|
| $\delta_A(F_T) = \frac{F_T * l^3}{3EI}$ | $\delta_A(M_{F_t}) = \frac{M_{F_T} * l^2}{2EI}$ |
| $\delta_A(q_{eq}) = \frac{q * l_1 * l^3}{3EI}$ | $\delta_A(M_{q_{eq}}) = \frac{M_{q_{eq}} * l^2}{2EI}$ |
| $\delta_A(F_{y_A}) = -\frac{F_{y_A} * l^3}{3EI}$ | $\delta_A(q_{\perp}) = \frac{q_{\perp} * l^4}{8EI}$ |

Thanks to this compatibility equation it is possible to compute the value of the vertical reaction force F_{y_A} as:

$$F_{y_A} = \left(\frac{F_T * l^3}{3EI} + \frac{M_{F_T} * l^2}{2EI} + \frac{q_{\perp} * l_1 * l^3}{3EI} + \frac{M_{q_{eq}} * l^2}{2EI} + \frac{q_{\perp} * l^4}{8EI} \right) * \frac{3EI}{l^3}$$

simplifying:

$$F_{y_A} = \left(\frac{F_T * l}{3} + \frac{M_{F_T}}{2} + \frac{q_{\perp} * l_1 * l}{3} + \frac{M_{q_{eq}}}{2} + \frac{q_{\perp} * l^2}{8} \right) * \frac{3}{l}$$

Once the reaction force F_{y_A} is computed, the system can be solved using the simpler cantilever beam's formula (figure 5.39).

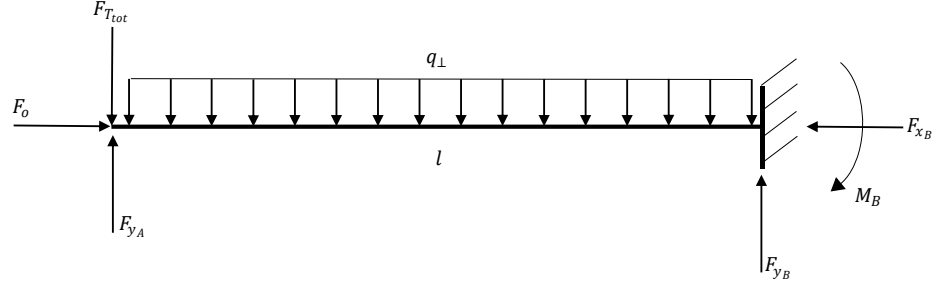


Figure 5.39: Schematic representation of a cantilever beam.

$$\sum F_x = 0 \rightarrow F_{x_B} = F_O$$

$$\sum F_y = 0 \rightarrow F_{y_B} + F_{y_A} = F_T + q_{\perp} * (l + l_1)$$

$$\sum M_B = 0 \rightarrow M_B + F_{y_A} * l - F_T * (l + l_1) - q_{\perp} * \frac{(l + l_1)^2}{2} = 0$$

And finally, the three clamp reaction forces can be computed.

$$F_{x_B} = F_O$$

$$F_{y_B} = F_T + q_{\perp} * (l + l_1) - F_{y_A}$$

$$M_B = F_T * (l + l_1) + q_{\perp} * \frac{(l + l_1)^2}{2} - F_{y_A} * l$$

It is important to point out that the following computations does not considers all the forces acting on the system. Some simplifications have been made to make the computation easily solvable. As an example, the shell's weight has been considered point-like and its barycenter has been considered positioned at the end of the beams. Then, all the transport moment due to the displacement of the real barycenter with respect to the ends of the guides have been neglected. This simplification is possible thanks to the entity of the bending moment produced by the tangential force acting on the cantilevered part of the beam which is an order of magnitude higher with respect to all the other moments.

Data:

- $l = 303,32 \text{ mm}$ (distance between the two linear bearings)
- $l_1 = 257,65 \text{ mm}$ (length of the cantilever part of the beam)
- $l_{tot} = 590 \text{ mm}$ (total guides' length)
- $P = 3,32 \text{ kg}$ (guides' weight)
- $q = \frac{P}{l_{tot}} * g = 0,055 \frac{\text{N}}{\text{mm}}$ (guides weight force per unit length)
- $F = 27,19 \text{ kg} * g = 266,76 \text{ N}$ (weight force due to shell and connecting plate)
- $F_{act} = 482 \text{ N}$ (actuator's axial force @ 6 bar)

Computations:

$$F_{\perp} = F * \cos(30) = 231,02 \text{ N}$$

$$F_{\parallel} = F * \sin(30) = 133,38 \text{ N}$$

$$q_{\perp} = q * \cos(30) = 0,048 \frac{\text{N}}{\text{mm}}$$

$$q_{\parallel} = q * \sin(30) = 0,028 \frac{\text{N}}{\text{mm}}$$

$$F_O = \frac{1}{2} F_{\parallel} + q_{\parallel} * l_{tot} - \frac{1}{2} F_{act} = -157,79 \text{ N (acting on each guide)}$$

$$F_T = \frac{1}{2} F_{\perp} = 115,51 \text{ N (acting on each guide)}$$

$$M_{F_T} = F_T * l_1 = 29761,15 \text{ Nmm}$$

$$M_{q_{eq}} = q_{\perp} * l_1 * \frac{l_1}{2} = 1593,20 \text{ Nmm}$$

$$F_{y_A} = \left(\frac{F_T * l}{3} + \frac{M_{F_T}}{2} + \frac{q_{\perp} * l_1 * l}{3} + \frac{M_{q_{eq}}}{2} + \frac{q_{\perp} * l^2}{8} \right) * \frac{3}{l} = 288,40 \text{ N}$$

$$F_{x_B} = F_O = -157,79 \text{ N}$$

$$F_{y_B} = F_T + q_{\perp} * (l + l_1) - F_{y_A} = -145,96 \text{ N}$$

$$M_B = F_T * (l + l_1) + q_{\perp} * \frac{(l + l_1)^2}{2} - F_{y_A} * l = -15127,35 \text{ Nmm}$$

2) Actuator retracted – rear bearings blocked

To compute the reaction forces of this second configuration the same formula of case 1 can be used. The only data that must be modified is the length of the cantilevered part of the guides.

Data:

- $l = 303,32 \text{ mm}$
- $l_1 = 107,65 \text{ mm}$
- $l_{tot} = 590 \text{ mm}$
- $F_{\perp} = 231,02 \text{ N}$
- $F_{\parallel} = 133,38 \text{ N}$
- $q_{\perp} = 0,048 \frac{\text{N}}{\text{mm}}$
- $q_{\parallel} = 0,028 \frac{\text{N}}{\text{mm}}$
- $F_O = -157,79 \text{ N}$ (on each guide)
- $F_T = 115,51 \text{ N}$ (on each guide)

Computations:

$$M_{F_T} = F_T * l_1 = 12435,23 \text{ Nmm}$$

$$M_{q_{eq}} = q_{\perp} * l_1 * \frac{l_1}{2} = 278,15 \text{ Nmm}$$

$$F_{y_A} = \left(\frac{F_T * l}{3} + \frac{M_{F_T}}{2} + \frac{q_{\perp} * l_1 * l}{3} + \frac{M_{q_{eq}}}{2} + \frac{q_{\perp} * l^2}{8} \right) * \frac{3}{l} = 189 \text{ N}$$

$$F_{x_B} = F_O = -157,79 \text{ N}$$

$$F_{y_B} = F_T + q_{\perp} * (l + l_1) - F_{y_A} = -53,76 \text{ N}$$

$$M_B = F_T * (l + l_1) + q_{\perp} * \frac{(l + l_1)^2}{2} - F_{y_A} * l = -5802,82 \text{ Nmm}$$

3) Actuator fully extended – frontal bearings blocked

In this third configuration the guides are considered as clamped in correspondence of the frontal linear bearings, then the whole system can be schematized by means of a cantilever model (figure 5.40).

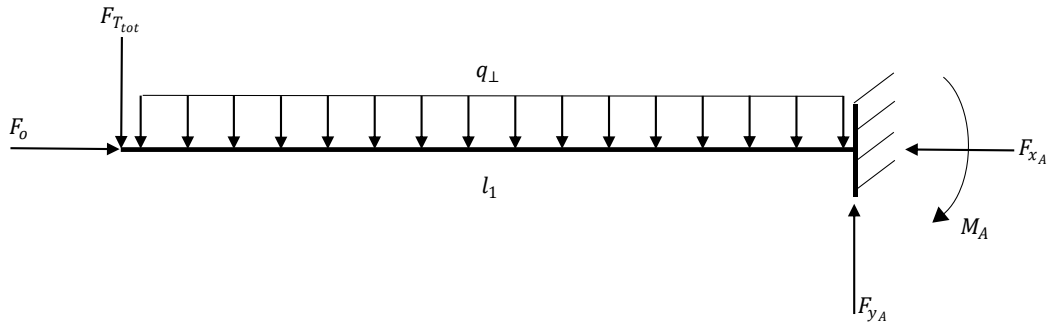


Figure 5.40: Representation of the system of cylindrical guides schematized as a cantilever beam.

Here, all the forces and momentums generated by the shell's weight are discharged on the frontal bearings only, so, the reaction forces' values obtained from the following computations must be used to check the compatibility of the selected bearings with the real structure.

Since a non-hyperstatic beam is considered, the following formulas are used to compute the reaction forces:

$$\sum F_x = 0 \rightarrow F_{xA} = F_o$$

$$\sum F_y = 0 \rightarrow F_{yA} = F_T + q_{\perp} * l_1$$

$$\sum M_A = 0 \rightarrow M_A = \frac{q_{\perp} * l_1^2}{2} + F_T * l_1$$

The computation is straightforward since the number of unknowns is equal to the number of linear equations.

Data:

All the data required by the formulas have already been listed in the first configuration.

Computations:

$$F_{x_A} = F_O = -157,79 \text{ N}$$

$$F_{y_A} = F_T + q_{\perp} * l_1 = 127,88 \text{ N}$$

$$M_A = \frac{q_{\perp} * l_1^2}{2} + F_T * l_1 = 31354,36 \text{ Nmm}$$

4) Actuator retracted – frontal bearings blocked

For this last configuration the same formulas of case 3 must be used. It is sufficient to modify the length of the cantilevered part of the guides as done in configuration 2.

Data:

All the data required by the formulas have already been listed in the second configuration.

Computations:

$$F_{x_A} = F_O = -157,79 \text{ N}$$

$$F_{y_A} = F_T + q_{\perp} * l_1 = 120,68 \text{ N}$$

$$M_A = \frac{q_{\perp} * l_1^2}{2} + F_T * l_1 = 12712,78 \text{ Nmm}$$

Once all the bearings' reactions forces have been computed for each of the four positioning configurations it is possible to verify if the selected bearings are suitable for their job. This check is performed by using the sizing procedure explained by the manufacturer (figure 5.41).

Allowable Load

•Basic Dynamic Load Rating(C)

Basic dynamic load rating is a constant load applied in a constant direction that enables each linear system of the same series to travel $50 \times 10^3 \text{m}$ under the same conditions, without 90% of the material suffering damage from rolling contact fatigue.

•Basic Static Load Rating(Co)

Basic static load rating is the static load exerted on contacting parts under maximum stress, at which the sum of the permanent deformation in the rolling element and rolling contact surface equals 0.0001 times the diameter of the rolling element.

•Allowable Static Moment(M_r , M_y , M_R)

Allowable static moment is a critical static moment load that acts upon a system at the loading moment. It is set in accordance with the permanent deformation as in basic static load rating C_o .

•Static Safety Factor(f_s)

Static safety factors are given in Table-1. When a linear system is still or moving at low speed, basic static load rating C_o must be divided by f_s in accordance with the conditions of use.

Table-1 Static Safety Factor(Lower Limit of f_s)

| Condition of Use | Lower Limit of f_s |
|---------------------------------------|----------------------|
| Under Normal Operating Conditions | 1~2 |
| When Smooth Travel is Required | 2~4 |
| When Subjected to Vibrations, Impacts | 3~5 |

$$\text{Allowable Load(N)} \leq C_o / f_s$$

$$\text{Allowable Moment(N-m)} \leq (M_r, M_y, M_R) / f_s$$

f_s : Static Safety Factor C_o : Basic Static Load(N)

M_r, M_y, M_R : Static Allowable Moment(N-m)

Figure 5.41: Bearing sizing procedure according to manufacturer's manual.

The allowable load computation formulas need some data that can be obtained from the data sheet of the bearings (figure 5.42).



| | | | |
|---|---|--|---|
|  | Boccole lineari_Boccole lineari con flangia/Singole | |  |
| | Codice componente SLHFC530 | | 20211122222955 |
| Tipo | Flangia | Stile | Standard |
| Con flangia | Flangia standard | Diametro del cerchio inscritto $d_i(\varnothing)$ | 30 |
| Lunghezza complessiva L(mm) | 64 | Materiale di Cilindro esterno | EN 1.4125 Equiv. |
| Trattamento superficie cilindro esterno | Senza trattamento superficie | Movimento | Movimento lineare |
| Con lubrificazione | Non fornito | Tipologia ricircolo di sfere | Tipo singolo |
| Diametro esterno $D(\varnothing)$ | 45 | Coefficiente di carico dinamico Valutazione (Dettaglio)(N) | 1570 |
| Coefficiente di carico statico base(N) | 2740 | Precisione | Grado elevato |
| Tolleranza cerchio inscritto (Minus Side)(mm) | -0.01 | Eccentricità (μm) | 15 |
| Tipo | Flangia standard | Lunghezza | Tipo singolo |
| Profilo flangia | Flangia compatta | Materiale sfera | EN 1.4125 Equiv. |
| Materiale fermo | Acciaio inox | Tenute | Con tenuta |
| Foro svasato piano | Standard | Rifornimento di grasso | Non fornito |

Figure 5.42: MISUMI linear bearings data sheet.

All the reaction forces are collected in a table considering their absolute values since bearings react at the same way both in tension and in compression. It is then possible to identify the worst case which will be used as a reference for the verification.

| | Frontal Bearing (A) | | | Rear Bearing (B) | | |
|--------|---------------------|--------|----------|------------------|--------|----------|
| | x_A | y_A | M_A | x_B | y_A | M_A |
| Case 1 | - | 288,40 | - | 157,79 | 145,96 | 15127,35 |
| Case 2 | - | 189 | - | 157,79 | 53,76 | 5802,82 |
| Case 3 | 157,59 | 127,88 | 31354,36 | - | - | - |
| Case 4 | 157,79 | 120,68 | 12712,78 | - | - | - |

From the table it is possible to notice that the maximum axial force acting on the bearings is equal to 157,79 N, the maximum tangential force is reached in case 1 on the rear bearing and it is equal to 145,96 N, while the maximum moment is applied to the frontal bearing in case 3 and it is equal to 31354,36 N.

Since the manufacturer provides the Basic Static Load Rating (C_o) only, the check on the admissible momentum is not feasible. Then, only the allowable load is checked.

$$Allowable\ Load(N) \leq \frac{C_o}{f_s}$$

Where:

- $C_o = 2740\ N$ (Basic Static Load Rating)
- $f_s = 2$ (static safety factor under normal operating condition)

Computations:

$$145,96\ N < \frac{2740}{2} = 1370\ N$$

Then the selected bearings are suitable for the application in terms of allowable tangential load.

5.2.9 Cylindrical bearings' supporting plates

The four cylindrical bearings are supported by two 68x270x20 mm stainless steel plates (figure 5.43).

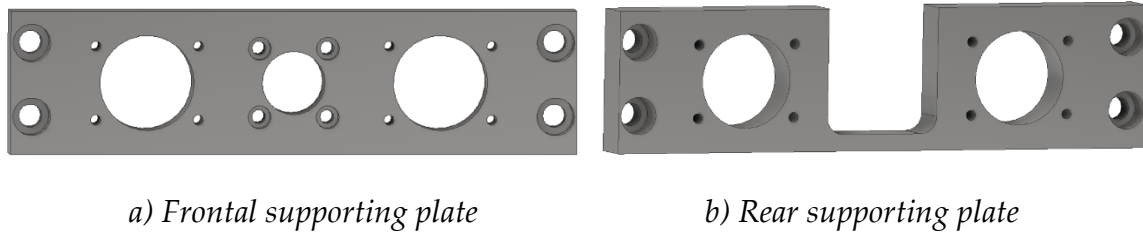


Figure 5.43: Renders of the frontal and rear linear bearings supporting plates.

They are directly bolted to the two uprights that connect the Stewart platform with the automation structure and have the task of both support the linear guides and the pneumatic actuator. To avoid the hyperstaticity of the actuator's joint, the actuator's body is bolted to the frontal supporting plate only, while the rear plate has been designed with a thinner steel bridge that connect the right and the left part of the plate leaving enough space to the actuator's body to move in free state condition (figure 5.44).

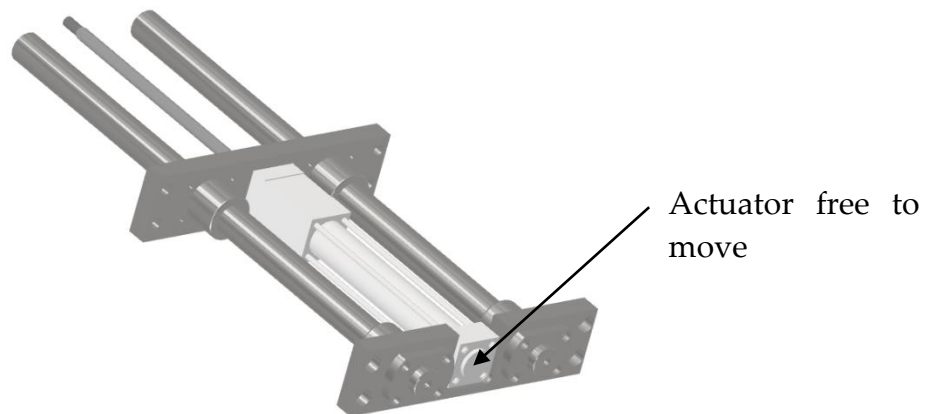


Figure 5.44: Render of the actuation structure

The FEM analysis on these two components can be performed in two different ways:

a) Considering the plates as singular elements

This first configuration allows to study the stresses and the deformations of the two plates when subjected to the reaction forces computed in the previous paragraph.

1) Constraints:

As FEM's constraints are considered the four connecting bolts' holes of each plate (figure 5.45).

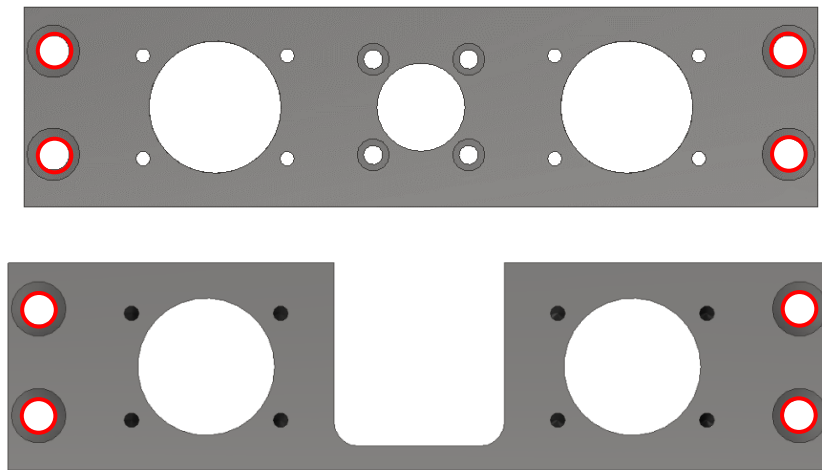


Figure 5.45: Frontal and rear cylindrical bearings supporting plates with highlighted in red the bolts holes used as FEM constraints.

Forces:

The forces acting on the plates have been taken from the force's summary table of paragraph 5.2.8. Indeed, all the forces and momentums' reactions previously computed for the cylindrical bearings are directly discharged on the supporting frame and the worst-case scenario for the frontal and the rear plate must be selected to check their compatibility in the system.

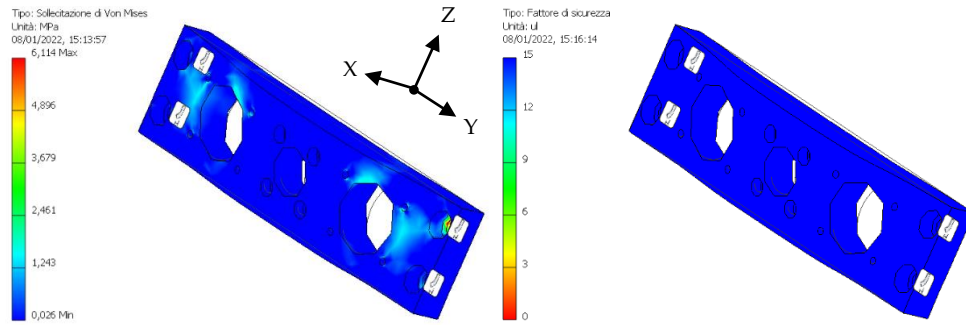
The worst-case scenario of the frontal plate is represented by the third positioning configuration described in the previous chapter, where the actuator is fully extended, and the frontal bearings are supposed to be blocked. In this case, both the axial force, the radial force and the momentum are discharged on the frontal bearings, while in the first configuration the tangential load only is present. Then, a 157,79 N axial force pointing towards the shell, a 127,88 N tangential force perpendicular to the axial force pointing downwards and a positive 31354,36 Nmm momentum in Y direction are applied to the two bearings' seats. The actuator's weight is not considered in the computation since it is negligible compared to the forces at stake (body's weight: 0,85 kg).

The rear plate worst-case scenario is represented by the first positioning configuration described in the previous chapter, where the actuator is fully extended, and the rear bearings are supposed to be blocked. In this case, both the axial force, the radial force and the momentum are discharged on the frontal bearings, while in the third and fourth configuration no force is supposed to be discharged on the rear bearings. Then, a 157,79 N axial force pointing towards the shell, a 145,96 N tangential force perpendicular to the axial force pointing downwards and a positive 15127,35 Nmm momentum in Y direction are applied to the two bearings' seats.

2) Results

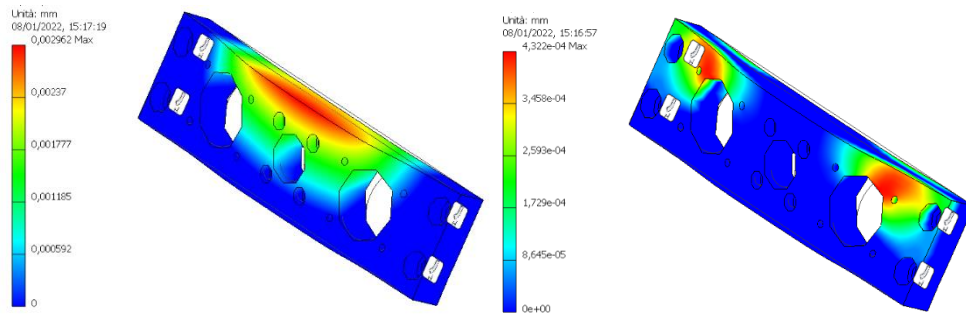
The analysis is then performed on both the sustaining plates. Here are reported the main results:

- Frontal cylindrical bearings supporting plate



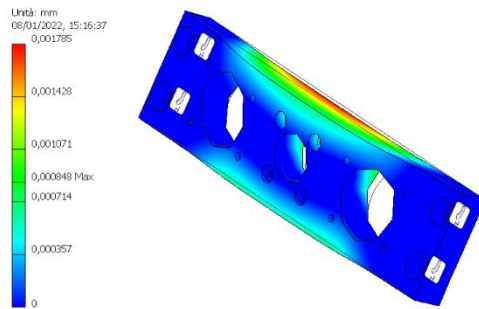
a) Von Mises stresses

b) Safety factor



c) X displacement

d) Y displacement



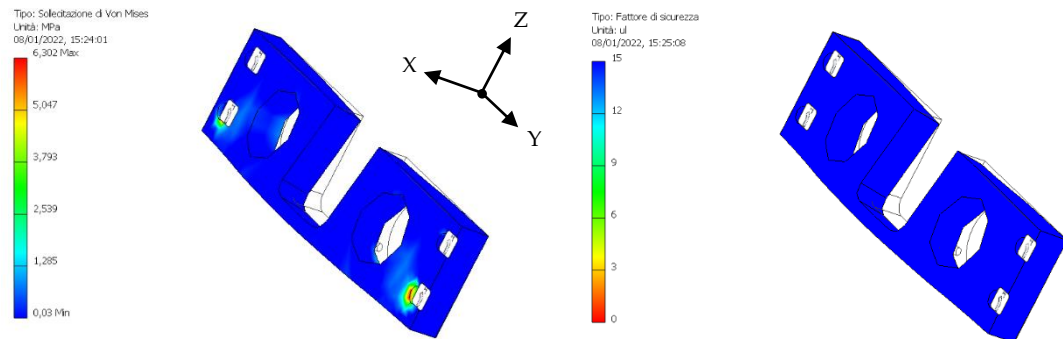
e) Z displacement

The FEM analysis results show the deformation of the plate in X-direction caused by the thrust of the actuator applied in the center of the plate. However, the safety factor is higher than 15 in the whole component and the Von Mises stresses are much lower than the $R_{p0.2}$ of the stainless steel equal to 205 MPa. Moreover, the Y and the Z deformations are negligible, and the

X deformation is two orders of magnitude lower than the admissible total displacement of the structure.

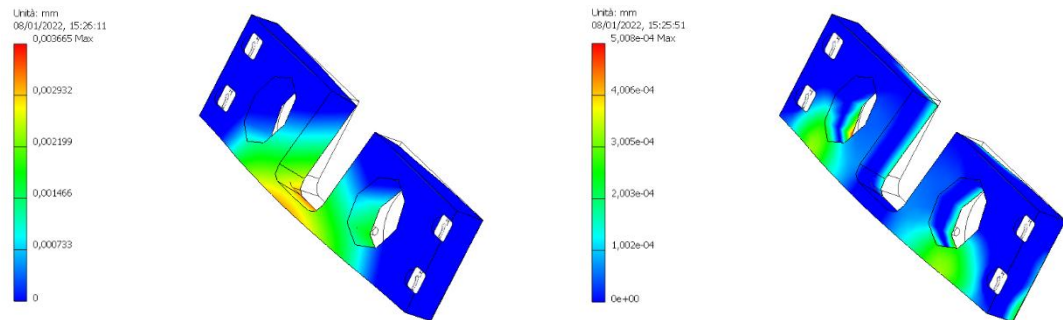
The designed frontal sustaining plate is then compatible with its application.

- Rear cylindrical bearings supporting plate



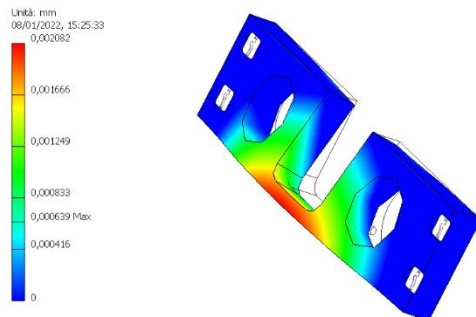
a) Von Mises stresses

b) Safety factor



c) X displacement

d) Y displacement



e) Z displacement

The FEM analysis results show that the main deformation of the plate is in X-direction as happens on the frontal sustain plate. However, even if the rear plate is weaker than the frontal plate due to the presence of the actuator's seat, the total deformation reaches a value equal to 0,0037 mm which is much lower than the admissible system displacement.

The Von Mises stresses are all concentrated in correspondence of the connection bolts' holes, but their values are much lower than the admissible stress, resulting in a safety factor higher than 15 in the whole plate. The plate is then compatible with its application.

b) Considering the whole system

This second configuration allows to appreciate the total shell's displacement with respect to the ideal position.

1) Constraints:

As FEM's constraints the eight connecting bolts' holes of the two supporting plates are considered (figure 5.46).

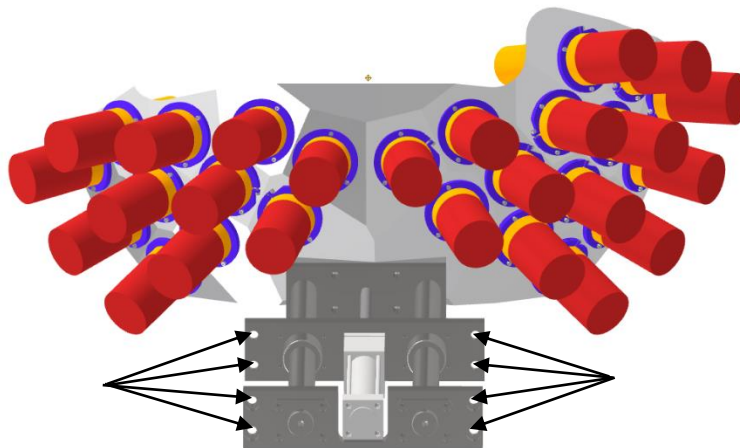


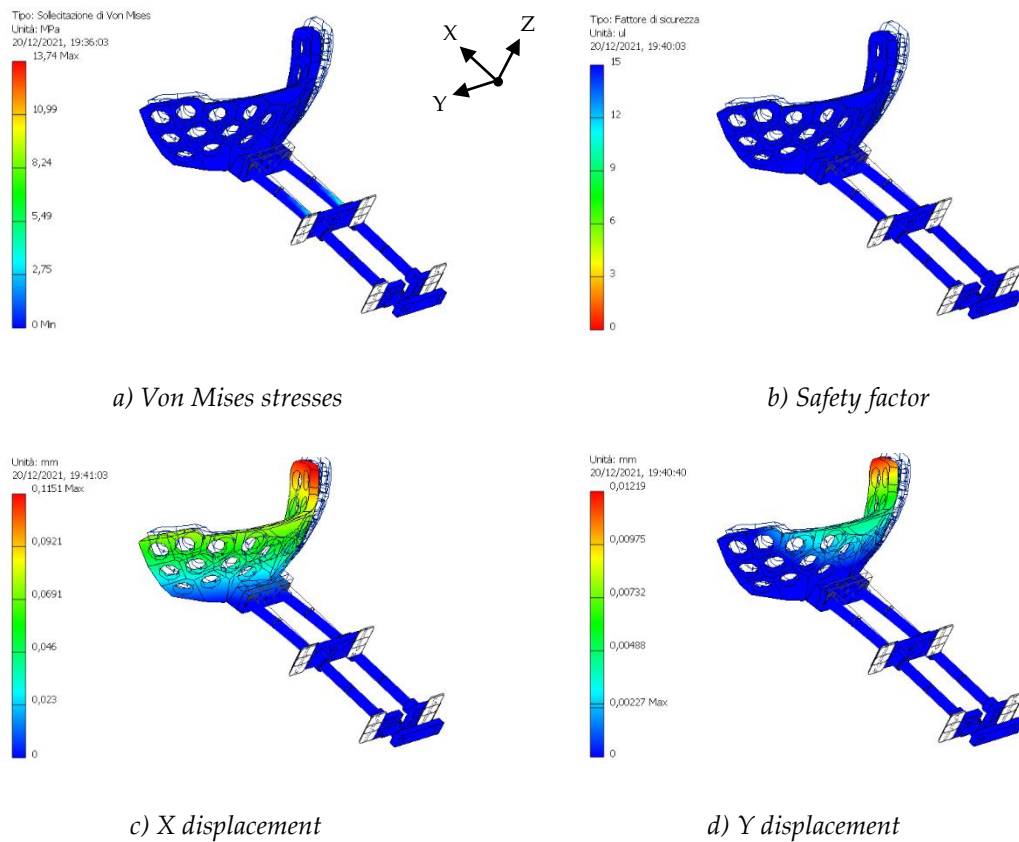
Figure 5.46: Automation structure with the holes used as FEM constraints indicated by an arrow.

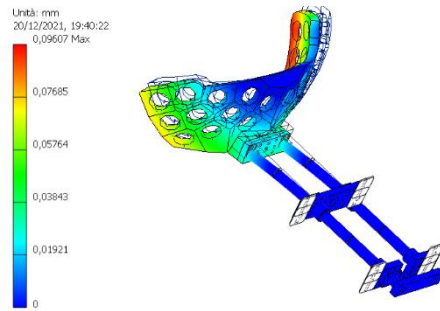
2) Forces:

Since the whole system is considered, the gravitational force must be added to the simulation. Moreover, as has already been made, all the detectors are removed from the model and a 7 N vertical force is imposed to each detectors' hole.

3) Results:

The results are obtained by generating a proper mesh refined in correspondence of the contacts between components to obtain more reliable stress and strain values. Here are reported the main results:





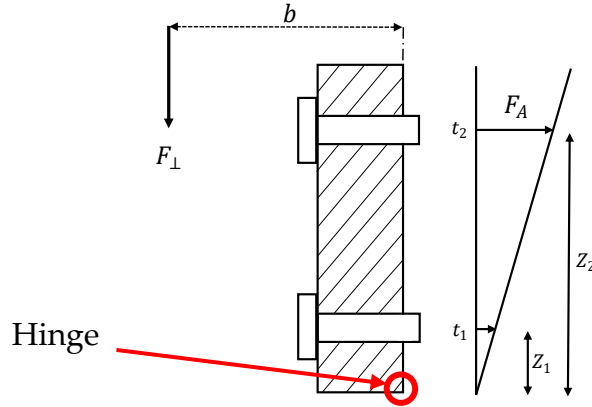
e) Z displacement

Considering the whole actuation structure stands out that both the X and the Z displacements reach a not negligible value. In particular, the computed X displacement reaches the same order of magnitude as the maximum positioning error accepted by the system. This deformation, however, does not pose a problem for the proper functioning of the system, but will have to be considered in defining the adjustment limits of the Stewart platform so that it can be compensated.

5.2.10 Supporting plates' connecting bolts

Each of the two bearings' supporting plates is connected to the two vertical uprights by means of four M10x1,5 mm ISO 4762 bolts. Thanks to the uprights design, all the tangential forces acting on the connecting plates are directly discharged on them, leaving to the bolts the task of supporting the axial force only. As has already been done in previous paragraphs, the axial force acting on each bolt is computed considering the lower edge of the plate as a hinge and by computing the axial force due to the momentum acting on the plates. Since this last data has already been computed in paragraph 5.2.8, the computation of the axial forces is straightforward. The same procedure used in the 5.2.2 paragraph (section 1) is considered.

The entity of the axial force acting on the bolts is directly proportional to the distance of the bolts from the hinge then, considering the following drawing:



the generic axial force t_i is expressed as:

$$t_i = F_A * \frac{z_i}{z_n}$$

with:

F_A : axial force acting on the most stressed bolt

z_i : distance of the i -th bolt from the hinge

z_n : distance of the furthest bolt from the hinge

Since the axial force is unknown it is possible to express it as function of the known moment M_y considering the following relations:

$$M_y = 2 * \left(F_A * z_n + F_A * \frac{z_{n-1}}{z_n} + \dots + F_A * \frac{z_1}{z_n} \right)$$

from which it is possible to derive the value of the axial force F_A as:

$$F_A = \frac{M_y * z_n}{2 * (z_n^2 + z_{n-1}^2 + \dots + z_1^2)}$$

Then, since the geometry of the connecting plate and the entity of the momentum are known, it is possible to compute the axial forces acting on each bolt (figure 5.47). For conservativity, the momentum with the higher entity is considered. It corresponds to the momentum acting on the frontal connecting plate when the actuator is fully extended, and the frontal bearings are considered as blocked. Since the computation require the total momentum acting on the plate it is necessary to double the value of the single momentum acting on each cylindrical bearing.

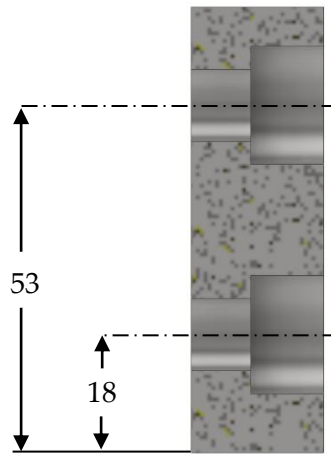


Figure 5.47: Lateral section of the frontal bearings supporting plate.

Data:

- $M_y = 31354,36 * 2 = 62708,72 \text{ Nmm}$
- $z_1 = 18 \text{ mm}$
- $z_2 = 53 \text{ mm}$

Computations:

$$F_A = \frac{M_y * z_2}{2 * (z_2^2 + z_1^2)} = 530,41 \text{ N}$$

$$t_1 = F_A * \frac{z_1}{z_2} = 180,14 \text{ N} \qquad t_2 = F_A * \frac{z_2}{z_2} = F_A = 530,41 \text{ N}$$

The value of the maximum axial force t_2 acting on the most stressed bolt has then been inserted in the bolt sizing Inventor's environment and the dimension of the smallest bolt able to sustain the given axial force is computed.

Carichi

| | | |
|---------------------------|-------|---------|
| Fattore di tenuta | k | 1,50 su |
| Forza assiale massima | F_a | 530 N |
| Fattore input forza | n | 0,50 su |
| Forza tangente massima | F_t | 0 N |
| Fattore di attrito giunto | f | 0,40 su |

Bullone

| | | |
|-----------------------------------|-----------|------------------|
| Numero bulloni | z | 1 su |
| Diametro filettatura | d | 6,000 mm |
| Passo filettatura | p | 1,500 mm |
| Diametro bullone medio | d_s | 5,026 mm |
| Diametro minimo bullone | d_{min} | 4,160 mm |
| Materiale | | Materiale utente |
| Resistenza allo snervamento | S_y | 689 MPa |
| Fattore di sicurezza richiesto | k_s | 3,00 su |
| Pressione filettatura ammissibile | p_a | 40 MPa |
| Modulo di elasticità | E | 206700 MPa |
| Fattore di attrito filettatura | f_1 | 0,20 su |
| Fattore di attrito testa | f_2 | 0,25 su |

Materiale

| | | |
|-----------------------------|---|------------|
| Larghezza funzionale giunto | L | 22,000 mm |
| Modulo di elasticità | E | 206700 MPa |

Risultati

| | | |
|------------------------------------|----------------|-------------|
| Forza di precarico | F_v | 744,876 N |
| Forza operativa | F_{max} | 795,615 N |
| Momento serrante richiesto | M_u | 1,415 N m |
| Sollecitazione di trazione | σ_t | 54,811 MPa |
| Sollecitazione torsionale | τ_k | 100,109 MPa |
| Sollecitazione ridotta | σ_{red} | 181,851 MPa |
| Sollecitazione dalla forza massima | σ_{max} | 58,545 MPa |
| Pressione filettatura | p_c | 18,789 MPa |
| Verifica resistenza | | Positiva |

The software returns, with an axial force equal to 530 N, a minimum diameter for the connecting bolts equal to 6 mm. Then, the M10x1,5 mm bolts are bigger enough to sustain the load and give to the connection a high safety factor.

5.2.11 Vertical uprights

The vertical uprights are the two elements in charge of connecting the upper Stewart platform's plate with the 30° tilted actuation structure (figure 5.48).

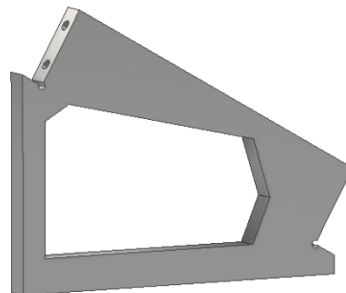


Figure 5.48: Lateral view of the vertical upright.

They are designed starting from a 20 mm thick rectangular stainless-steel plate which is properly modified in shape to fit with the connected components. The external boundary's shape is obtained by considering the general systems' dimensions and by imposing the lower edge of the plate to be 280 mm wide.

Moreover, the middle point of the lower edge is imposed to be 590 mm far in X direction with respect to the Z origin axis and the right vertical edge 15 mm long. Knowing these lengths it is possible to compute all the others edge dimensions by considering the following scheme:

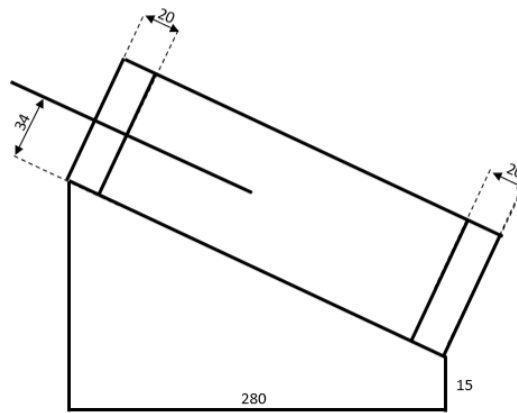


Figure 5.49: Schematic representation of the actuation structure from which it is possible to compute the dimensions of the vertical uprights.

Once the external boundaries' shape is defined, it is possible to lighten the structure by using an optimizing Inventor's tool which use a topological approach to remove material from the plate maintaining the mechanical properties required by the problem unchanged. This tool needs as input the position and the entity of all the forces and momentums acting on the component, the position of the constraints' surfaces and the indication of the material's zone which will not be modified by the optimizing process. With all this data, the tool can generate an ideal plate's shape which is able to sustain all the indicated loads and

simultaneously reduce to the minimum the weight of the component. For this purpose, the connection between the bearings' supporting plates and the uprights is supposed to be rigid and all the forces and momentum acting on the supporting plates are considered directly discharged on the uprights. Since multiple settings have been considered in the linear bearings' force computation, it is necessary to identify the worst-case scenario to be used in the optimization process. Even if it is not a real configuration, a combination of forces is imposed to the uprights to be conservative in the plate design. Indeed, the worst-case scenario for the frontal bearings' supporting plate is represented by the case 3, where the actuator is considered fully extended and the frontal bearings blocked, while the worst-case scenario for the rear plate is represented by case 1 where the actuator is considered fully extended and the rear bearings as blocked. Then, the forces and momentums computed in the case 3 are imposed to the frontal plate's seat obtained in the upright and the case 1 forces and momentum are imposed to the rear plate's seat. Then, the 20 mm thick region positioned all around the external edges is set as "maintained region" so that the optimizing process does not modify the global shape of the plate and the lower face is imposed as constrained. Then the mesh is generated, and the optimized plate's shape computed. The following image shows the result:

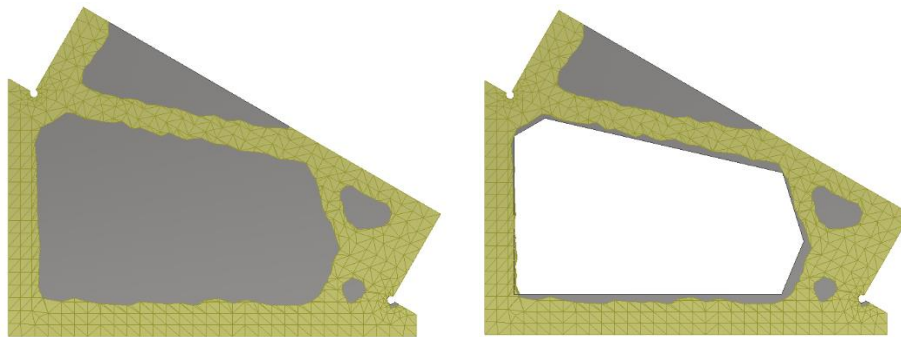


Figure 5.50: On the left the starting non-optimized geometry in grey with the optimized geometry overlapped in yellow. On the right the final geometry based on the optimized one.

Once the uprights global shape is defined, it is possible to perform a FEM analysis on the component to compute the deformation of the structure when subjected to the previously described forces.

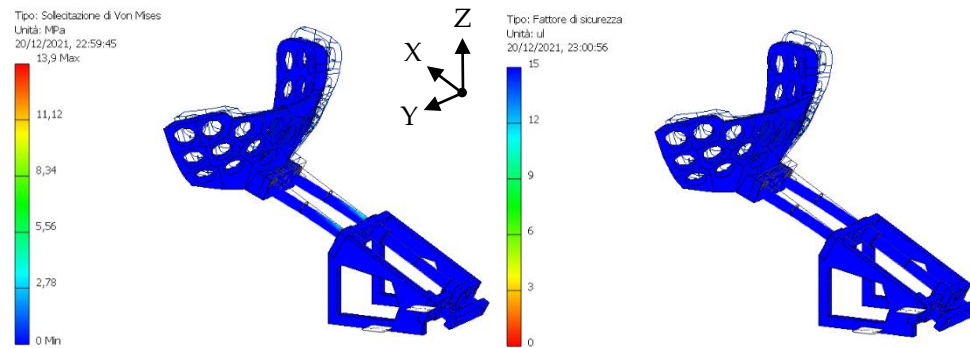
1) Constraints:

As constraint are selected the inferior face of the upright since it is bolted to the upper Stewart platform's plate.

2) Forces:

The same combination of forces considered in the optimizing process is used in the FEM analysis.

3) Results:



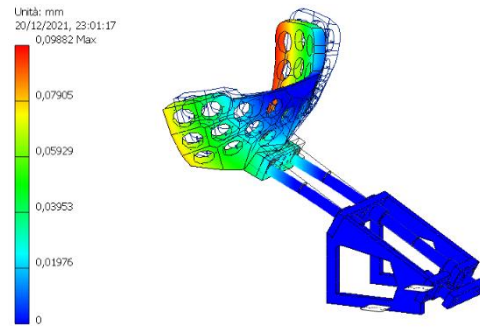
a) Von Mises stresses

b) Safety factor



c) X displacement

d) Y displacement



e) Z displacement

The connection of the two bearings supporting plates by means of the two vertical uprights increase the rigidity of the automation structure. However, since the most loaded elements of the system are the two cylindrical guides, this last FEM analysis is aligned with respect to the one performed in chapter 5.2.9 where the two vertical uprights were not considered yet in the computation. Then, the same considerations on the obtained results done in chapter 5.2.9 are valid for the latter analysis.

5.2.12 Vertical uprights' connecting bolts

The two vertical uprights are connected to the upper Stewart platform's plate by means of four M10x1,5 mm ISO 4762 bolts. Since no forces are acting in X and Y directions the connecting bolts are subjected to axial force only. The computation of the axial force is done by following the same procedure described in paragraph 5.2.2 (section 1). In this case, the vertical edges of the two uprights facing the detectors' shell are considered as hinges and the momentum producing the axial forces is generated by the displacement in X direction of the whole overlying structure's barycenter with respect to the uprights' middle axis (the momentum generated by the displacement of the barycenter in Y direction is negligible) (figure 5.51).

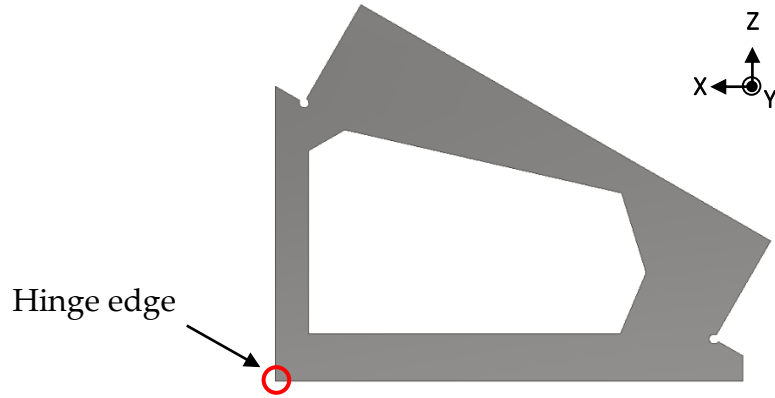
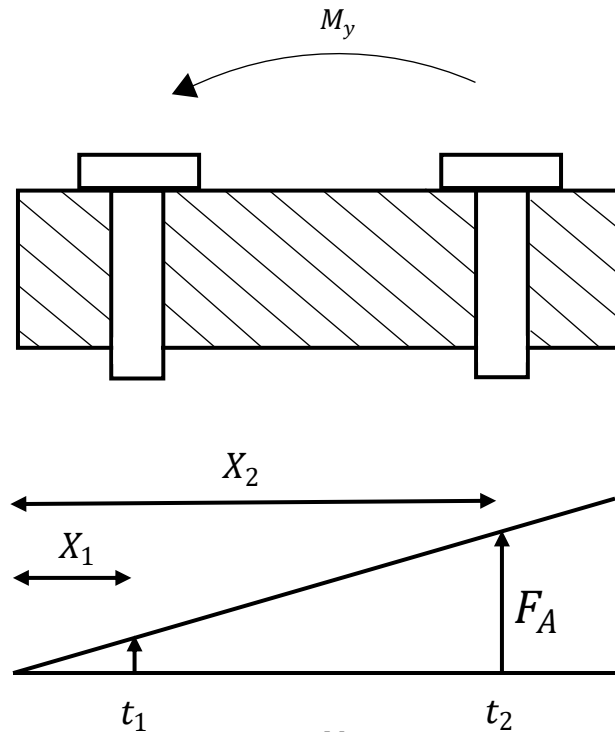


Figure 5.51: Lateral view of the vertical upright with the “hinge edge” circled in red.

As already said, the entity of the axial force acting on the bolts is directly proportional to the distance of the bolts from the hinge, then, considering the following scheme:



the generic axial force t_i is expressed as:

$$t_i = F_A * \frac{x_i}{x_n}$$

with:

F_A : axial force acting on the most stressed bolt

x_i : distance of the i-th bolt from the hinge

x_n : distance of the furthest bolt from the hinge

Since the axial force is unknown it is possible to express it as function of the known moment M_y considering the following relations:

$$M_y = 2 * \left(F_A * x_n + F_A * \frac{x_{n-1}}{x_n} + \dots + F_A * \frac{x_1}{x_n} \right)$$

from which it is possible to derive the value of the axial force F_A as:

$$F_A = \frac{M_y * x_n}{2 * (x_n^2 + x_{n-1}^2 + \dots + x_1^2)}$$

Then, since the geometry of the uprights is known, it is possible to compute the axial forces acting on each bolt (figure 5.52).

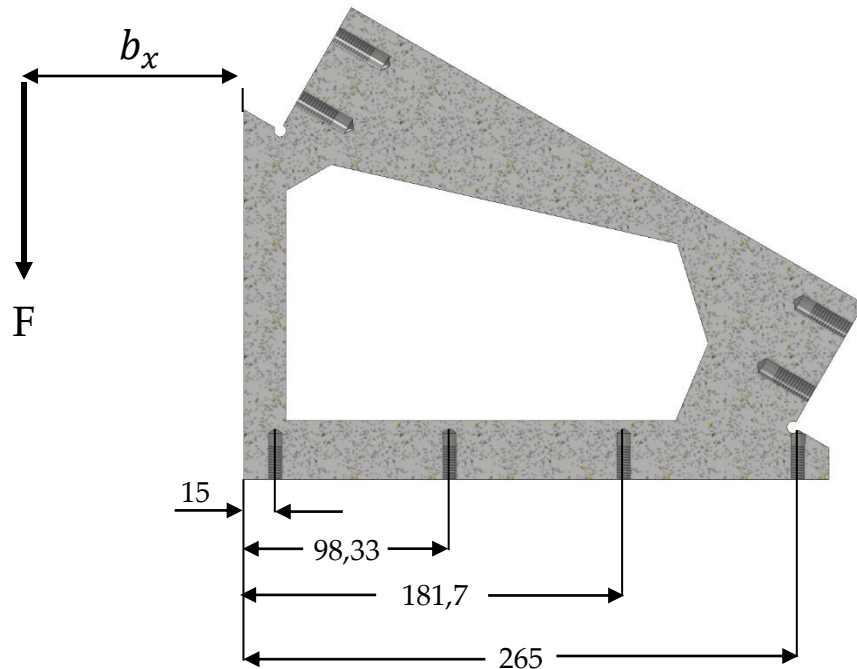


Figure 5.52: Dimensioned lateral section of the vertical upright.

Data:

- $m = 50,45 \text{ kg}$ (weight of the overlying structure)
- $F = m * g = 494,91 \text{ N}$
- $b_x = 205,30 \text{ mm}$
- $M_y = F * b_x = 101605,02 \text{ Nmm}$
- $x_1 = 15 \text{ mm}$
- $x_2 = 98,33 \text{ mm}$
- $x_3 = 181,67 \text{ mm}$
- $x_4 = 265 \text{ mm}$

Computations:

$$F_A = \frac{M_y * x_4}{2 * (x_4^2 + x_3^2 + x_2^2 + x_1^2)} = 119 \text{ N}$$

$$t_1 = F_A * \frac{x_1}{x_4} = 6,74 \text{ N}$$

$$t_2 = F_A * \frac{x_2}{x_4} = 44,16 \text{ N}$$

$$t_3 = F_A * \frac{x_3}{x_4} = 81,58 \text{ N}$$

$$t_4 = F_A * \frac{x_4}{x_4} = F_A = 119 \text{ N}$$

The value of the maximum axial force t_4 acting on the most stressed bolt is inserted in the bolt sizing Inventor's environment and the dimension of the smallest bolt able to sustain the given axial force has been computed. Here are reported the results of the analysis:

Carichi

| | | |
|---------------------------|----------------|---------|
| Fattore di tenuta | k | 1,50 su |
| Forza assiale massima | F _a | 118 N |
| Fattore input forza | n | 0,50 su |
| Forza tangente massima | F _t | 0 N |
| Fattore di attrito giunto | f | 0,40 su |

Bullone

| | | |
|-----------------------------------|------------------|------------------|
| Numero bulloni | z | 1 su |
| Diametro filettatura | d | 4,000 mm |
| Passo filettatura | p | 1,500 mm |
| Diametro bullone medio | d _s | 3,026 mm |
| Diametro minimo bullone | d _{min} | 2,160 mm |
| Materiale | | Materiale utente |
| Resistenza allo snervamento | S _y | 689 MPa |
| Fattore di sicurezza richiesto | k _s | 3,00 su |
| Pressione filettatura ammissibile | p _a | 40 MPa |
| Modulo di elasticità | E | 206700 MPa |
| Fattore di attrito filettatura | f ₁ | 0,20 su |
| Fattore di attrito testa | f ₂ | 0,25 su |

Materiale

| | | |
|-----------------------------|---|------------|
| Larghezza funzionale giunto | L | 22,000 mm |
| Modulo di elasticità | E | 206700 MPa |

Risultati

| | | |
|------------------------------------|------------------|-------------|
| Forza di precarico | F _v | 169,231 N |
| Forza operativa | F _{max} | 177,315 N |
| Momento serrante richiesto | M _u | 0,223 N m |
| Sollecitazione di trazione | σ _t | 46,196 MPa |
| Sollecitazione torsionale | τ _k | 112,909 MPa |
| Sollecitazione ridotta | σ _{red} | 200,946 MPa |
| Sollecitazione dalla forza massima | σ _{max} | 48,403 MPa |
| Pressione filettatura | p _c | 10,221 MPa |
| Verifica resistenza | | Positiva |

For a 118 N forces is sufficient a M4x1,5 mm bolt which is much smaller than the M10x1,5 mm bolts selected. The threaded connection is the sufficiently strong and ensure a high safety factor to the mounting.

5.2.13 Stewart platform

The general functioning of a Stewart platform and the solution of its inverse kinematic is described in chapter 5.1, here will be described the physical hexapod used in the NUMEN experiment.

The Stewart platform is the most critical component of the entire structure. It is responsible for both the support and the fine positioning of the detectors' sustaining shell in the correct place. Since it is required a high level of precision and repeatability, the design and the certification of this structure is outsourced to an external manufacturer specialized in the construction of micro-screw jacks (figure 5.53).

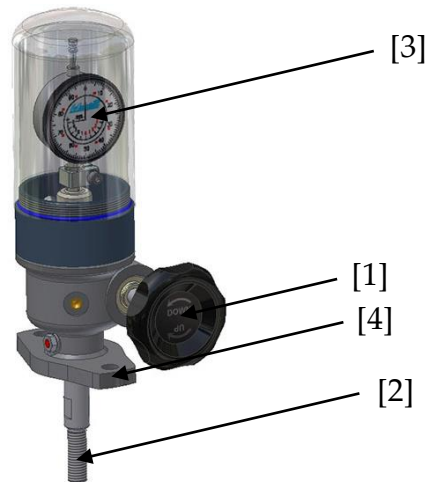


Figure 5.53: Render of a Weingrill micro-screw jack. Acting manually on the black knob [1] it is possible to set the length of the rod [2]. The length feedback is readable thanks to the analogic display [3]. The flange [4] allows to fix the body on a structure.

A modified version of the micro-screw jack represented in figure 5.53 is used in the design here represented. It is designed by the Italian manufacturer Weingrill SRL¹⁹ according to all the design requirements imposed by the mathematical model.

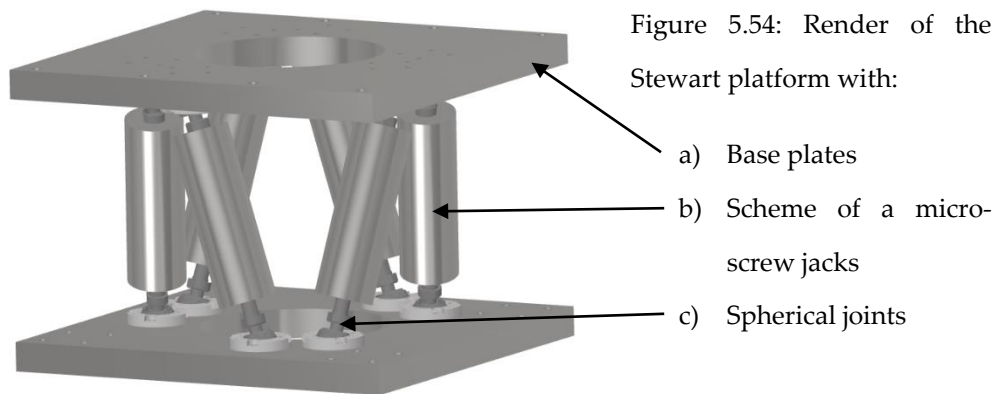
In particular, the following boundary conditions are given to the manufacturer to obtain a working structure:

- a) All the six jacks must be able to withstand a 450 N axial compression force and a 250 N axial tensile force. These values are obtained from a Matlab script described later which consider both the geometry of the Stewart platform and the forces acting on the upper moving plate of the hexapod.
- b) The regulation range of each jack must be equal or higher than ± 5 mm with a maximum positioning error equal to $1\ \mu\text{m}$. These values are

¹⁹ Weingrill SRL, San Secondo Di Pinerolo, 10060 (To)

obtained by solving the inverse kinematic of the physical platform with imposed geometries and by guaranteeing a regulation range on the end effector equal to ± 1 mm along the three main directions X, Y and Z and 1° in zenithal and azimuthal angular directions. Doing so, the possible positioning error of the shell due to the bending of the system computed with the FEM analysis can be corrected by the Stewart platform.

- c) All the materials used for both the micro-screw jacks and the spherical joints used to connect the jacks with the two base plates must be able to withstand high radiations and not to interfere with the gamma rays emitted by the nuclear reactions.
- d) Each jack must have a mechanical stopper able to block the stroke of the thread once the correct length is set.
- e) The length variation of each jack must be detected by a linear transducer and communicated to the data acquisition system.
- f) The maximum dimension of each jack must be enclosed by an imaginary cylinder with a base diameter of 40 mm and a height of 120 mm (figure 5.54).



These values are imposed so that, considering the geometry of the two base plates described later, during the regulation phase the micro-screw jacks does not enter in collision one with the other.

- g) The two ends of the jacks shall be arranged to be connected to the spherical joints, described later, by means of a thread.
- h) The micro-screw jacks must be designed to work without lubricant to avoid the contamination of the maintenance personnel with activated materials.

All this information are provided to the manufacturer who confirm the construction feasibility of the jacks.

These components are then connected both to the base and the moving plate by means of twelve spherical joints. Even in this case commercial joints are used to guarantee a high level of precision. They are selected from the Hephaist Seiko²⁰ catalog, and they are specifically designed to be used into parallel robot applications²¹. The SRJ joint is selected for the application (figure 5.55).

Figure 5.55: SRJ joints
produced by Hephaist



²⁰ Hephaist Seiko Co., LDT, Japan

²¹ Myostat motion control INC , "SRJ brochure_19", Canada, 2019

The correct sphere diameter is selected considering the data sheet of the spherical joints (figure 5.56). The bigger the sphere the higher the permissive loads and the bigger the joints itself. Since the axial compressive and tensile forces are known, the smaller joints able to withstand such loads is selected.

TECHNICAL SPECIFICATIONS

| MODEL | BASIC LOAD RATINGS | | RECOMMENDED PERMISSIVE LOADS | | | | WEIGHT (kg) | MAXIMUM SWING ANGLE |
|---------|--------------------|--------|------------------------------|-------------|------------|--------------|----------------|---------------------|
| | C (N) | Co (N) | Compressive (N) | Tensile (N) | Radial (N) | Moment (N-m) | | |
| SRJ004C | 128 | 100 | 102 | 38.4 | 64 | 0.64 | 0.015 | ±15° |
| SRJ006C | 320 | 280 | 256 | 96 | 160 | 1.84 | 0.036 | ±30° |
| SRJ008C | 490 | 540 | 392 | 147 | 245 | 3.92 | 0.06 | ±30° |
| SRJ012C | 720 | 770 | 576 | 216 | 360 | 7.20 | 0.18 | ±30° |
| SRJ016C | 1170 | 1300 | 936 | 351 | 585 | 18.7 | 0.37 | ±30° |
| SRJ024C | 2840 | 3920 | 2272 | 852 | 1420 | 59.6 | 0.93 | ±30° |
| SRJ032C | 5800 | 8820 | 4640 | 1740 | 2900 | 174 | 2.30 | ±30° |
| SRJ048C | 10600 | 16000 | 8480 | 3180 | 5300 | 413 | 6.73 | ±30° |

C(N) basic dynamic load rating Co(N) basic static load rating

Figure 5.56: Data sheet of the SRJ joints from the “SRJ brochure_19”

The SRJ016C joints are selected for the application. They are mounted on the two base plates of the Stewart platform according to the 6-3 configuration described in chapter 5.1.1. The main geometries of the two plates are here schematized (figure 5.57):

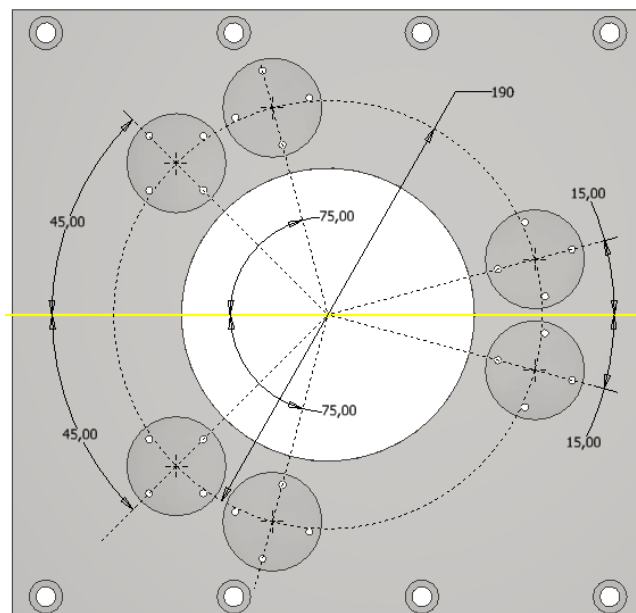


Figure 5.57: frontal view of the base plate with the six spherical joints holes geometrically dimensioned with respect to the centre of the plate.

Thanks to the use of a spherical joint, all the tangential forces acting on the system are transformed into axial forces acting on the six micro-screw jacks. This simplify the sizing of the jacks, elements which are not designed to withstand tangential loads.

The previously mentioned load acting on each jack are computed considering the weight of all the components positioned above the Stewart platform. Since the structure will work in static condition, the position of the global barycenter of such components is computed with the specific Inventor's tool (figure 5.58).

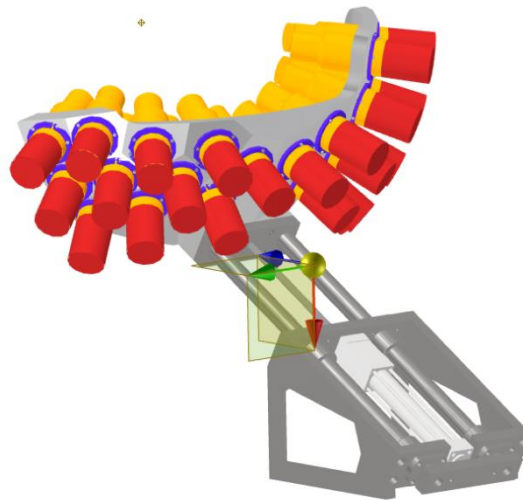
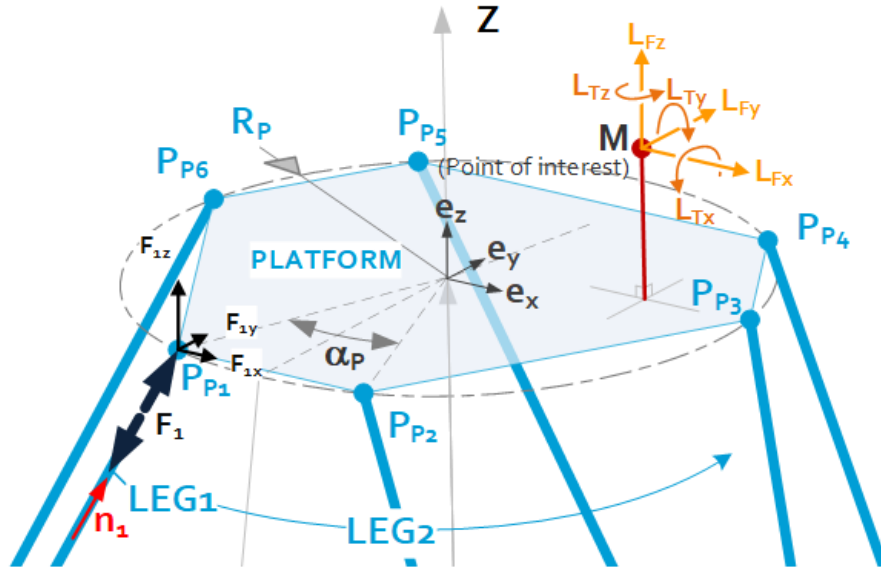


Figure 5.58: Part of the whole sustaining structure mounted above the Stewart platform with the indication of the barycentre position.

Then, a mathematical procedure is followed to compute the forces acting on the six jacks²². Starting from the definition of the hexapod geometries:

²² JPE, "Hexapod forces, engineering fundamentals", The Netherlands, 2021



- P_B, P_P : Hinge locations in the base and moving plate respectively
- R_B, R_P : Radius of pitch circle of the hinge locations in the base and moving plate respectively
- α_B, α_P : Angle between the hinge locations of a leg pair
- Z_P : Height of the moving plate with respect to the base one
- \vec{e}_i : Orthogonal unit vector, standard basis
- \vec{n}_i : Unit vector collinear with leg number i
- \vec{F}_i : Force in leg number i
- $L_{Fx, Fy, Fz}$: External force load in point M
- $L_{Tx, Ty, Tz}$: External torque load in point M

It is possible to extract the vector force \vec{F}_i to three orthogonal vectors \vec{F}_{ix} , \vec{F}_{iy} and \vec{F}_{iz} :

$$\bullet \vec{F}_{ix} = \vec{e}_x \vec{n}_i \vec{F}_i \quad \bullet \vec{F}_{iy} = \vec{e}_y \vec{n}_i \vec{F}_i \quad \bullet \vec{F}_{iz} = \vec{e}_z \vec{n}_i \vec{F}_i$$

Since the system will work in static conditions, the following equilibrium equations holds:

$$L_{Fx} + \sum_{i=1}^{i=6} \vec{e}_x \vec{n}_i \vec{F}_i = 0$$

$$L_{Fy} + \sum_{i=1}^{i=6} \vec{e}_y \vec{n}_i \vec{F}_i = 0$$

$$L_{Fz} + \sum_{i=1}^{i=6} \vec{e}_z \vec{n}_i \vec{F}_i = 0$$

$$L_{Tx} + \sum_{i=1}^{i=6} [\vec{e}_x \vec{n}_i (Z_{Pi} - Z_M) + \vec{e}_z \vec{n}_i (Y_M - Y_{Pi})] F_i = 0$$

$$L_{Ty} + \sum_{i=1}^{i=6} [\vec{e}_x \vec{n}_i (Z_M - Z_{Pi}) + \vec{e}_z \vec{n}_i (X_{Pi} - X_M)] F_i = 0$$

$$L_{Tz} + \sum_{i=1}^{i=6} [\vec{e}_x \vec{n}_i (Y_{Pi} - Y_M) + \vec{e}_y \vec{n}_i (X_M - X_{Pi})] F_i = 0$$

All these equations can be expressed in matrix notation as:

$$\begin{bmatrix} L_{Fx} \\ L_{Fy} \\ L_{Fz} \\ L_{Tx} \\ L_{Ty} \\ L_{Tz} \end{bmatrix} + \begin{bmatrix} \vec{e}_x \cdot \vec{n}_1 & \cdots & \vec{e}_x \cdot \vec{n}_6 \\ \vec{e}_y \cdot \vec{n}_1 & \cdots & \vec{e}_y \cdot \vec{n}_6 \\ \vec{e}_z \cdot \vec{n}_1 & \cdots & \vec{e}_z \cdot \vec{n}_6 \\ \vec{e}_y \cdot \vec{n}_1 \cdot -\Delta Z + \vec{e}_z \cdot \vec{n}_1 \cdot \Delta Y & \cdots & \vec{e}_y \cdot \vec{n}_6 \cdot -\Delta Z + \vec{e}_z \cdot \vec{n}_6 \cdot \Delta Y \\ \vec{e}_x \cdot \vec{n}_1 \cdot \Delta Z + \vec{e}_z \cdot \vec{n}_1 \cdot -\Delta X & \cdots & \vec{e}_x \cdot \vec{n}_6 \cdot \Delta Z + \vec{e}_z \cdot \vec{n}_6 \cdot -\Delta X \\ \vec{e}_x \cdot \vec{n}_1 \cdot -\Delta Y + \vec{e}_y \cdot \vec{n}_1 \cdot \Delta X & \cdots & \vec{e}_x \cdot \vec{n}_6 \cdot -\Delta Y + \vec{e}_y \cdot \vec{n}_6 \cdot \Delta X \end{bmatrix} \begin{bmatrix} F_1 \\ F_2 \\ F_3 \\ F_4 \\ F_5 \\ F_6 \end{bmatrix} = \vec{0}$$

and thus:

$$\begin{bmatrix} L_{Fx} \\ L_{Fy} \\ L_{Fz} \\ L_{Tx} \\ L_{Ty} \\ L_{Tz} \end{bmatrix} + T_L \cdot \begin{bmatrix} F_1 \\ F_2 \\ F_3 \\ F_4 \\ F_5 \\ F_6 \end{bmatrix} = \vec{0} \Leftrightarrow \begin{aligned} \vec{L} &= -T_L \cdot \vec{F} \\ \vec{F} &= -T_L^{-1} \cdot \vec{L} \end{aligned}$$

Since the external forces and momentum are known and the geometry of the system is defined, it is possible to compute the forces acting on each jack.

A Matlab script is coded to perform this computation:

```

r1=190/2; %radius of the base frame
r2=190/2; %radius of the moving frame
l1=590;
l3=300;
htot=935;
h1=106;
h2=21+15+280*tand(30)-140*tand(30)+34/cosd(30);
H=htot-h1-h2-(l1+l3)*tand(30); %height of the Stewart platform
gamma=15;

nAA1=[r2*cosd(60-gamma)-r1*cosd(gamma) r2*sind(60-gamma)-
r1*sind(gamma) H]';
nBB1=[r2*cosd(60+gamma)+r1*sind(30-gamma) r2*sind(60+gamma)-
r1*cosd(30-gamma) H]';
nCC1=[-r2*cosd(gamma)+r1*sind(30+gamma) r2*sind(gamma)-
r1*cosd(30+gamma) H]';
nDD1=[-r2*cosd(gamma)+r1*sind(30+gamma) -
r2*sind(gamma)+r1*cosd(30+gamma) H]';
nEE1=[r2*cosd(60+gamma)+r1*sind(30-gamma) -
r2*sind(60+gamma)+r1*cosd(30-gamma) H]';
nFF1=[r2*cosd(60-gamma)-r1*cosd(gamma) -r2*sind(60-
gamma)+r1*sind(gamma) H]';

n1=nAA1/norm(nAA1);
n2=nBB1/norm(nBB1);
n3=nCC1/norm(nCC1);
n4=nDD1/norm(nDD1);
n5=nEE1/norm(nEE1);
n6=nFF1/norm(nFF1);

ex=[1 0 0];
ey=[0 1 0];
ez=[0 0 1];

XM=173.984;

```

```

YM=-14.546;
ZM=261.357+21+H;

XP=[r2*cosd(60-gamma) r2*cosd(60+gamma) -r2*cosd(gamma) -
r2*cosd(gamma) r2*cosd(60+gamma) r2*cosd(60-gamma)]';
YP=[r2*sind(60-gamma) r2*sind(60+gamma) r2*sind(gamma) -
r2*sind(gamma) -r2*sind(60+gamma) -r2*sind(60-gamma)]';
ZP=[H H H H H H]';

TL=[ex*n1 ex*n2 ex*n3 ex*n4 ex*n5 ex*n6;...
    ey*n1 ey*n2 ey*n3 ey*n4 ey*n5 ey*n6;...
    ez*n1 ez*n2 ez*n3 ez*n4 ez*n5 ez*n6;...
    ey*n1*(-ZM+ZP(1))+ez*n1*(YM-YP(1)) ey*n2*(-
ZM+ZP(2))+ez*n2*(YM-YP(2)) ey*n3*(-ZM+ZP(3))+ez*n3*(YM-YP(3))
ey*n4*(-ZM+ZP(4))+ez*n4*(YM-YP(4)) ey*n5*(-ZM+ZP(5))+ez*n5*(YM-
YP(5)) ey*n6*(-ZM+ZP(6))+ez*n6*(YM-YP(6));...
    ex*n1*(ZM-ZP(1))+ez*n1*(-XM+XP(1)) ex*n2*(ZM-ZP(2))+ez*n2*(-
XM+XP(2)) ex*n3*(ZM-ZP(3))+ez*n3*(-XM+XP(3)) ex*n4*(ZM-
ZP(4))+ez*n4*(-XM+XP(4)) ex*n5*(ZM-ZP(5))+ez*n5*(-XM+XP(5))
ex*n6*(ZM-ZP(6))+ez*n6*(-XM+XP(6));...
    ex*n1*(-YM+YP(1))+ey*n1*(XM-XP(1)) ex*n2*(-
YM+YP(2))+ey*n2*(XM-XP(2)) ex*n3*(-YM+YP(3))+ey*n3*(XM-XP(3))
ex*n4*(-YM+YP(4))+ey*n4*(XM-XP(4)) ex*n5*(-YM+YP(5))+ey*n5*(XM-
XP(5)) ex*n6*(-YM+YP(6))+ey*n6*(XM-XP(6))];
L=[0 0 -59.532*9.81 0 0 0]';
F=-inv(TL)*L

```

The main results are here reported:

$$\begin{aligned}
 F_1 &= 420,3 \text{ N} & F_2 &= 69,6 \text{ N} \\
 F_3 &= -248,8 \text{ N} & F_4 &= -216,5 \text{ N} \\
 F_5 &= 134,2 \text{ N} & F_6 &= 452,6 \text{ N}
 \end{aligned}$$

The positive values refer to compressive forces and the negative values to tensile forces. As previously said, the micro-screw jacks must be able to withstand these forces to correctly sustain the automation structure.

5.2.14 Linear bearings

The whole sustaining cart composed by the Stewart platform and the automation structure is mounted on a pair of linear bearings. These elements allow the horizontal translation from the working to the maintenance position of the detectors' supporting shell. Each linear bearing is composed by a rail on which cursors are mounted (figure 5. 59).

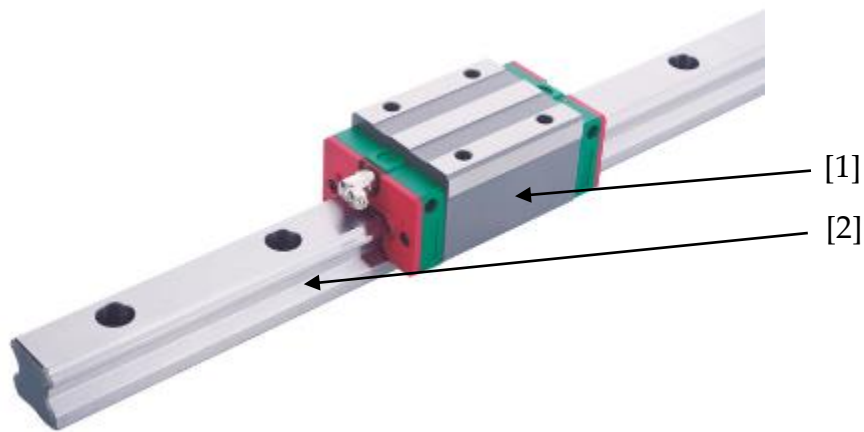
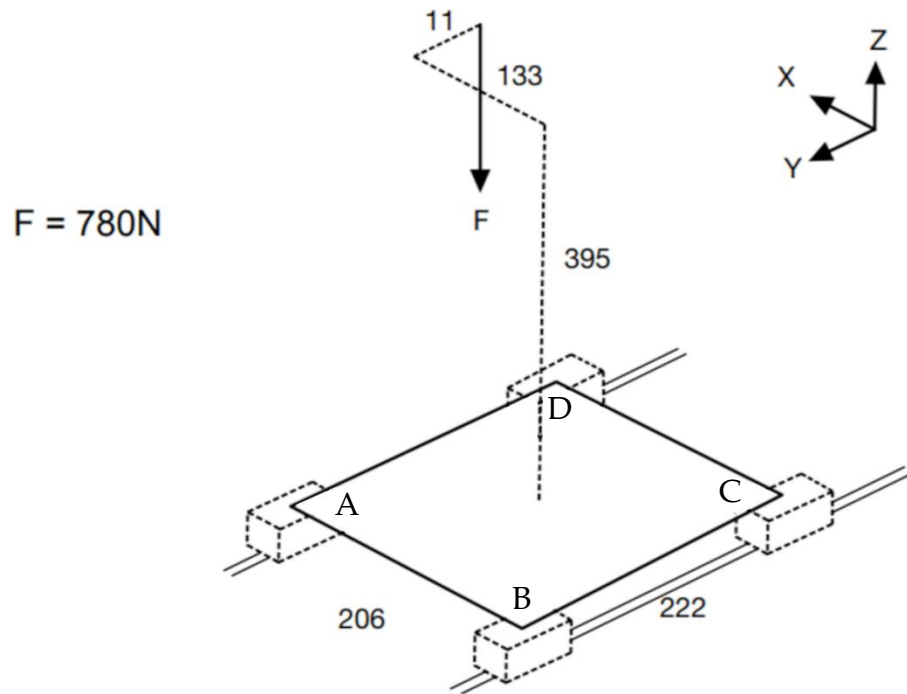


Figure 5.59: Render of a commercial linear bearing. [1] rail, [2] cursor.

Several types of linear bearing are available on the market. They differ from each other in the shape of the recirculating elements. To select the correct bearing for the NUMEN application the computation of all the forces acting on each cursor is done. The guides' system is considered as composed by 2 parallel rails, each of them carrying two cursors. The cursors are directly bolted to the Stewart platform base plate and the two rails are bolted to the sustaining structure's basement. Before computing the forces acting on the cursor, the geometry of the bearing system is defined. The distance between the two rails and the distance between the two cursors mounted on the same rail is imposed by considering both the global geometry of the system described in chapter 5.2.4 (figure 5.31) and the dimensions

of the Stewart platform base plate. The final arrangement is represented in the following scheme:



From this scheme it is possible to notice that the concentrated weight force of the structure mounted above the linear bearings is displaced with respect to the center of the Stewart platform base plate. This generate both a compressive force on the four cursor and a momentum on the base plate which produce a tensile force on the cursors due to the hinge effect described in chapter 5.2.2.

It is then necessary to consider the superposition of effects in the computation of the forces acting on each cursor.

To simplify the computation, the Stewart platform base plate is considered as a hyperstatic beam with both clamped ends (figure 5.60).

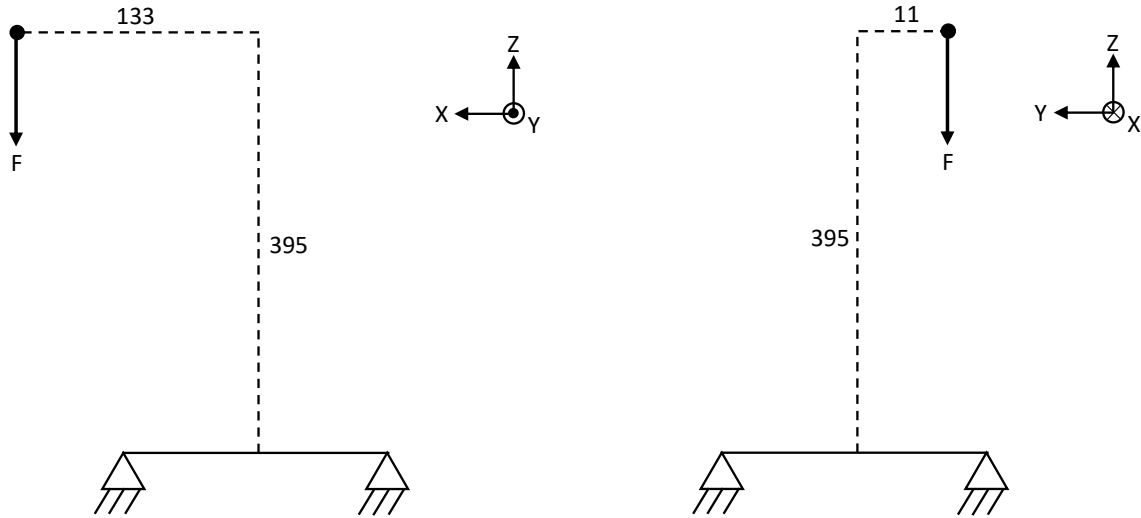
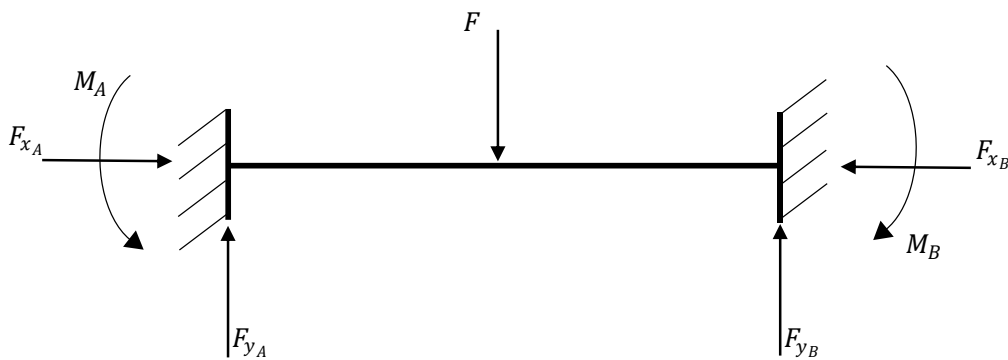


Figure 5.60: Schematic representation of the Stewart platform base plate considered as a hyperstatic beam clamped on both ends in correspondence of the linear guides cursors.

The two views are analyzed singularly using the same method adopted for the computation of the forces acting on the cylindrical bearings of the automation structure. Since in a hyperstatic structure the number of equations is lower than the number of unknowns, it is then necessary to add to the linear system of equations two extra “congruence equations”.

1) Hyperstatic beam with both clamped ends and center load



Considering the above scheme, the following equations holds in static conditions:

$$\sum F_x = 0 \rightarrow F_{x_A} - F_{x_B} = 0$$

$$\sum F_y = 0 \rightarrow F_{y_A} + F_{y_B} - F = 0$$

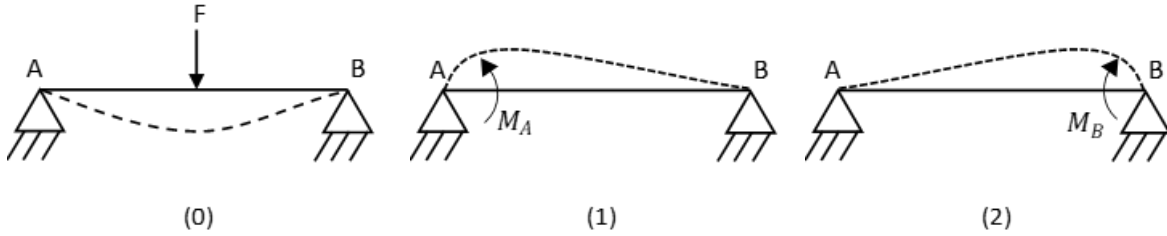
$$\sum M_A = 0 \rightarrow -M_A + F * \frac{l}{2} - F_{y_B} * l + M_B = 0$$

To solve the linear system two more congruence equations must be added:

$$\varphi_A = 0 \rightarrow \text{Null displacement of the clamped end A}$$

$$\varphi_B = 0 \rightarrow \text{Null displacement of the clamped end B}$$

The displacement of the two end is caused by the superposition of three different effects:



$$\varphi_A = \varphi_A^{(0)} + \varphi_A^{(1)} + \varphi_A^{(2)} = \frac{Fl^2}{16EI} - \frac{M_A l}{3EI} - \frac{M_B l}{6EI} = 0$$

$$\varphi_B = \varphi_B^{(0)} + \varphi_B^{(1)} + \varphi_B^{(2)} = -\frac{Fl^2}{16EI} + \frac{M_A l}{6EI} + \frac{M_B l}{3EI} = 0$$

All these formulas are taken from the literature.

Since the structure is symmetric, the modulus of the two torques are equal:

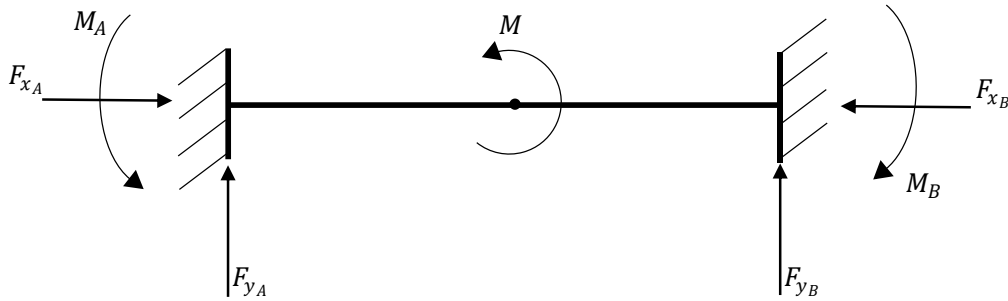
$$|M_A| = |M_B| \rightarrow M_A = M_B$$

The above equations can be simplified as:

$$\frac{Fl}{16} - \frac{M_A}{3} - \frac{M_A}{6} = 0 \rightarrow M_A = \frac{Fl}{8} = M_B$$

$$-M_A + F * \frac{l}{2} - F_{yB} * l + M_B = 0 \rightarrow F_{yB} = \frac{F}{2} = F_{yA}$$

2) Hyperstatic beam with both clamped ends and center torque



Considering the above scheme, the following equations holds in static conditions:

$$\sum F_x = 0 \rightarrow F_{xA} - F_{xB} = 0$$

$$\sum F_y = 0 \rightarrow F_{yA} + F_{yB} = 0$$

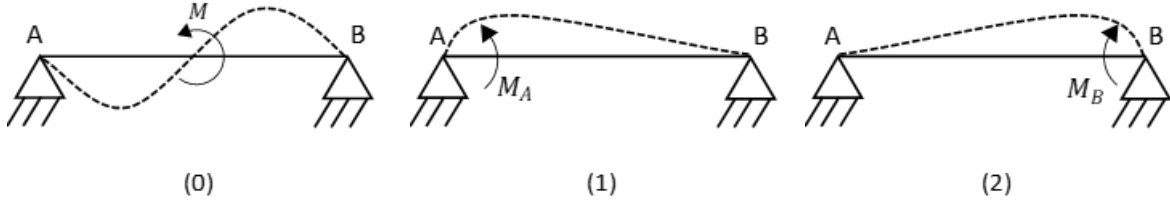
$$\sum M_A = 0 \rightarrow -M_A - M - F_{yB} * l + M_B = 0$$

To solve the linear system two more congruence equations must be added:

$$\varphi_A = 0 \rightarrow \text{Null displacement of the clamped end A}$$

$$\varphi_B = 0 \rightarrow \text{Null displacement of the clamped end B}$$

The displacement of the two end is caused by the superposition of three different effects:



$$\varphi_A = \varphi_A^{(0)} + \varphi_A^{(1)} + \varphi_A^{(2)} = \frac{Ml}{24EI} - \frac{M_A l}{3EI} - \frac{M_B l}{6EI} = 0$$

$$\varphi_B = \varphi_B^{(0)} + \varphi_B^{(1)} + \varphi_B^{(2)} = \frac{Ml}{24EI} + \frac{M_A l}{6EI} + \frac{M_B l}{3EI} = 0$$

All these formulas are taken from the literature.

The above equations can be simplified as:

$$\frac{M}{8} - M_A - \frac{M_B}{2} = 0 \rightarrow M_A = \frac{M}{8} - \frac{M_B}{2}$$

$$\frac{M}{8} + \frac{M}{16} - \frac{M_B}{4} + M_B = 0 \rightarrow M_B = -\frac{1}{4}M$$

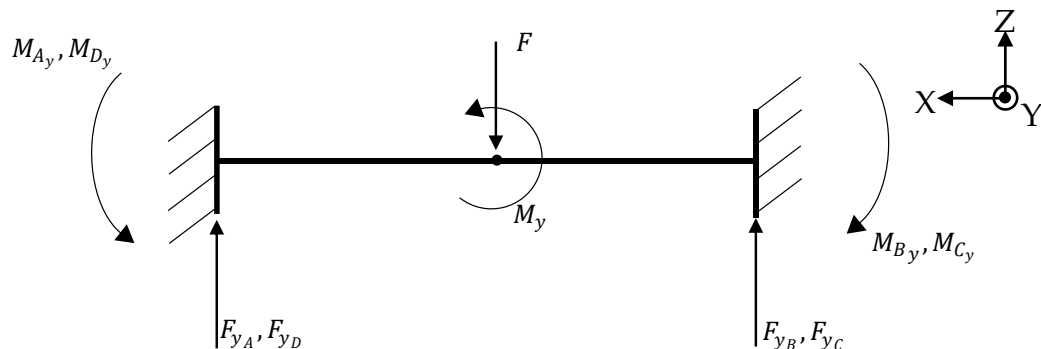
$$-M_A - M - F_{yB} * l + M_B = 0 \rightarrow F_{yB} = -\frac{3}{2}\frac{M}{l}$$

$$F_{yA} + F_{yB} = 0 \rightarrow F_{yA} = \frac{3}{2}\frac{M}{l}$$

The general equations must then be applied to the real structure.

Considering one plane at a time:

a) XZ plane



$$F_{y_A}(F) = F_{y_D}(F) = \frac{1}{2}F = \frac{F}{4}$$

$$F_{y_B}(M_y) = F_{y_C}(M_y) = -\frac{1}{2}\left(\frac{3}{2}\frac{M_y}{l}\right)$$

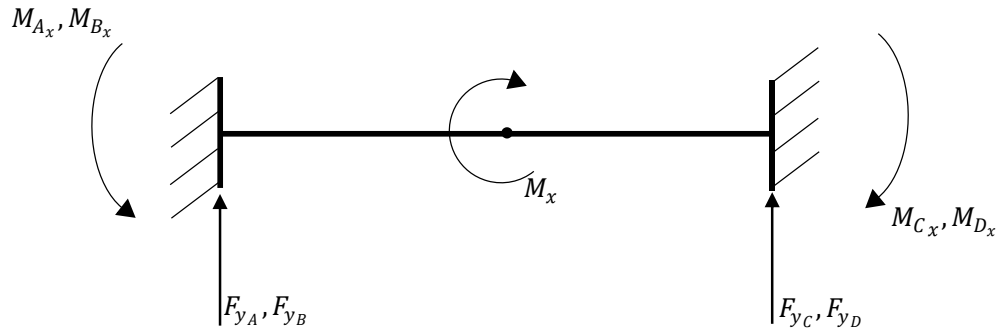
$$F_{y_B}(F) = F_{y_C}(F) = \frac{1}{2}F = \frac{F}{4}$$

$$M_{A_y}(M_y) = M_{D_y}(M_y) = \frac{1}{2}\left(\frac{M_y}{4}\right)$$

$$F_{y_A}(M_y) = F_{y_D}(M_y) = \frac{1}{2}\left(\frac{3}{2}\frac{M_y}{l}\right)$$

$$M_{B_y}(M_y) = M_{C_y}(M_y) = -\frac{1}{2}\left(\frac{M_y}{4}\right)$$

b) YZ plane



$$F_{y_A}(M_x) = F_{y_B}(M_x) = -\frac{1}{2}\left(\frac{3}{2}\frac{M_x}{l}\right)$$

$$M_{A_x}(M_x) = M_{B_x}(M_x) = -\frac{1}{2}\left(\frac{M_x}{4}\right)$$

$$F_{y_C}(M_x) = F_{y_D}(M_x) = \frac{1}{2}\left(\frac{3}{2}\frac{M_x}{l}\right)$$

$$M_{C_x}(M_x) = M_{D_x}(M_x) = \frac{1}{2}\left(\frac{M_x}{4}\right)$$

Then, knowing the entity of the force $F = 776,2 \text{ N}$ obtained with the Inventor tool it is possible to compute the values of the reaction forces of each of the four linear bearings cursors:

$$F_{y_A} = F_{y_A}(F) + F_{y_A}(M_y) + F_{y_A}(M_x)$$

$$F_{y_C} = F_{y_C}(F) + F_{y_C}(M_y) + F_{y_C}(M_x)$$

$$F_{y_B} = F_{y_B}(F) + F_{y_B}(M_y) + F_{y_B}(M_x)$$

$$F_{y_D} = F_{y_D}(F) + F_{y_D}(M_y) + F_{y_D}(M_x)$$

$$M_{A_y} = M_{D_y}$$

$$M_{A_x} = M_{B_x}$$

$$M_{B_y} = M_{C_y}$$

$$M_{C_x} = M_{D_x}$$

The computed forces have been communicated to the linear bearings manufacturer who recommended the HGH25CA 2R1035EZAHI ball bearings of the HG series ARMOLOY-treated. This type of linear bearings can work without lubrication avoiding the risk of radiation contamination of the maintenance personnel.

5.2.15 Support frame

The whole cart composed by the linear bearings, the hexapod, the automation structure, and the detectors' supporting shell is mounted on a support frame composed by two parallel 50x50 profile steel tubing. The two are attached one with the other by means of a base plate directly bolted to the NUMEN basement (figure 5.60).

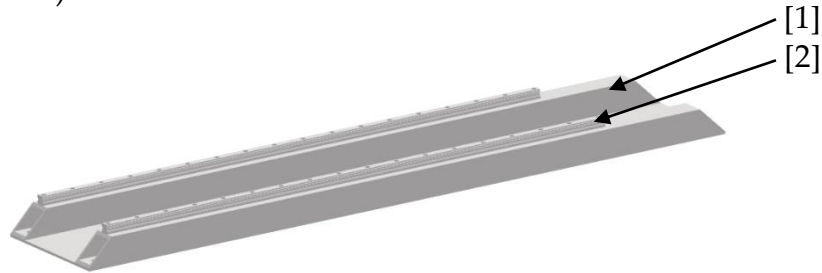


Figure 5.60: Render of the support frame [1] on which the two linear bearings' rails [2] are bolted.

Since the NUMEN's basement can vary according to some changes in the nearby components, the shape and the dimensions of the support frame can still change. The FEM analysis is then not be done on this last component.

The support frame, in addition to the task of supporting the structure, also has the task of allowing the positioning of the cable chain below the Stewart platform (figure 5.61). Indeed, thanks to the void produced by the rise of the linear

bearings with respect to the NUMEN basement, it is possible to install the cable chain responsible for the correct movement of the power and signal cables coming from the data acquisition system under the Stewart platform. This reduces the global size of the system and speed up the disassembly procedure allowing to remove the cable chain together with the support frame.

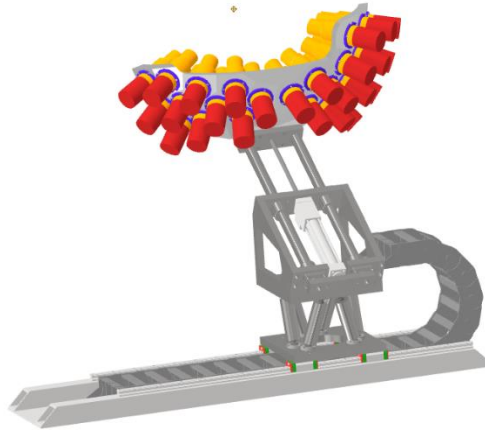


Figure 5.61: Render of the whole supporting structure with the cable chain.

The selected cable chain is the E300_3_45_150_0 by Igus²³ and it is dimensioned with the specific tool to contain all the fifty $\phi 5$ mm cables coming from the detectors and the pneumatic line needed by the actuator (figure 5.62).

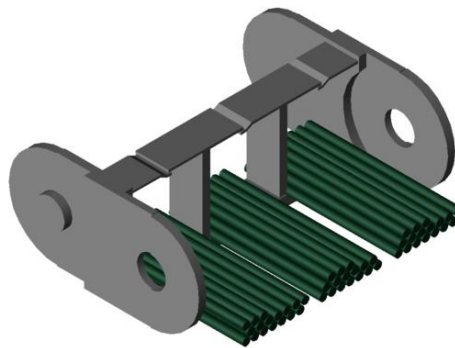


Figure 5.62: Render of one section of the E300_3_45_150_0 cable chain with the fifty $\phi 5$ mm positioned in the working position.

²³ IGUS, inc., 257 Ferris Avenue, Rumford, RI, United States

Moreover, since the horizontal translation of the cart is performed manually, two threaded end stops are mounted on the profile tubing to correctly position the cart in the Y direction (figure 5.63).

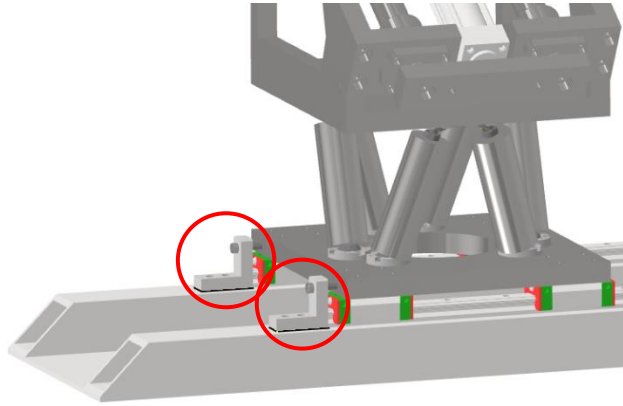


Figure 5.63: Detail of the sustain structure with the two end stops circled in red.

Once the cart is moved to the working position and the two end stops are set, a pair of manual clamps mounted behind the Stewart platform block the structure in place. A pair of HK2501A Zimmer manual clamp is used for the application (figure 5.64). They are specifically designed for the used linear bearings' rails and develop a holding force up to 1200 N.

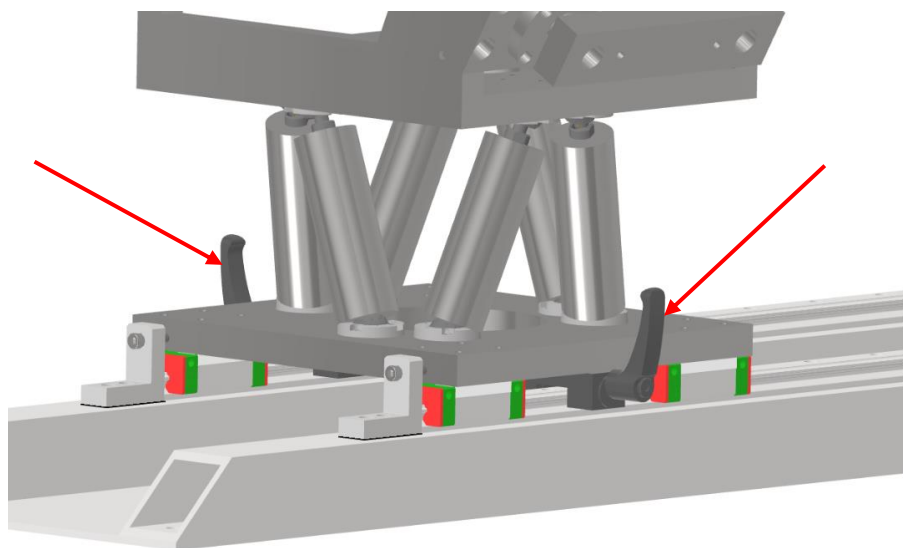


Figure 5.64: Detail of the sustain structure with the two manual clamps pointed by two arrows.

5.2.16 Patch panels

Since the maintenance of each detector will be performed mainly singularly, it is required to easily detach the signal and the power cables coming from the 25 detectors from the data acquisition system. These cables are responsible for both the transmission of the data registered by the detectors towards the data acquisition system and the power of the detectors which allows them to operate properly. To speeding up the maintenance, two patch panels are installed on the lateral sides of the vertical uprights of the automation structure (figure 5.65).

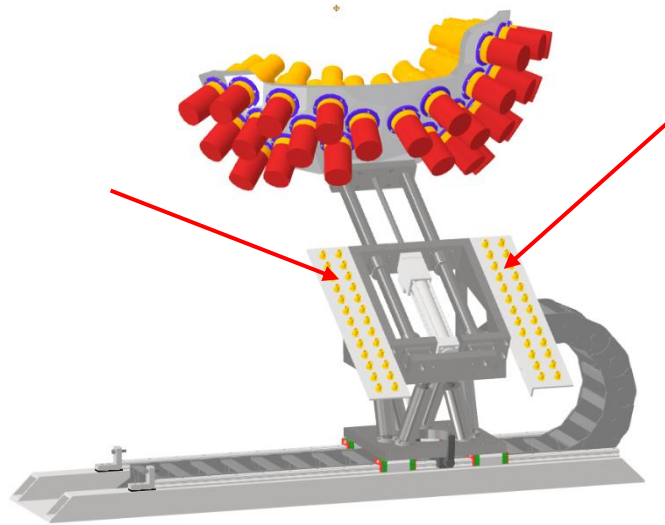


Figure 5.65: Representation of the whole sustain structure with the two patch panels bolted to the sides of the automation structure.

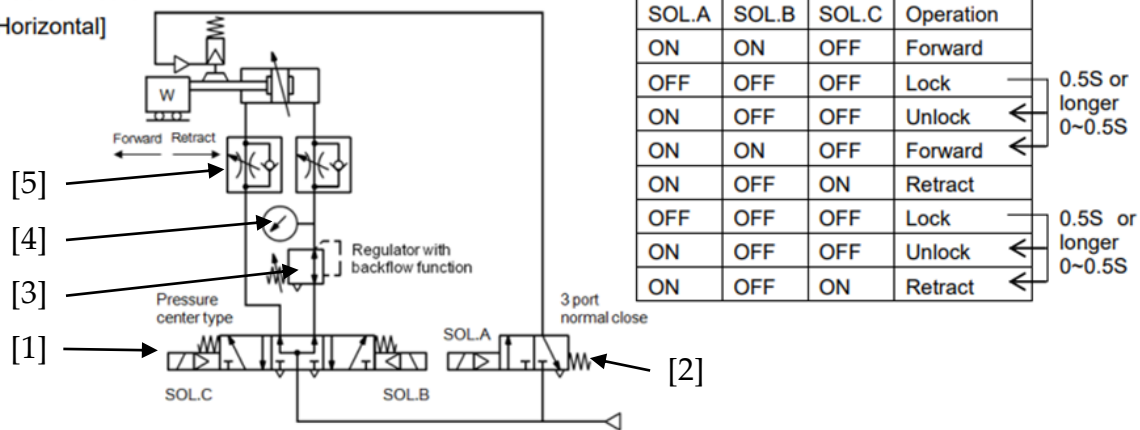
The proposed patch panels are composed by a 4 mm thick metallic plate on which 26 BNC connectors are mounted. The BNC connector allows to connect the cables coming from the detector on one side and the cables coming from the data acquisition system from the other side. They can be manually disconnected to isolate the detectors from the system to perform the maintenance.

5.3 Control system

The semi-automatic positioning structure described in chapter 5.2 requires a control system to manage the shell handling sequence. Indeed, the MWBB32-160 pneumatic cylinder needs two synchronized valves for the extension/retraction phase and the block of the stem. The pneumatic scheme of the control system is taken from the actuator catalog, and it's here reported:

⑦ Basic Circuit

1. [Horizontal]



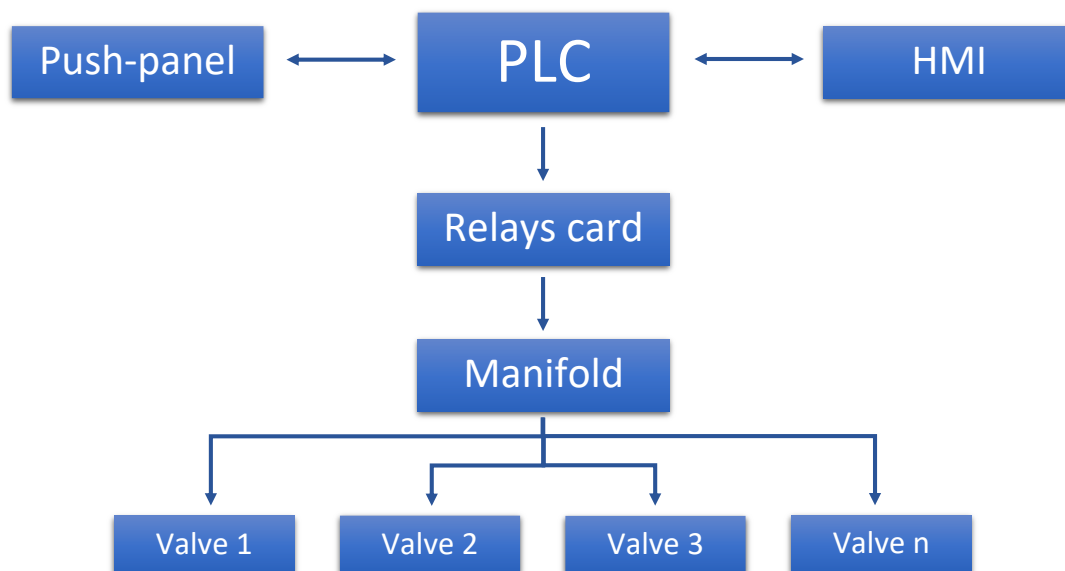
It is composed by a 5/3 normally open solenoid valve [1], a 3/2 normally closed solenoid valve with returning spring [2], a pressure regulator with backflow function [3], a barometer [4] and two speed controllers [5]. The whole system is fed by a 6-bar inlet pressure which allows the actuator to properly work. As can be seen from the table on the right side of the scheme, it is necessary to control the sequence of activation of the three solenoids to obtain the correct functioning of the system. First, the pneumatic block must be disengaged powering the solenoid A. Only after this phase it is possible to act on the solenoid B to obtain the extension of the actuator, or on solenoid C to obtain the retraction of the stem. The lock of the system is obtained de-energizing solenoid A.

To manage the sequence of valves' activations a central PLC controller is installed in the system. It directly commands a 24V DC relays card which sends

electrical signal to the pneumatic valves via a D-sub cable. This configuration allows to easily substitute the relays card in case of malfunctioning and isolate the PLC from the valves.

All the described electrical elements are mounted on a DIN guide inside an electrical cabinet and can be controlled both on-site, by means of a push-panel positioned on the cabinet itself, or remotely thanks to a Human Machine Interface mounted in the control room out from the NUMEN experimental hall.

The whole control system can then be schematized as:



Since multiple valves must be controlled simultaneously, they are all mounted in a rack configuration thanks to a pneumatic manifold.

To obtain a better price quote of the whole structure a control system based on the use of SMC valves of the JSY1000 series²⁴ is hypnotized (figure 5.66). These valves are specifically studied for the MWBW pneumatic actuators and can be mounted in parallel on a DIN rail. It is then possible to command all the valves

²⁴ SMC, "Compact 5-Port Solenoid Valve", p.19

with a single D-sub cable thanks to the pneumatic manifold on which the valves are mounted on.

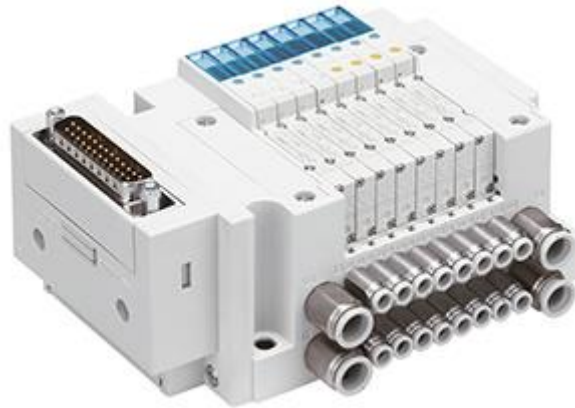


Figure 5.66: SMC JSY1000 compact 5-port solenoid valve with eight valves connected in parallel and the D-sub connector.

For the NUMEN application it is required a manifold with two valves, but to be more conservative, and to guarantee a correct functioning of the system even in case of malfunctioning, an additional valve module is considered in the price quote. The manifold is then connected via D-sub cable to a relays card composed by four SPDT CA/CC RS Pro 24 V relays mounted in a rack configuration on the DIN rail (figure 5.67).



Figure 5.67: SPDT CA/CC RS Pro 24 V relay module

The opening of the relays is commanded by the central S7-1200 CPU 1211C Siemens PLC opportunely programmed and commanded by the HMI SIMATIC KTP400 (figure 5.68).



Figure 5.68: On the left the S7-1200 CPU 1211C Siemens PLC,
on the right the HMI SIMATIC KTP400

The control of the PLC can be also analogically done acting on the buttons mounted on the lateral side of the electrical cabinet. This configuration allows technicians to move the actuator in proximity of it simplifying the maintenance procedure (figure 5.69).



Figure 5.69: Siemens 6FC5203-0AD26-0AA0 Push Button Panel

5.4 Price quote

To evaluate the construction feasibility of the third structure, a global quote which considers the costs of all the used components is done. For each component used it is indicated the description with the commercial code, the quantity used, the unit price, the total amount, and the status (P: purchased, C: custom). The prices are taken from catalogs for commercial components and from previous price quotes of similar experiments for custom components.

| Item | Description | Quantity | Status | Unit Price | Amount |
|------|---|----------|--------|------------|------------|
| 1 | Automation structure's connecting plate | 1 | C | 296,98 € | 296,98 € |
| 2 | Linear shaft - MISUMI - SSFJW30-610-M10-N10 | 2 | P | 92,73 € | 185,46 € |
| 3 | Flanged Linear Bushings - MISUMI - SLHFCS30 | 4 | P | 50,13 € | 200,52 € |
| 4 | End stops' plate | 1 | C | 211,89 € | 211,89 € |
| 5 | Cylindrical bearings' supporting plates (frontal) | 1 | C | 450,10 € | 450,10 € |
| 6 | Cylindrical bearings' supporting plates (rear) | 1 | C | 426,04 € | 426,04 € |
| 7 | Pneumatic actuator - SMC - MWBB32-160 | 1 | P | 278,12 € | 278,12 € |
| 8 | Vertical uprights | 2 | C | 547,68 € | 1.095,36 € |
| 9 | Stewart platform base plate | 2 | C | 641,23 € | 1.282,46 € |
| 10 | Sferical rolling joint - Hephaist - SRJ016C | 12 | P | 236,96 € | 2.843,52 € |
| 11 | Micro-screw jack | 6 | C | 1.000,00 € | 6.000,00 € |
| 12 | Linear bearings - Hiwin - HGH25CA 2R1035EZA | 2 | P | 167,00 € | 334,00 € |
| 13 | Support frame | 1 | C | 1.000,00 € | 1.000,00 € |
| 14 | Cable chain - Igus - E300_3_45_150_0 - | 1 | P | 68,13 € | 68,13 € |
| 15 | Manual clamp - Zimmer - HK2501A | 2 | P | 154,26 € | 308,52 € |
| 16 | Handle - MISUMI - UHFNSG120-S | 2 | P | 15,95 € | 31,90 € |
| 17 | Manifold - SMC - JJ5SY1-10F1-03D-C2D | 1 | P | 250,99 € | 250,99 € |
| 18 | Dsub cable 25 pin 20 m | 1 | P | 150,00 € | 150,00 € |
| 19 | PLC - Siemens - S7-1200 CPU 1211C | 1 | P | 385,00 € | 385,00 € |
| 20 | Relays - RS - SPDT CA/CC RS Pro 24 V | 4 | P | 55,24 € | 220,96 € |
| 21 | HMI - Siemens - SIMATIC KTP400 | 1 | P | 321,30 € | 321,30 € |
| 22 | Push-panel - Siemens - 6FC5203-0AD26-0AA0 | 1 | P | 332,00 € | 332,00 € |
| 23 | End stop - MISUMI - AJLTTS5-20 | 2 | P | 31,38 € | 62,76 € |
| 24 | Bolt - ISO 4762 - M10 x 40 | 4 | P | 0,35 € | 1,41 € |

| Item | Description | Quantity | Status | Unit Price | Amount |
|------|-------------------------------------|----------|--------|------------|----------|
| 25 | Flanged hex nut - MISUMI - FRSNUT10 | 1 | P | 1,65 € | 1,65 € |
| 26 | Bolt - ISO 4762 - M10 x 25 | 20 | P | 0,35 € | 7,00 € |
| 27 | Bolt - ISO 4762 - M6 x 12 | 16 | P | 0,04 € | 0,68 € |
| 28 | Bolt - ISO 4762 - M6 x 25 | 20 | P | 0,04 € | 0,84 € |
| 29 | Bolt - MISUMI - ANBS6-25 | 2 | P | 6,74 € | 13,48 € |
| 30 | Bolt - ISO 4762 - M5 x 16 | 36 | P | 0,03 € | 0,96 € |
| 31 | Patch panel | 2 | C | 150,00 € | 300,00 € |
| 32 | BNC connectors | 50 | P | 5,00 € | 250,00 € |

| | | |
|--------------|----------|------------------|
| Subtotal | € | 17.312,03 |
| VAT Rate | % | 22,00 |
| VAT | € | 3.808,65 |
| Total | € | 21.120,67 |

The total cost of the manual structure can then be compared with the cost of the automated Stewart platform listed in Chapter 5.1.3. It can be noticed that a manual solution has led to a much cheaper structure. If the commercial platform was used in the experiment, the total cost doubles up to 42491,99 €. The development of a completely manual structure, with all the problems associated with its set-up, is therefore justified by the large economic savings obtained.

Since the above quote is computed with estimation of the custom components, to obtain a more precise comparison, it will be necessary to update the quote as soon as the real cost of those component is known.

6 Conclusions

The work developed in this thesis allowed to better understand the design process which stands behind the construction of a critical component as the gamma detectors' supporting structure. Following each phase of the project from the definition of the boundary conditions to the elaboration of a price quote of all the components used for the supporting structure revealed how to manage each of the main phases composing the whole construction process. There have been many problems and difficulties encountered in the design; first, the identification of all the boundary conditions which impose some constraints to the system as the geometry of the structure, the resistance to radiations, the precision and the repeatability of the positioning system, the global cost, and many more. Then, one of the harder points to overcome was the definition of the structure's kinematics able to satisfy both the coarse regulation related to the translation of the whole cart and the fine regulation related to the precise positioning of the supporting shell in space. The ease of construction of the first solution has indeed been discarded because of the difficulty in solving the inverse kinematics of a serial structure, directing the study towards a more complex parallel type. Moreover, the design of a structure mostly based on the use of commercial components allowed to obtain a cheaper solution, but radically limited the design freedom. Finally, the relationship with companies specialized in prototyping mechanical components has turned out more complicated than expected because of the little appeal due to the demand for production of a very limited series of components.

To solve all these problems, it was necessary to apply many of the knowledge learned during the master's degree course in mechanical engineering. In addition, thanks to mentoring by INFN researchers, it has been possible to apply

methods experimentally developed in the design of similar systems to speed up the solution of the encountered issues.

It has then been possible to design a structure which satisfies all the requirements and the boundary conditions. Moreover, it is easy to install and remove simplifying the changing of configuration from low to high intensity tests. The positioning procedure is straightforward, and the positioning correction of the shell is simply performed acting on the length of the six platform's legs.

Even if the global functioning of the system is defined and the components have been properly sized for their application, research is still to be carried out to fully define the behaviour of the structure.

First, it is necessary to design, together with the constructor, the six micro-screw jacks which will compose the Stewart platform. Then, a tolerance chain must be calculated to better understand the global positioning precision of the system and to properly adjust the MATLAB code aligning it with the real mechanical functioning of the structure. Moreover, a failure mode and effect analysis performed on the supporting structure will prevent damage to the detectors. Finally, as the FEM analysis point out, it is possible to optimize the shape of the structure's plates since, for most of them, the mechanical safety factor is way higher than the minimum allowed. This will also lighten the structure reducing the load acting on both the Stewart platform and the linear guides leading to a higher precision of the system. At this stage it will be very important to keep under control the deformations of the system to avoid that an excessive lightening of the structure causes the generation of large deformations.

In conclusion, the structure proposed in this thesis represents only one of many solutions to the problem. Some other configurations with similar results can be developed. It is then necessary to expand the knowledge related to precision positioning structures searching for solutions which simplify both the construction and the positioning procedure. Only after careful research it will be possible to validate the structure proposed in this thesis and proceed with prototyping.

7 Bibliography

- ¹ D. Sartirana, *Sistemi automatici per la movimentazione di bersagli per esperimenti di fisica nucleare*, Torino: Politecnico di Torino, 2019.
- ² “The NUMEN Technical Design Report”, International Journal of Modern Physics A (IJMPA), Volume No. 36, Issue No. 30, Article No. 2130018.
- ³ F. Cappuzzello, C. Agodi, D. Carbone and M. Cavallaro, “The MAGNEX spectrometer: Results and perspectives”, Eur. Phys. J. A (2016) 52: 167. DOI 10.1140/epja/i2016-16167-1.
- ⁴ Cern
- ⁵ P. Cruz, R. Ferreira, J. Silva Sequeira, “Kinematic modeling of Stewart-Gough platform”, ICINCO, 2005.
- ⁶ D. Stewart, “A platform with six degrees of freedom”, Proc. Instn. Mech. Engrs. 1965.
- ⁷ J. Merlet, “Parallel Robots”, Springer Netherlands, Dordrecht, The Netherland, 2006
- ⁸ JPE, “Hexapod forces, engineering fundamentals”, The Nederalnds, 2021
- ⁹ S. Hajdu, D. Bodnar, J. Menyhart, ZS. Békési, “Kinematical simulation methods for Stewart platform in medical equipments”, Department of Mechanical Engineering, University of Debrecen, 4028 Debrecen, Ótemető, Hungary, 2017
- ¹⁰ R.V.V. Petrescu, R. Aversa, A. Apicella, M.M. Mirsayar, S. Kozaitis, T. A. Lebdeh, F.I.T. Petrescu, “Inverse Kinematics of a Stewart Platform”, Journal of Mechatronics and Robotics, 2018
- ¹¹ H. Ulbrich, L. Ginzinger, “Motion and vibration control”, Movic, 2008

8 Sitography

- ¹ *Superconducting Cyclotron*, <https://www.lns.infn.it/en/accelerators/superconducting-cyclotron.html>
- ² *MAGNEX*, <https://www.lns.infn.it/it/apparati/magnex.html>
- ³ *NUMEN*, <https://www.lns.infn.it/it/ricerca/progetti/numen.html>
- ⁴ *Ball Splines/One End Stepped and Threaded*, <https://uk.misumi-ec.com/vona2/detail/110302402950>
- ⁵ *BREVA*, <https://symetrie.fr/hexapodes/breva/>

9 Catalogs

- ¹ SMC, *"Cylinder with lock, MWB series"*, Tokyo
- ² Myostat motion control INC, *"SRJ brochure_19"*, Canada, 2019
- ³ SMC, *"Compact 5-Port Solenoid Valve"*, Tokyo
- ⁴ Thomson, *"Linear actuator"*, United Kingdom
- ⁵ Festo, *"Cylinders with holding brake DFLC/G"*, Germany, 2021
- ⁶ Zimmer, *"Clamping elements series HKR"*, Italy
- ⁷ Abba Linear Tech Co., *"Self-lubricated linear bearings"*, Taiwan
- ⁸ NSK, *"Linear guide RA series"*, Tokyo
- ⁹ Schneeberger, *"Linear bearings"*, Switzerland
- ¹⁰ Harmonic Drive, *"LAH Linear actuator"*, Germany
- ¹¹ Weingrill, *"Martinetti meccanici TS"*, Italy
- ¹² Physik instrumente, *"Micropositioning actuators"*, Germany
- ¹³ Oriental motor, *"Compact Linear Actuators DRS2 Series"*, USA
- ¹⁴ SMC, *"Snodo sferico"*, Tokyo
- ¹⁵ SKF, *"Terminali con filettatura maschio SALKB 16 F"*, Sweden
- ¹⁶ Misumi, *"Misumi web index"*, Tokyo
- ¹⁷ Hiwin, *"Guide lineari"*, Italy
- ¹⁸ Gefran, *"Trasduttore rettilineo di posizione"*, Italy

Appendix A

MATLAB Script for the solution of the Stewart platform inverse kinematic

```
%%Inputs
r1=190/2; %radius of the base frame
r2=190/2; %radius of the moving frame
l1=590;
l2=l1/cosd(30)+300/cosd(30);
l3=300;
htot=935;
h1=106;
h2=21+15+280*tand(30)-140*tand(30)+34/cosd(30);
h=htot-h1-h2-(l1+l3)*tand(30);
gamma=15;

psi=5; %rotation of P around X
teta=3; %rotation of P around Y
phi=0; %rotation of P around Z
X=5;
Y=8;
Z=h;

%%Stewart platform coordinates
A=[r1*cosd(60-gamma) r1*sind(60-gamma) 0]';
B=[r1*cosd(60+gamma) r1*sind(60+gamma) 0]';
C=[-r1*cosd(gamma) r1*sind(gamma) 0]';
D=[-r1*cosd(gamma) -r1*sind(gamma) 0]';
E=[r1*cosd(60+gamma) -r1*sind(60+gamma) 0]';
F=[r1*cosd(60-gamma) -r1*sind(60-gamma) 0]';
A1=[r2*cosd(gamma) r2*sind(gamma) 0]';
B1=[-r2*sind(30-gamma) r2*cosd(30-gamma) 0]';
C1=[-r2*sind(30+gamma) r2*cosd(30+gamma) 0]';
D1=[-r2*sind(30+gamma) -r2*cosd(30+gamma) 0]';
E1=[-r2*sind(30-gamma) -r2*cosd(30-gamma) 0]';
F1=[r2*cosd(gamma) -r2*sind(gamma) 0]';

OB=[0 0 0]';
OP=[0 0 0]';
Bq=[X Y Z]';
Rpb=[cosd(phi)*cosd(teta) cosd(phi)*sind(teta)*sind(psi)-
sind(phi)*cosd(psi)
cosd(phi)*sind(teta)*cosd(psi)+sind(phi)*sind(psi);...
sind(phi)*cosd(teta)
sind(phi)*sind(teta)*sind(psi)+cosd(phi)*cosd(psi)
sind(phi)*sind(teta)*cosd(psi)-cosd(phi)*sind(psi);...
```

```

        -sind(teta) cosd(teta)*sind(psi) cosd(teta)*cosd(psi)]; %rotation
matrix
BuA1=Rpb*A1; %coordinates of point A1 with respect to B
BuB1=Rpb*B1; %coordinates of point B1 with respect to B
BuC1=Rpb*C1; %coordinates of point C1 with respect to B
BuD1=Rpb*D1; %coordinates of point D1 with respect to B
BuE1=Rpb*E1; %coordinates of point E1 with respect to B
BuF1=Rpb*F1; %coordinates of point F1 with respect to B
BOP=Rpb*OP;
LambdaAA1=norm(BuA1+Bq-A);
LambdaBB1=norm(BuB1+Bq-B);
LambdaCC1=norm(BuC1+Bq-C);
LambdaDD1=norm(BuD1+Bq-D);
LambdaEE1=norm(BuE1+Bq-E);
LambdaFF1=norm(BuF1+Bq-F);

%%Stewart platform plots
plot3([A(1) B(1) C(1) D(1) E(1) F(1) A(1)], [A(2) B(2) C(2) D(2) E(2) F(2)
A(2)], [A(3) B(3) C(3) D(3) E(3) F(3) A(3)], 'b')
hold on
plot3([BuA1(1)+Bq(1) BuB1(1)+Bq(1) BuC1(1)+Bq(1) BuD1(1)+Bq(1)
BuE1(1)+Bq(1) BuF1(1)+Bq(1) BuA1(1)+Bq(1)], [BuA1(2)+Bq(2) BuB1(2)+Bq(2)
BuC1(2)+Bq(2) BuD1(2)+Bq(2) BuE1(2)+Bq(2) BuF1(2)+Bq(2)
BuA1(2)+Bq(2)], [BuA1(3)+Bq(3) BuB1(3)+Bq(3) BuC1(3)+Bq(3) BuD1(3)+Bq(3)
BuE1(3)+Bq(3) BuF1(3)+Bq(3) BuA1(3)+Bq(3)], 'b')
plot3([A(1) BuA1(1)+Bq(1)], [A(2) BuA1(2)+Bq(2)], [A(3) BuA1(3)+Bq(3)], 'r')
plot3([B(1) BuB1(1)+Bq(1)], [B(2) BuB1(2)+Bq(2)], [B(3) BuB1(3)+Bq(3)], 'r')
plot3([C(1) BuC1(1)+Bq(1)], [C(2) BuC1(2)+Bq(2)], [C(3) BuC1(3)+Bq(3)], 'r')
plot3([D(1) BuD1(1)+Bq(1)], [D(2) BuD1(2)+Bq(2)], [D(3) BuD1(3)+Bq(3)], 'r')
plot3([E(1) BuE1(1)+Bq(1)], [E(2) BuE1(2)+Bq(2)], [E(3) BuE1(3)+Bq(3)], 'r')
plot3([F(1) BuF1(1)+Bq(1)], [F(2) BuF1(2)+Bq(2)], [F(3) BuF1(3)+Bq(3)], 'r')
plot3(OB(1),OB(2),OB(3), '*')
plot3(OP(1)+Bq(1),OP(2)+Bq(2),OP(3)+Bq(3), '*')

axis equal
xlabel('X')
ylabel('Y')
zlabel('Z')

%%Numen coordinates
G=[-l1 0 htot-h1]';
H=[-l1 0 -h1]';
I=[0 0 -h1]';

%%Numen plots
plot3([OB(1) I(1)], [OB(2) I(2)], [OB(3) I(3)])
plot3([I(1) H(1)], [I(2) H(2)], [I(3) H(3)])
plot3([H(1) G(1)], [H(2) G(2)], [H(3) G(3)])
plot3(G(1),G(2),G(3), '*')

%%Detectors' shell coordinates
J=[0 0 h2]';
K=[-l1-l3 0 h2+l1*tand(30)+l3*tand(30)]';
L=[-l1 0 h2+l1*tand(30)+l3*tand(30)]';
BuJ=Rpb*J;
BuK=Rpb*K;
BuL=Rpb*L;

```



```

%%Detectors' shell plots
plot3([OP(1)+Bq(1) BuJ(1)+Bq(1)], [OP(2)+Bq(2) BuJ(2)+Bq(2)], [OP(3)+Bq(3)
BuJ(3)+Bq(3)])
plot3([BuJ(1)+Bq(1) BuK(1)+Bq(1)], [BuJ(2)+Bq(2)
BuK(2)+Bq(2)], [BuJ(3)+Bq(3) BuK(3)+Bq(3)])
plot3([BuK(1)+Bq(1) BuL(1)+Bq(1)], [BuK(2)+Bq(2)
BuL(2)+Bq(2)], [BuK(3)+Bq(3) BuL(3)+Bq(3)])
plot3(BuL(1)+Bq(1), BuL(2)+Bq(2), BuL(3)+Bq(3), '*')

hold off

%% Compensation
figure
X=G(1)-BuL(1)-Bq(1);
Y=G(2)-BuL(2)-Bq(2);
Z=h+G(3)-BuL(3)-Bq(3);

Bq1=[X Y Z]';

lambdaAA1=norm(BuA1+Bq1-A);
lambdaBB1=norm(BuB1+Bq1-B);
lambdaCC1=norm(BuC1+Bq1-C);
lambdaDD1=norm(BuD1+Bq1-D);
lambdaEE1=norm(BuE1+Bq1-E);
lambdaFF1=norm(BuF1+Bq1-F);

%%Stewart platform plots
plot3([A(1) B(1) C(1) D(1) E(1) F(1) A(1)], [A(2) B(2) C(2) D(2) E(2) F(2)
A(2)], [A(3) B(3) C(3) D(3) E(3) F(3) A(3)], 'b')
hold on
plot3([BuA1(1)+Bq1(1) BuB1(1)+Bq1(1) BuC1(1)+Bq1(1) BuD1(1)+Bq1(1)
BuE1(1)+Bq1(1) BuF1(1)+Bq1(1) BuA1(1)+Bq1(1)], [BuA1(2)+Bq1(2)
BuB1(2)+Bq1(2) BuC1(2)+Bq1(2) BuD1(2)+Bq1(2) BuE1(2)+Bq1(2)
BuF1(2)+Bq1(2) BuA1(2)+Bq1(2)], [BuA1(3)+Bq1(3) BuB1(3)+Bq1(3)
BuC1(3)+Bq1(3) BuD1(3)+Bq1(3) BuE1(3)+Bq1(3) BuF1(3)+Bq1(3)
BuA1(3)+Bq1(3)], 'b')
plot3([A(1) BuA1(1)+Bq1(1)], [A(2) BuA1(2)+Bq1(2)], [A(3)
BuA1(3)+Bq1(3)], 'r')
plot3([B(1) BuB1(1)+Bq1(1)], [B(2) BuB1(2)+Bq1(2)], [B(3)
BuB1(3)+Bq1(3)], 'r')
plot3([C(1) BuC1(1)+Bq1(1)], [C(2) BuC1(2)+Bq1(2)], [C(3)
BuC1(3)+Bq1(3)], 'r')
plot3([D(1) BuD1(1)+Bq1(1)], [D(2) BuD1(2)+Bq1(2)], [D(3)
BuD1(3)+Bq1(3)], 'r')
plot3([E(1) BuE1(1)+Bq1(1)], [E(2) BuE1(2)+Bq1(2)], [E(3)
BuE1(3)+Bq1(3)], 'r')
plot3([F(1) BuF1(1)+Bq1(1)], [F(2) BuF1(2)+Bq1(2)], [F(3)
BuF1(3)+Bq1(3)], 'r')
plot3(OB(1), OB(2), OB(3), '*')
plot3(OP(1)+Bq1(1), OP(2)+Bq1(2), OP(3)+Bq1(3), '*')

axis equal
xlabel('X')
ylabel('Y')
zlabel('Z')

```

```

%%Numen plots
plot3([OB(1) I(1)], [OB(2) I(2)], [OB(3) I(3)])
plot3([I(1) H(1)], [I(2) H(2)], [I(3) H(3)])
plot3([H(1) G(1)], [H(2) G(2)], [H(3) G(3)])
plot3(G(1), G(2), G(3), '*'')

%%Detectors' shell plots
plot3([OP(1)+Bq1(1) BuJ(1)+Bq1(1)], [OP(2)+Bq1(2)
BuJ(2)+Bq1(2)], [OP(3)+Bq1(3) BuJ(3)+Bq1(3)])
plot3([BuJ(1)+Bq1(1) BuK(1)+Bq1(1)], [BuJ(2)+Bq1(2)
BuK(2)+Bq1(2)], [BuJ(3)+Bq1(3) BuK(3)+Bq1(3)])
plot3([BuK(1)+Bq1(1) BuL(1)+Bq1(1)], [BuK(2)+Bq1(2)
BuL(2)+Bq1(2)], [BuK(3)+Bq1(3) BuL(3)+Bq1(3)])
plot3(BuL(1)+Bq1(1), BuL(2)+Bq1(2), BuL(3)+Bq1(3), '*'')

hold off

% nAA1=[r2*cosd(gamma)-r1*cosd(60-gamma) r2*sind(gamma)-r1*sind(60-gamma)
h]';
% nBB1=[-r2*sind(30-gamma)-r1*cosd(60+gamma) r2*cosd(30-gamma)-
r1*sind(60+gamma) h]';
% nCC1=[-r2*sind(30+gamma)+r1*cosd(gamma) r2*cosd(30+gamma)-
r1*sind(gamma) h]';
% nDD1=[-r2*sind(30+gamma)+r1*cosd(gamma) -
r2*cosd(30+gamma)+r1*sind(gamma) h]';
% nEE1=[-r2*sind(30-gamma)-r1*cosd(60+gamma) -r2*cosd(30-
gamma)+r1*sind(60+gamma) h]';
% nFF1=[r2*cosd(gamma)-r1*cosd(60-gamma) -r2*sind(gamma)+r1*sind(60-
gamma) h]';
%
% n1=nAA1/norm(nAA1);
% n2=nBB1/norm(nBB1);
% n3=nCC1/norm(nCC1);
% n4=nDD1/norm(nDD1);
% n5=nEE1/norm(nEE1);
% n6=nFF1/norm(nFF1);
%
% q=quiver3(A(1), A(2), 0, nAA1(1), nAA1(2), nAA1(3))
% q.ShowArrowHead='off';
% q.LineWidth=1.5;
% q
% p=quiver3(B(1), B(2), 0, nBB1(1), nBB1(2), nBB1(3))
% p.ShowArrowHead='off';
% p.LineWidth=1.5;
% p
% w=quiver3(C(1), C(2), 0, nCC1(1), nCC1(2), nCC1(3))
% w.ShowArrowHead='off';
% w.LineWidth=1.5;
% w
% z=quiver3(D(1), D(2), 0, nDD1(1), nDD1(2), nDD1(3))
% z.ShowArrowHead='off';
% z.LineWidth=1.5;
% z
% y=quiver3(E(1), E(2), 0, nEE1(1), nEE1(2), nEE1(3))
% y.ShowArrowHead='off';
% y.LineWidth=1.5;
% y

```

```
% j=quiver3(F(1),F(2),0,nFF1(1),nFF1(2),nFF1(3))
% j.ShowArrowHead='off';
% j.LineWidth=1.5;
% j
% hold off
```